NASA TECHNICAL NOTE

NASA TN D-4064

c. 1

NASA TN D-4064

EFFECTS OF JET PLUMING ON THE STATIC STABILITY OF FIVE ROCKET MODELS AT MACH NUMBERS OF 4, 5, AND 6 AND STATIC PRESSURE RATIOS UP TO 26 000

by William F. Hinson and Robert J. McGhee

Langley Research Center
Langley Station, Hampton, Va.

NATIONAL AERONAUTICS AND SPACE ADMINISTRATION • WASHINGTON, D. C. • AUGUST 1967

NASA TN D-4064

EFFECTS OF JET PLUMING ON THE STATIC STABILITY OF FIVE ROCKET MODELS AT MACH NUMBERS OF 4, 5, AND 6 AND STATIC PRESSURE RATIOS UP TO 26 000

By William F. Hinson and Robert J. McGhee

Langley Research Center
Langley Station, Hampton, Va.

NATIONAL AERONAUTICS AND SPACE ADMINISTRATION

For sale by the Clearinghouse for Federal Scientific and Technical Information
Springfield, Virginia 22151 – CFSTI price $3.00

EFFECTS OF JET PLUMING ON THE STATIC STABILITY OF FIVE ROCKET MODELS AT MACH NUMBERS OF 4, 5, AND 6 AND STATIC PRESSURE RATIOS UP TO 26 000

By William F. Hinson and Robert J. McGhee
Langley Research Center

SUMMARY

The effect of jet pluming on the normal force and pitching moment of five cone-cylinder—flare-finned models has been measured at free-stream Mach numbers of 4, 5, and 6. The Reynolds number per foot was 0.54 to 0.76×10^6 $\left(1.77 \text{ to } 2.49 \times 10^6\right.$ per meter$\left.\right)$ at free-stream Mach numbers of 4 and 6, respectively. The range of jet-static-pressure ratios varied from a jet-off condition to values of 4000 to 8000 at free-stream Mach numbers of 4 and 6, respectively, for a rocket nozzle of exit Mach number of 2.24. With a sonic nozzle, the jet-static-pressure ratio was from 16 000 to 26 000 at free-stream Mach numbers of 4 and 6, respectively.

Increasing the jet pressure ratio resulted in large jet plumes and initial turning angles approaching 100°, which in turn caused boundary-layer separation over large regions of the test models. Normal-force coefficients decreased to approximately a constant value with increasing jet pressure ratio associated with essentially complete flow separation over the body; however, when a flare afterbody was employed a larger jet pressure ratio was required before a near constant value was reached. All models generally displayed irregular pitching-moment-coefficient variations with jet pressure ratio, angle of attack, and Mach number. At moderate angles of attack and high jet pressure ratios, normal-force and pitching-moment coefficients obtained with nozzles having exit Mach numbers of 2.24 and 1.0 at pressure ratios simulating the same initial turning angle of 90.3° were in poor agreement.

INTRODUCTION

As a rocket vehicle traverses the altitude range, the pressure at the nozzle exit relative to the ambient pressure increases and a large gaseous jet plume appears at the higher altitudes. The interaction of this plume with the surrounding flow field results in flow separation over the vehicle sufficient to render the stabilizing surfaces ineffective over a large angle-of-attack range.

Experimental data on the effect of jet pluming on vehicle static stability, as well as data obtained by wind-tunnel and flight-simulation techniques are contained in references 1 to 8. However, in these references the range of values of the ratio of exit pressure to free-stream static pressure has been rather limited. For example, references 4 and 7 contain experimental data for pressure ratios of about 3200 and 2450, respectively. No known information is available on vehicle static stability for pressure ratios in the range approaching 10 000. This pressure-ratio range is realistic for a rocket motor with an exit Mach number of about 3.0 operating at an altitude of approximately 200 000 feet (60.96 km).

The purpose of this investigation is to extend the range of pressure ratios to larger values than has been reported thus far and to measure effects of the jet plume on static stability. Data were also obtained in the lower range of pressure ratios, including jet-off conditions.

The models used were scaled from the upper three stages of a proposed unguided four-stage rocket vehicle similar in performance to the NASA Scout vehicle. Five model configurations having a nozzle with a design exit Mach number of 2.24 were tested at free-stream Mach numbers of 4, 5, and 6. One model was also tested with a sonic nozzle (Mach 1). This nozzle was used to examine the effects of large values of jet pressure ratios and consequently large values of jet initial turning angle at lower chamber pressure. The exhaust medium used for both nozzles was compressed nitrogen at a source pressure of 3000 pounds per square inch (20.7 meganewtons/meter^2). Utilizing the nozzle with exit Mach number of 2.24 with a maximum plenum chamber pressure of approximately 2700 pounds/inch^2 (17.6 meganewtons/meter^2) resulted in maximum jet pressure ratios of 4000 and 8000 at free-stream Mach numbers of 4 and 6, respectively. Using the sonic nozzle with the largest plenum chamber pressure resulted in maximum jet pressure ratios of 16 000 and 26 000 at free-stream Mach numbers of 4 and 6, respectively.

The tests were conducted in a 2-foot hypersonic facility with Reynolds number per foot varying from 0.54 to 0.76×10^6 $\left(1.77 \text{ to } 2.49 \times 10^6 \text{ per meter}\right)$ at free-stream Mach numbers of 4 and 6, respectively. The angle of attack was varied from 0° to 8°.

SYMBOLS

A	cross-sectional area of particular model maximum cylinder diameter, inch^2 (centimeter^2)
D	maximum cylinder diameter of a particular model, inches (centimeters)
C_N	normal-force coefficient, $F_N/q_\infty A$

C_m	pitching-moment coefficient, $M_Y/q_\infty AD$
F_N	normal force along Z-axis, positive direction upward, pounds force (newtons)
M_j	jet exit Mach number
M_Y	moment about Y-axis, in-lb (newton-centimeters)
M_∞	free-stream Mach number
p_j/p_∞	jet pressure ratio (ratio of jet-exit pressure to free-stream static pressure)
q_∞	free-stream dynamic pressure, pounds/inch^2 (newtons/centimeter^2)
x_{cp}/D	ratio of center of pressure measured from model base to body diameter
α	angle of attack, degrees
δ_j	initial starting angle of exhaust gas of rocket nozzle, measured from the center line of the rocket nozzle, degrees (see fig. 5)
γ	ratio of specific heats

APPARATUS

Models

A sketch of the models tested, together with model designations and detailed dimensions, is shown in figure 1. Photographs of the models are shown in figure 2. The models were constructed of aluminum except the rear section of models 1, 2, and 3; these sections were constructed of mild steel. Model 1 represents the upper three stages of a proposed four-stage unguided rocket vehicle similar to the present NASA Scout, but with no rear stabilizing surfaces. Models 2 and 3 show a 20° half-angle flare and cruciform fins, respectively, which are used to add stability for the same three-stage configuration. The fins used were of the wedge type with a total angle of 5°. Model 4, by contrast, represents just the upper two stages of this three-stage vehicle. Model 5 is the same two stages as model 4 except that the "flare—reverse-flare" has been removed.

The two nozzles used in the investigation are shown in figure 3. The nozzles were designed to have exit Mach numbers of 2.24 and 1.0 and to use compressed nitrogen with a source pressure of 3000 lb/in^2 (20.7 meganewtons/meter^2), as the exhaust medium. The nozzle design technique is discussed in reference 6. Allowance for the sting was made in the nozzle design, in that the proper nozzle area ratio was maintained. The compressed nitrogen passed through the hollow sting and was injected into the nozzle settling chamber through louvers.

Wind Tunnel

The tests were conducted in a 2-foot hypersonic facility (ref. 9) at the Langley Research Center. This wind tunnel is an ejector type which provides continuous flow at high Mach numbers.

The average test conditions are shown in the following table:

M_∞	Stagnation temperature		Stagnation pressure		Static pressure		Reynolds number	
	$^\circ$R	$^\circ$K	lb/ft^2	kN/m^2	lb/ft^2	N/m^2	per ft	per m
4	559.67	311	835.4	39.925	5.5	26.29	0.54×10^6	1.772×10^6
5	759.67	422	1670.7	79.846	3.16	15.10	.42	1.377
6	759.67	422	4176.8	199.616	2.65	12.66	.76	2.493

Instrumentation

A two-component electrical-strain-gage balance similar to the one described in reference 7 was designed and constructed to measure the normal force and pitching moment for these models. The pressure in the nozzle settling chamber was measured by Bourdon pressure gages which were visually monitored during the tests. The pressure gages were connected to the nozzles by a steel tube with an inside diameter of 0.030 inch (0.76 mm). The tube terminated in the surface of the support sting at the maximum diameter of the nozzle plenum chamber.

Tests

The test conditions for each model are summarized in table 1. All models were tested with the $M_j = 2.24$ nozzle at $M_\infty = 4$, 5, and 6. Model 3 was tested also with the $M_j = 1.0$ nozzle. In the tests with the $M_j = 2.24$ nozzle the p_j/p_∞ range was from jet-off to 4000 at $M_\infty = 4$ and from jet-off to 8000 at $M_\infty = 6$. When the $M_j = 1.0$ nozzle was used, the p_j/p_∞ range was from jet-off to 16 000 at $M_\infty = 4$ and from jet-off to 26 000 at $M_\infty = 6$. The angle-of-attack range was varied from 0° to 8° in increments of 2°. Schlieren photographs were obtained for selected test conditions.

ACCURACY OF DATA

The ratios of p_j/p_∞ quoted herein are estimated to be accurate within ±2 percent. Mach number variation in the region of the test model was accurate within ±0.02. Angle-of-attack values presented are estimated to be accurate within $\pm 0.1^\circ$. Maximum error in the aerodynamic coefficients for C_N and C_m, based on balance error, data reduction, and some repeat data points are estimated to be within ±0.05. The estimated accuracy of x_{cp}/D is approximately one body diameter. In some cases the x_{cp}/D location is close to or forward of the nose tip. This condition generally occurred with the jet on at low angles of attack when most of the model body was engulfed in separated flow. During these conditions the magnitude of the coefficients used to compute x_{cp}/D was small and sometimes less than the quoted accuracy of the balance. Therefore, these data points should be interpreted only as a qualitative measure of model instability.

METHOD OF ANALYSIS

The normal-force and pitching-moment measurements are referred to the body-axis system of figure 4. Location of the center of pressure x_{cp}/D (measured from the model base) has been obtained from the ratio of the pitching-moment and normal-force measurements. The moment-center location of 3.85 inches (9.78 cm) from the model base (see fig. 1) is not realistic for these models since the center of gravity of the upper three-stage combinations of the NASA Scout is located at approximately 65 percent of the body length as compared with a location approximately 72 percent of the body length for these models. Since these models (models 1, 2, and 3) were scaled from proposed launch vehicles, and since full-scale vehicle center-of-gravity positions are subject to change because of payload and/or vehicle configuration, it was considered unnecessary to transfer the moment data to another body station. Therefore, the stability implications are relative to the balance moment-center location of 3.85 inches (9.78 cm) from the model base. For convenience the same moment reference was used for the two-stage models 4 and 5. The models were considered to be statically stable if the x_{cp}/D was rearward of the moment reference location. If the x_{cp}/D location was at or forward of the moment reference, then the models were considered to be neutrally stable or statically unstable.

RESULTS AND DISCUSSION

A schematic representation of the flow-field nomenclature applicable to model 5 is shown in figures 5(a) and 5(b) for test conditions representative of small and large angles of attack, respectively. The region denoted by the shaded area is the zone in which boundary-layer separation is expected to be caused chiefly by interference between the body flow field and the jet plume. Generally, separation would be expected to spread outward and extend forward on the model body surface as the physical size of the plume increases $\left(\text{as } p_j/p_\infty \text{ increases}\right)$. As the angle of attack is increased, the separated region on the windward side (lower surface) would be expected to be decreased by the larger compression, whereas that on the upper surface would tend to be increased. This phenomenon is illustrated in figure 5(b) for an extreme case in which the lower-surface separation has been shown to decrease to zero. The boundary-layer separation would be expected to manifest itself by large decreases in dynamic pressure in the region of the stabilizing surfaces and hence would result in uncertain and irregular effects on the normal-force coefficients and vehicle stability. The presence of a flare in the flow field as illustrated by figure 5 may result in additional disturbances, and flow reattachment may possibly be caused by the additional compression on the flare surface itself.

The basic data, consisting of normal-force coefficient C_N, pitching-moment coefficient C_m, and center-of-pressure ratio x_{cp}/D for all models, are plotted as functions of jet pressure ratio p_j/p_∞ at the various angles of attack in figures 6 to 10. The measured coefficient data at $\alpha = 0^\circ$ were zero or near zero and have not been presented for all models. The data for model 1 at $\alpha = 0^\circ$ presented in figures 6(a), (b), and (c) are typical of all models. Included with the basic data plots are selected schlieren photographs of the flow field at various values of p_j/p_∞ and angles of attack.

Effect of Jet Pressure Ratio and Angle of Attack

Jet-off condition.- With the exception of model 1, which had no stabilizing surfaces, the three-stage configurations (models 2 and 3) are shown, by the pitching-moment data in figures 7 and 8, to exhibit near neutral stability or only slight instability throughout the test range of angle of attack for jet-off conditions. For the two-stage configurations (models 4 and 5) with the jet off, the data of figures 9 and 10 show that the model was unstable for angles of attack greater than 2°. The unstable contribution to the pitching moment of the flare—reverse-flare of model 4 is readily apparent from the data of figure 9.

Jet-on condition.- Although it can be shown that for the configurations of this investigation, only small jet pressure ratios would be required to fill the base of the models completely, examination of many additional schlieren photographs not reproduced herein suggested that significant flow separation on the body was not induced by the plume at jet pressure ratios p_j/p_∞ much lower than 250. The lowest test pressure ratios were approximately 250, 425, and 540 at Mach numbers of 4, 5, and 6, respectively. At these pressure ratios and at $\alpha = 0^\circ$, most of the stabilizing surfaces were immersed in separated flow.

As p_j/p_∞ was increased, the size of the jet plume and the associated initial starting angle δ_j increased, the latter eventually reaching a value approaching 100°. With increasing p_j/p_∞, the extent of flow separation over the model body generally increased, as is well illustrated in the schlieren photographs in figures 6 to 10. In figures 6 and 8 (models 1 and 3) it can be seen that for small angles of attack the normal-force coefficient decreased to approximately a constant value for $p_j/p_\infty \geqq 1000$. When a flare was used, such as on models 2, 4, and 5, a larger value of p_j/p_∞ was required before the normal-force coefficient decreased to a near constant value. The rear-section geometry of these models, a large base coupled with a discrete flare angle, resulted in local external flow angles not parallel to the body axis. Therefore, it would be expected that a large plume $\left(\text{higher } p_j/p_\infty\right)$ would be required to produce the same separation effects. Similar phenomena were shown in reference 7. It is surmised that the separated-flow region at the highest jet pressure ratios due to the presence of the jet plume has advanced to the maximum forward point on the model body for the specific angle of attack. Since the model nose cannot be seen in the schlieren photographs, projections of these shock patterns on some photographs were extended, and these projections indicated that the flow-separation point had moved forward to the nose-cone—cylinder juncture ($0 \geqq \alpha \leqq 4^\circ$).

The trends observed for small angles of attack are generally valid up to the highest angles of attack for this investigation ($\alpha = 8^\circ$); however, because of the probable change in separated regions shown in the schlieren photographs, higher values of jet pressure ratio are required. For both two-stage models (models 4 and 5) at $M_\infty = 4.0$, a trend with increasing angle of attack appears to result in an increase in the normal-force coefficient with increasing pressure ratios after the initial decrease. In addition, figures 9(a) and 10(a) show that a decreasing trend follows at still higher pressure ratios. Since this behavior is peculiar to the model with the small flare, which corresponds to the interstage flare for the three-stage model, it is possible that some unusual relationship between flare angle and Mach number is responsible. The data in figure 10(h) $\left(p_j/p_\infty = 2538\right)$ suggest that two separated regions occur on the windward side of the body, one in front of the flare-cylinder juncture and one at the rear of the flare. At higher pressure ratios the flow appears to separate over the entire flare and when this phenomenon occurred, the normal-force coefficient again began decreasing. This particular separation phenomenon was not observed in the schlieren photographs for the large-base flare angle of model 2 and the force- and moment-coefficient data do not reflect this behavior.

All the models generally displayed pitching-moment variations with jet pressure ratio for which no suitable physical explanation is presently discernible. With the exception of model 1, which had no base protuberance (no fin or flare), there is no apparent correlation between the configuration, Mach number, or angle-of-attack variations. In this single case, figure 6 does indicate that for the lowest test Mach number ($M_\infty = 4.0$), essentially all of the pitching-moment change with plume shape occurred at pressure ratios near the lower limit of these tests. However, even for this simple base shape the irregularities in the pitching moment at the two higher Mach numbers cannot be fully explained from the data.

Effect of Nozzle Geometry

It is indicated in reference 1 that among the many variables in the simulation of jet boundaries, perhaps the most important property to be simulated is the initial starting angle of the jet. Use of a supersonic nozzle to achieve large values of p_j/p_∞ and corresponding large initial starting angles would require a large plenum chamber pressure. If a nozzle with exit Mach number $M_j = 1.0$ is used, large values of p_j/p_∞ and large initial starting angles can be produced with a smaller chamber pressure than with a supersonic nozzle. In this investigation, an $M_j = 1.0$ nozzle was utilized for the finned configuration of the three-stage vehicle (model 3) in order to compare the aerodynamic characteristics with those for the $M_j = 2.24$ nozzle. The basic data are given in figure 8, and the nozzle effects are compared in figures 11 to 13 at $M_\infty = 6.0$. Figure 11 compares, for each of the two nozzle configurations, the initial starting angle of the exhaust flow at the base of the nozzle δ_j in quiescent air ($M_\infty = 0$) as a function of p_j/p_∞ for an exhaust pressure corresponding to the test stream static pressure at $M_\infty = 6.0$. These curves were calculated by using two-dimensional theory. As an illustration, the initial plume shape near the body surface would be the same for the two nozzles when, for the inclination angle selected, the corresponding pressure ratios are reproduced $\left(p_j/p_\infty = 1000 \text{ for } M_j = 2.24 \text{ nozzle } \delta_j = 81.6^\circ\text{; for the } M_j = 1.0 \text{ nozzle at the same angle, } p_j/p_\infty = 520\right)$.

Figure 12 compares the measured aerodynamic coefficients for the two nozzles as a function of p_j/p_∞ for model 3 at $M_\infty = 6.0$ and at angles of attack of 4° and 6°. The smallest obtainable jet-on value of p_j/p_∞ with the $M_j = 1.0$ nozzle was 3400. The data indicate that both normal-force and pitching-moment coefficients are essentially independent of pressure ratio above values of 4500 and 10 000 for the $M_j = 2.24$ and $M_j = 1.0$ nozzle, respectively. Although data in the low jet-pressure-ratio range are lacking and no comparison can be made with the tests of reference 1, the data at moderate angles of attack for the present investigation at the high pressure ratios do not suggest that the aerodynamic behavior is the same for the same initial starting angle for the two nozzles. The entire comparable data for the $M_j = 1.0$ nozzle lies above that for the $M_j = 2.24$ nozzle.

Figure 13, which is a cross plot of the data of figure 8, shows the variation of the aerodynamic coefficients with angle of attack for model 3 using the $M_j = 2.24$ and the $M_j = 1.0$ nozzle for the same starting angle of $\delta_j = 90.3^\circ$. In addition to the data from figure 8, the normal-force and pitching-moment coefficients, at $\alpha = 0^\circ$, which had been previously indicated to be unaffected by p_j/p_∞, have been included in the figure. This figure more clearly represents the effect of angle of attack on both normal-force and pitching-moment coefficients and shows their divergence with increasing angle of attack, even for the same starting angle for the two nozzles. The implications of these results are that other factors, in addition to the starting angle of the exhaust plume, must be simulated when there is a supersonic or hypersonic external flow. One such factor, which could strongly influence the behavior in the region of the mixing zone of the two flows is the momentum flux (momentum per unit effective exhaust flow area) normal to the surface of the body.

Effect of Flare—Reverse-Flare

Figure 14 shows the effect of installing a flare—reverse-flare on model 5 approximately one-third the distance from the nose to form model 4. The general effect of the flare—reverse-flare was to increase both the normal-force and pitching-moment coefficients; such increases would have been expected in part because of the increased projected platform area well forward of the moment reference as well as the compression region associated with the forward-facing flare. Comparison of the data and schlieren photographs of figures 9 and 10 indicate that the presence of the flare—reverse-flare well forward on the body has delayed the tendency of the flow to separate over the forward portion of the body to appreciably higher pressure ratios than for model 5 with the flare—reverse-flare removed. Generally, however, the flow was separated over essentially the entire model in either configuration at the highest test pressure ratios.

CONCLUDING REMARKS

The effect of jet pluming on the normal-force and pitching-moment coefficients of five cone-cylinder-flare finned models has been measured at free-stream Mach numbers of 4, 5, and 6. The Reynolds number per foot was 0.54 to 0.76×10^6 $\left(1.772 \text{ to } 2.493 \times 10^6 \text{ per meter}\right)$ at $M = 4$ and 6, respectively. The range of jet-static-pressure ratios varied from a jet-off condition to values of 4000 to 8000 at $M = 4$ and 6, respectively, when a rocket nozzle of exit Mach number 2.24 was used. With a sonic nozzle, the jet-static-pressure ratio was 16 000 and 26 000 at free-stream Mach numbers of 4 and 6, respectively. Conclusions as follows were indicated:

1. Increasing the jet pressure ratio resulted in large jet plumes and initial turning angles approaching 100°, which in turn caused boundary-layer separation over large regions of the models.

2. Normal-force coefficients decreased to approximately a constant value with increasing jet pressure ratio associated with essentially complete flow separation over the body; however, when a flare afterbody was employed, a larger jet pressure ratio was required before a near-constant value was reached.

3. All models generally displayed irregular pitching-moment-coefficient variations with jet pressure ratio, angle of attack, and Mach number.

4. At moderate angles of attack and high jet pressure ratios, normal-force and pitching-moment coefficients obtained with nozzles having exit Mach numbers of 2.24 and 1.0 at pressure ratios simulating the same initial inclination angle of 90.3° were in poor agreement.

Langley Research Center,
National Aeronautics and Space Administration,
Langley Station, Hampton, Va., February 17, 1967,
124-07-03-05-23.

REFERENCES

1. Love, Eugene S.; Grigsby, Carl E.; Lee, Louise P.; and Woodling, Mildred J.: Experimental and Theoretical Studies of Axisymmetric Free Jets. NASA TR R-6, 1959. (Supersedes NACA RM L54L31 by Love and Grigsby, RM L55J14 by Love, RM L56G18 by Love, Woodling, and Lee, and TN 4195 by Love and Lee.)

2. Fetterman, David E., Jr.: Effects of Simulated Rocket-Jet Exhaust on Stability and Control of a Research-Type Airplane Configuration at a Mach Number of 6.86. NASA TM X-127, 1959.

3. Dryer, Murray; and North, Warren J.: Preliminary Analysis of the Effect of Flow Separation Due to Rocket Jet Pluming on Aircraft Dynamic Stability During Atmospheric Exit. NASA MEMO 4-22-59E, 1959.

4. Salmi, Reino J.: Effects of Jet Billowing on Stability of Missile-Type Bodies at Mach 3.85. NASA TN D-284, 1960.

5. Stalmach, C. J., Jr.; and Cooksey, J. M.: Simulation of Rocket Power Effects on Vehicle Stability and Measurements of Aerodynamic Damping in a Hypervelocity Wind Tunnel. Paper No. 62-24, Inst. Aerospace Sci., 1962.

6. Falanga, Ralph A.; Hinson, William F.; and Crawford, Davis H.: Exploratory Tests of the Effects of Jet Plumes on the Flow Over Cone-Cylinder-Flare Bodies. NASA TN D-1000, 1962.

7. Hinson, William F.; and Falanga, Ralph A.: Effect of Jet Pluming on the Static Stability of Cone-Cylinder-Flare Configurations at a Mach Number of 9.65. NASA TN D-1352, 1962.

8. Hinson, William F.; and Hoffman, Sherwood: Analysis of Jet Pluming Interference by Computer Simulation of Measured Flight Motions of the RAM A Fourth Stages. NASA TN D-2018, 1963.

9. Stokes, George M.: Description of a 2-Foot Hypersonic Facility at the Langley Research Center. NASA TN D-939, 1961.

TABLE 1.- MODEL TEST CONDITIONS

M_∞	α, deg	p_j/p_∞							Figure	
									Data	Schlieren photographs
		Model 1, M_j = 2.24								
4	0	Jet-off*	255	720	1600	2 700	3 100	4050*	6(a)	6(d)
	2	Jet-off	255	720	1600	2 700	3 100	4050		
	4	Jet-off	250	696*	1600	2 675	3 140	4047*		6(d)
	6	Jet-off	255	720*	1600	2 675	3 100	4040*		6(d)
	8	Jet-off	255	720	1600	2 710	3 150	4100		
5	0	Jet-off*	490	1290	2900	4 850	5 550	5912*	6(b)	6(e)
	2	Jet-off	490	1290	2900	4 850	5 550	-----		
	4	Jet-off	470*	1275	2900	4 880	5 130	5642*		6(e)
	6	Jet-off	475	1275	2900	4 900	5 640	-----		
	8	Jet-off	425*	1140	2600	4 490	5 160*	-----		6(e)
6	0	Jet-off*	550	1500	3420	5 700	6 700	7830*	6(c)	6(f)
	2	Jet-off	550*	1500	3420	5 700	6 700	6898*		6(f)
	4	Jet-off	500	1500	3400	5 830	6 750	-----		
	6	Jet-off	550	1500*	3330	4 900	6 600	7450*		6(f)
	8	Jet-off	540	1500	3460	------	------	-----		
		Model 2, M_j = 2.24								
4	0	Jet-off*	250	730	1600	2 710	3 130	4061*	7(a)	7(d)
	2	Jet-off	250	730	1600	2 710	3 130	-----		
	4	Jet-off	250	730	1600*	2 700	3 140	3791*		7(d)
	6	Jet-off	250	730	1630	2 700	3 150	-----		
	8	Jet-off	250	730	1600*	2 750	3 100	4004*		7(d)
5	0	Jet-off	450	1250	2875	4 850	5 600	-----	7(b)	
	2	Jet-off	450	1250	2875	4 850	5 600	-----		
	4	Jet-off	450	1250	2900	4 850	------	-----		
	6	Jet-off	450	1250	2850	4 850	5 600	-----		
	8	Jet-off	440	1250	2850	4 900	------	-----		
6	0	Jet-off	572*	1500	3400	5 950	6 875	7878*	7(c)	7(e)
	2	Jet-off	550	1500	3400	5 950	6 875	-----		
	4	Jet-off*	550	1500	3440	5 800	6 700	7181*		7(e)
	6	Jet-off	550*	1500	3400	5 800	6 700	7511*		7(e)
	8	Jet-off	550	1500	-----	------	------	-----		
		Model 3, M_j = 2.24								
4	0	Jet-off	250	700	1600	2 750	3 150	-----	8(a)	
	2	Jet-off	250	700	1600	2 750	3 150	-----		
	4	Jet-off	250	700	1600	2 750	3 100	-----		
	6	Jet-off	250	700	1600	2 750	3 100	-----		
	8	Jet-off	250	700	1600	2 750	3 100	-----		
		Model 3, M_j = 1.0								
4	0	Jet-off	1500	4100	9500	13 400	16 100	-----	8(b)	
	2	Jet-off	1500*	4100	9500*	13 400*	16 100*	-----		8(g)
	4	Jet-off*	1500*	4100*	9400*	13 100*	16 100*	-----		8(h)
	6	Jet-off*	1500*	4312*	9301*	12 800*	16 100*	-----		8(i)
		Model 3, M_j = 2.24								
5	0	Jet-off	500	1250	2850	4 730	5 390	-----	8(c)	
	2	Jet-off	500	1250	2850	4 730	5 390	-----		
	4	Jet-off	460	1310	2900	4 910	5 600	-----		
	6	Jet-off	460	1260	-----	4 910	5 460	-----		
	8	Jet-off	460	1230	2800	5 010	5 375	-----		

*Denotes schlieren photograph presented.

TABLE 1.- MODEL TEST CONDITIONS – Concluded

M_∞	α, deg	p_j/p_∞							Figure	
									Data	Schlieren photographs
Model 3, M_j = 1.0										
5	0	Jet-off*	2730*	6845*	15 646*	22 797*	------	-----	8(d)	8(j)
	2	Jet-off*	2512*	6888*	15 551*	21 709*	------	-----		8(k)
	4	Jet-off*	2502*	6851*	15 474*	21 674*	------	-----		8(l)
	6	Jet-off*	2472*	6759*	15 463*	21 700	------	-----		8(m)
Model 3, M_j = 2.24										
6	0	Jet-off	550	1500	3 430	5 800	6 750	7830	8(e)	
	2	Jet-off	550	1500	3 430	5 800	6 750	7830		
	4	Jet-off*	558*	1500	3 426*	5 823*	6 800	7804*		8(p)
	6	Jet-off	550	1500	3 390	5 800	6 700	7830		
	8	Jet-off	550	1500	3 555*	5 871*	6 856*	7821*		8(r)
					4 476*	5 012*				
Model 3, M_j = 1.0										
6	0	Jet-off*	3595*	9347*	14 746*	20 264*	26 415*	-----	8(f)	8(n)
	2	Jet-off*	3327*	9103*	14 827*	20 473*	25 795*	-----		8(o)
	4	Jet-off*	3613*	9103*	14 867*	20 585*	26 300	-----		8(q)
	6	Jet-off*	3323*	9093* ?	14 843*	20 585*	26 100	-----		8(s)
Model 4, M_j = 2.24										
4	0	Jet-off	260	675	1 475	2 175	2 575	3000	9(a)	
	2	Jet-off	260	675	1 475	2 175	2 575	3000		
	4	Jet-off	250	675	1 540	2 175	2 600	3000		
	6	Jet-off	250	675	1 540	2 175	2 575	3000		
	8	Jet-off	250	675	1 500	2 150	2 640	3000		
5	0	Jet-off	425	1175	2 640	------	4 430	5150	9(b)	
	2	Jet-off	425	1175	2 640	------	4 430	5150		
	4	Jet-off	425	1175	2 640	3 675	4 500	5075		
	6	Jet-off	425	1200	2 575	3 740	4 475	5075		
	8	Jet-off	450	1175	2 675	3 700	4 450	5175		
6	0	Jet-off	550	1540	3 340	4 800	5 630	6300	9(c)	
	2	Jet-off	550	1540	3 340	4 800	5 630	6300		
	4	Jet-off*	550*	-----	3 384*	------	5 845*	6687*		9(d)
	6	Jet-off*	550*	1475	3 431*	------	5 825	6918*		9(e)
	8	Jet-off	575	1475	------	------	------	-----		
Model 5, M_j = 2.24										
4	0	Jet-off	240	675	1 475	2 125	2 575	2950	10(a)	
	2	Jet-off	240	675	1 475	2 125	2 575	2950		
	4	Jet-off	240	675	1 500	2 125	2 575	2950		
	6	Jet-off*	240	664*	1 493*	2 114*	2 538*	2972*		10(h)
	8	Jet-off	240	675	1 500	2 125	2 575	2950		
5	0	Jet-off	425	1150	2 650	------	4 450	5100	10(b)	
	2	Jet-off	425	1150	2 650	------	4 450	5100		
	4	Jet-off	425	1125	2 725	3 700	4 425	5150		
	6	Jet-off	425	1150	2 600	3 700	4 400	5100		
	8	Jet-off	425	1175	2 625	3 700	4 375	-----		
6	0	Jet-off*	601*	1508*	3 400	5 725	6 767*	-----	10(c)	10(d)
	2	Jet-off*	551*	1600*	3 404*	5 829*	6 808*	-----		10(e)
	4	Jet-off*	579*	1463*	3 301*	5 553*	6 512*	-----		10(f)
	6	Jet-off*	603*	1522*	3 397*	5 708*	6 738*	-----		10(g)
	8	Jet-off	550	1525	------	------	------	-----		

*Denotes schlieren photograph presented.

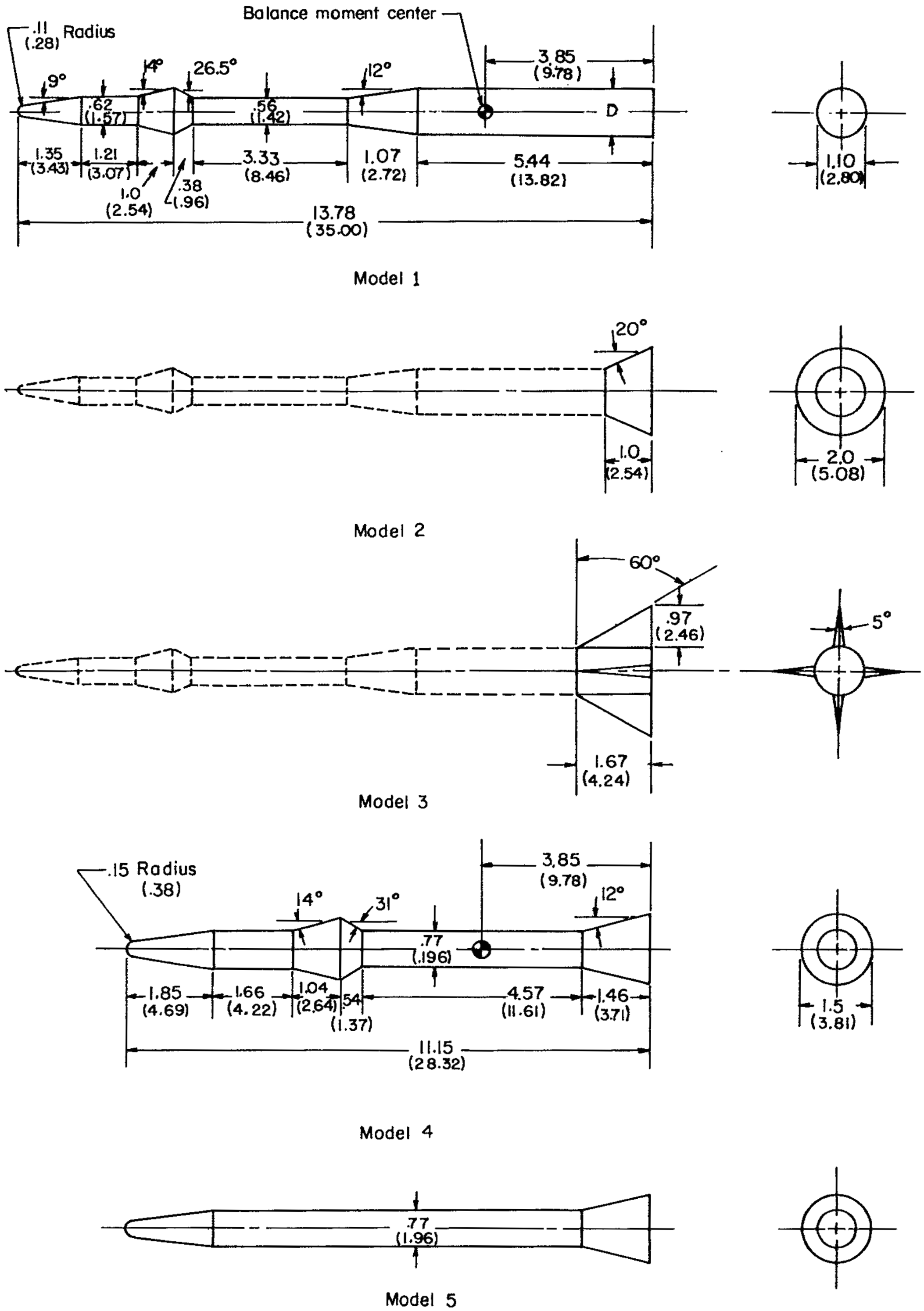

Figure 1.- Sketch of test models. Linear dimensions are given in inches and parenthetically in centimeters.

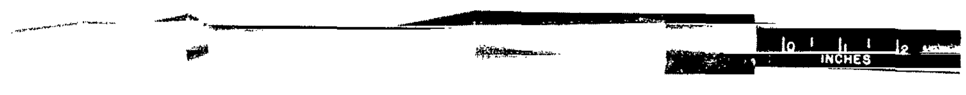

Model 1

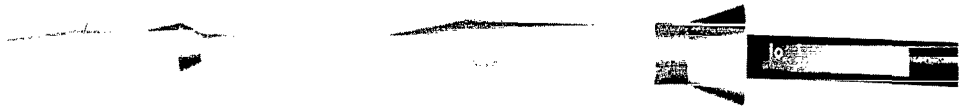

Model 2

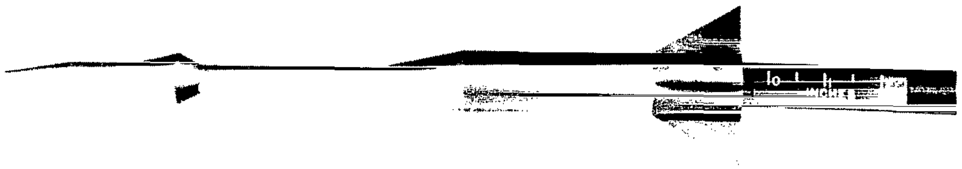

Model 3

Model 4

Model 5

Figure 2.- Photographs of test models.

L-67-977

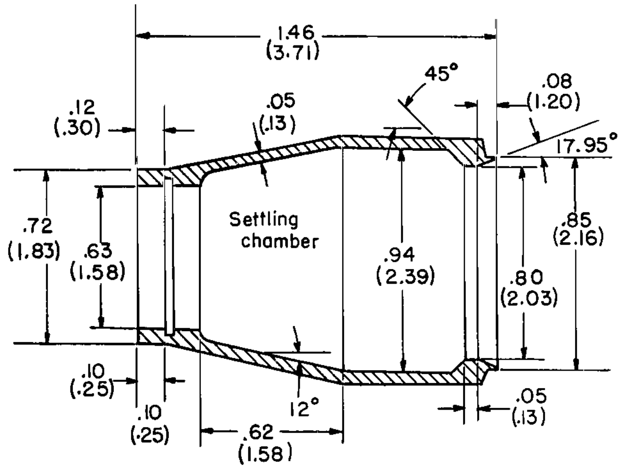

(a) $M_j = 2.24$.

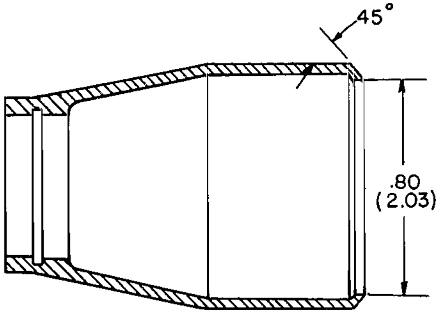

(b) $M_j = 1.0$.

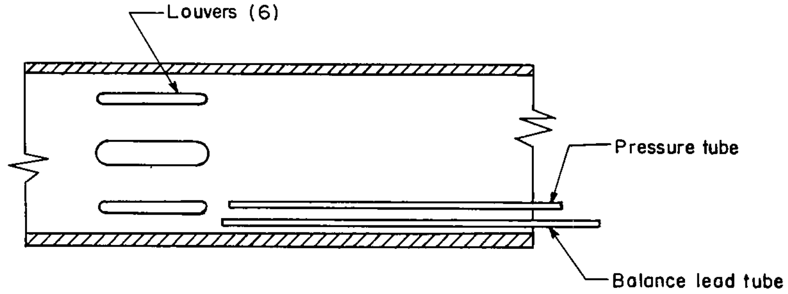

(c) Sting cutaway.

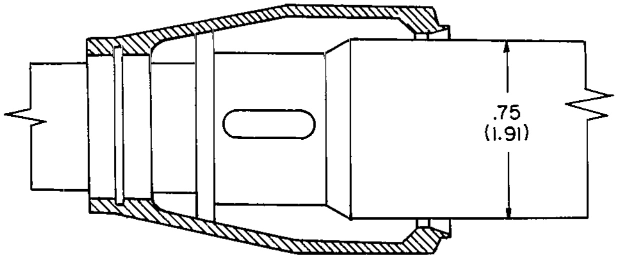

(d) Assembly of $M_j = 2.24$ nozzle and sting.

Figure 3.- Sketch of test nozzles and sting. Linear dimensions are given in inches and parenthetically in centimeters.

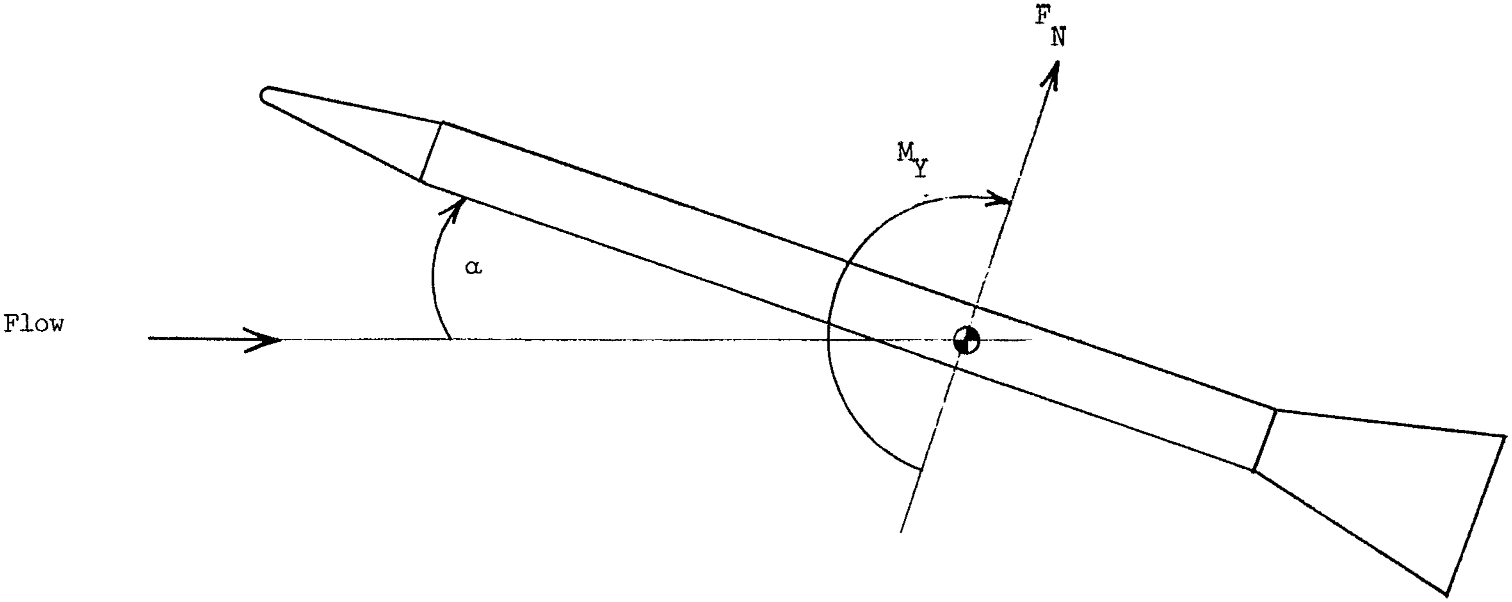

Figure 4.- Body-axis system. Arrows indicate positive direction.

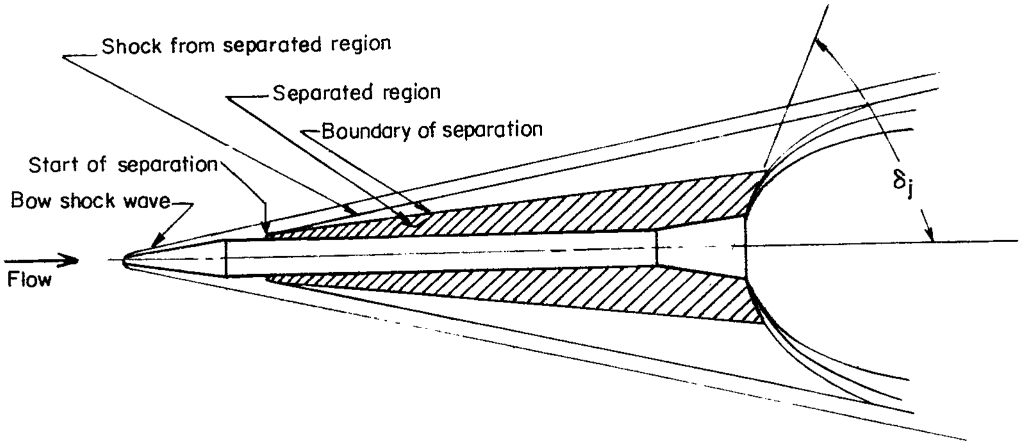

(a) Low angle of attack.

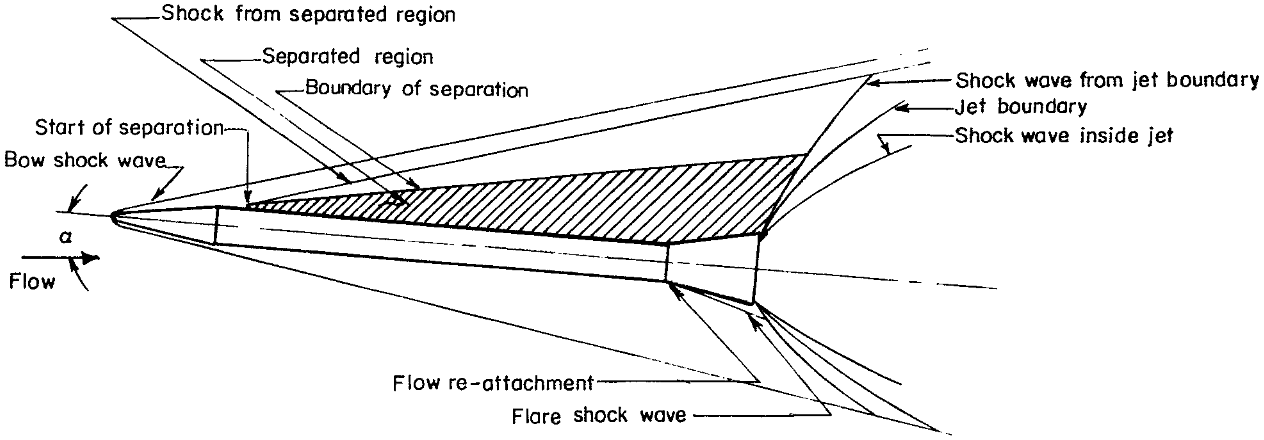

(b) High angle of attack.

Figure 5.- Schematic representation of the flow-field nomenclature.

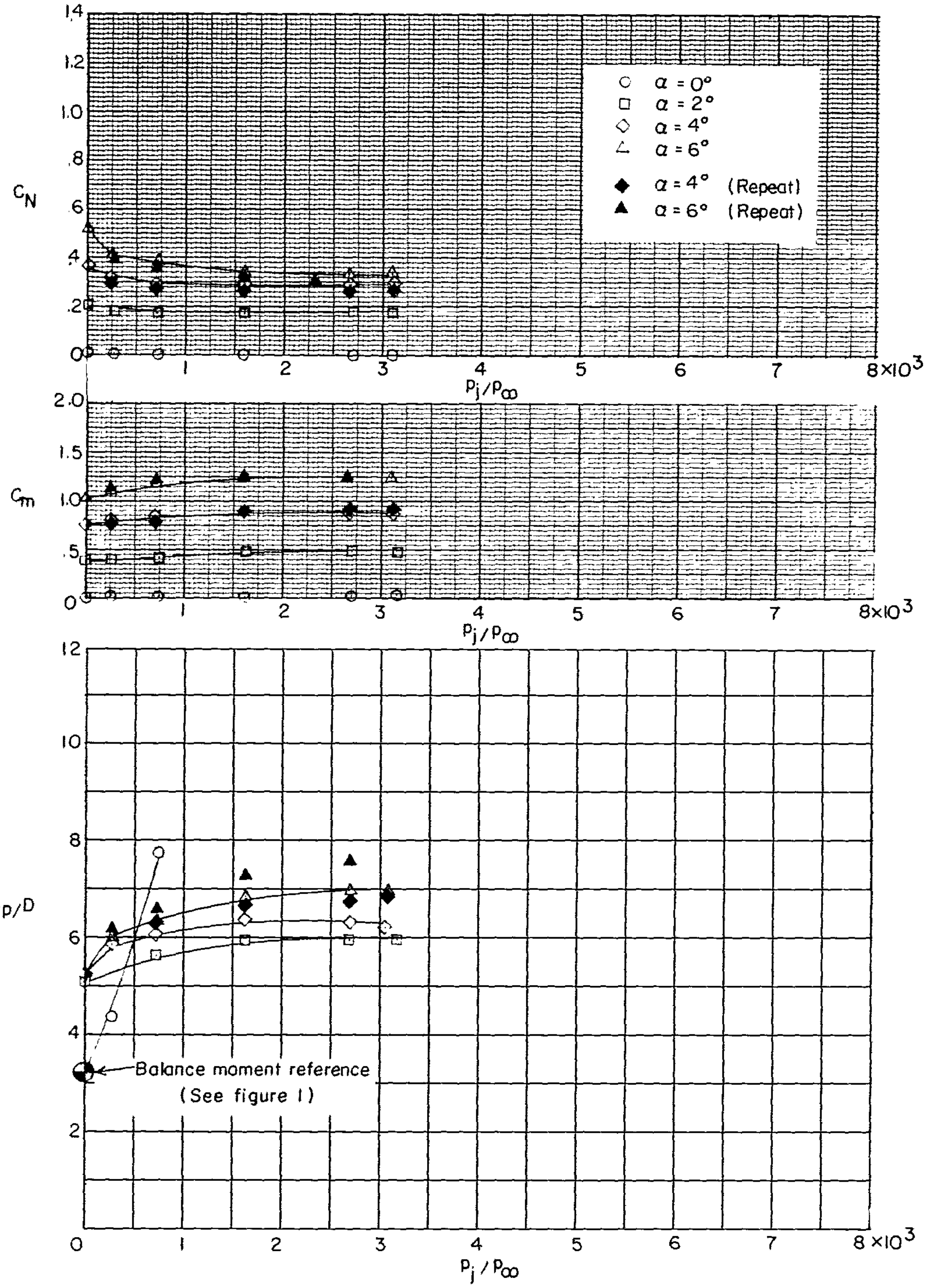

(a) $M_\infty = 4$; $M_j = 2.24$.

Figure 6.- The variation of C_N, C_m, and x_{cp}/D with pressure ratio and angle of attack for model 1, including schlieren photographs.

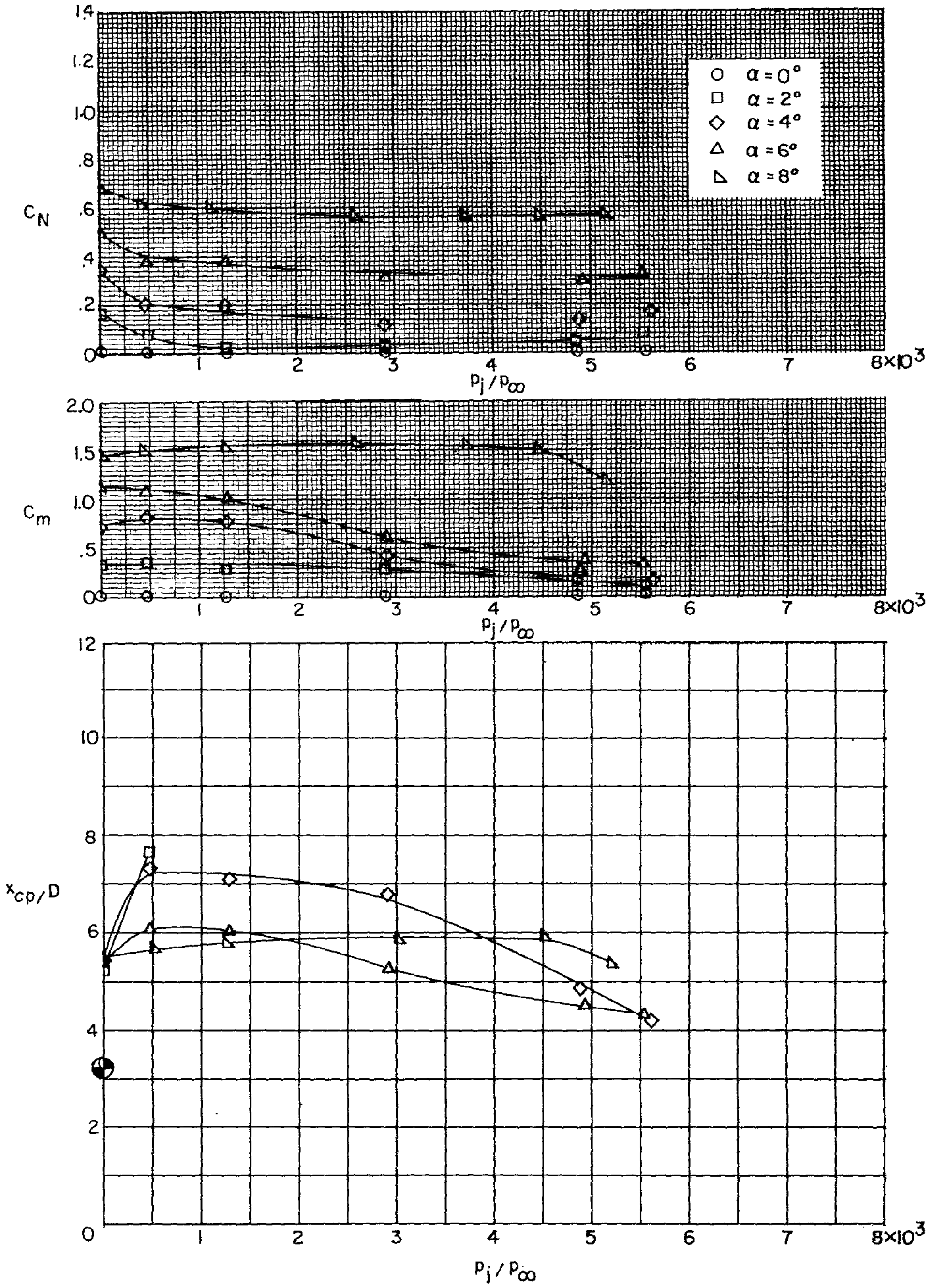

(b) $M_\infty = 5$; $M_j = 2.24$.

Figure 6.- Continued.

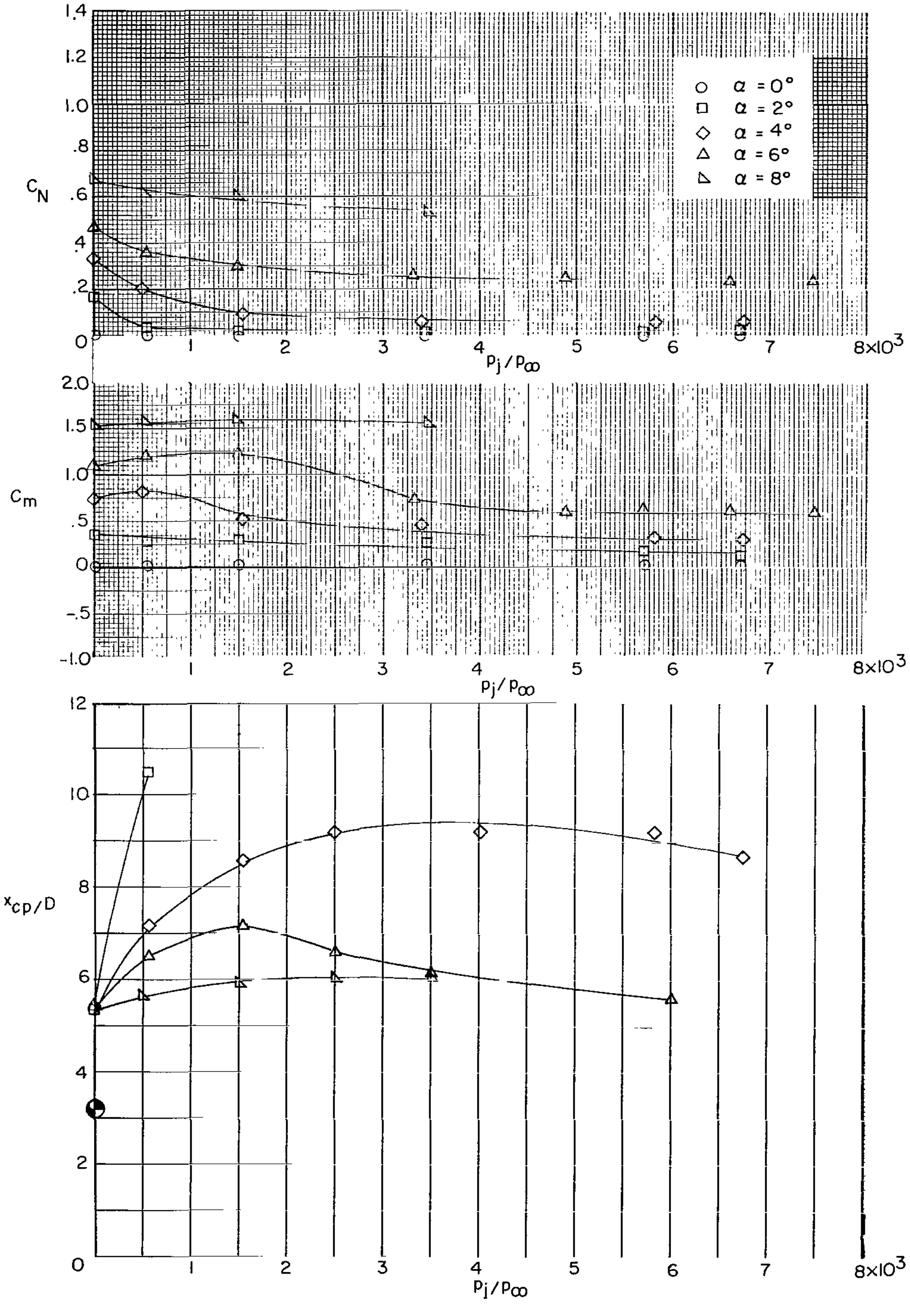

(c) $M_\infty = 6$; $M_j = 2.24$.

Figure 6.- Continued.

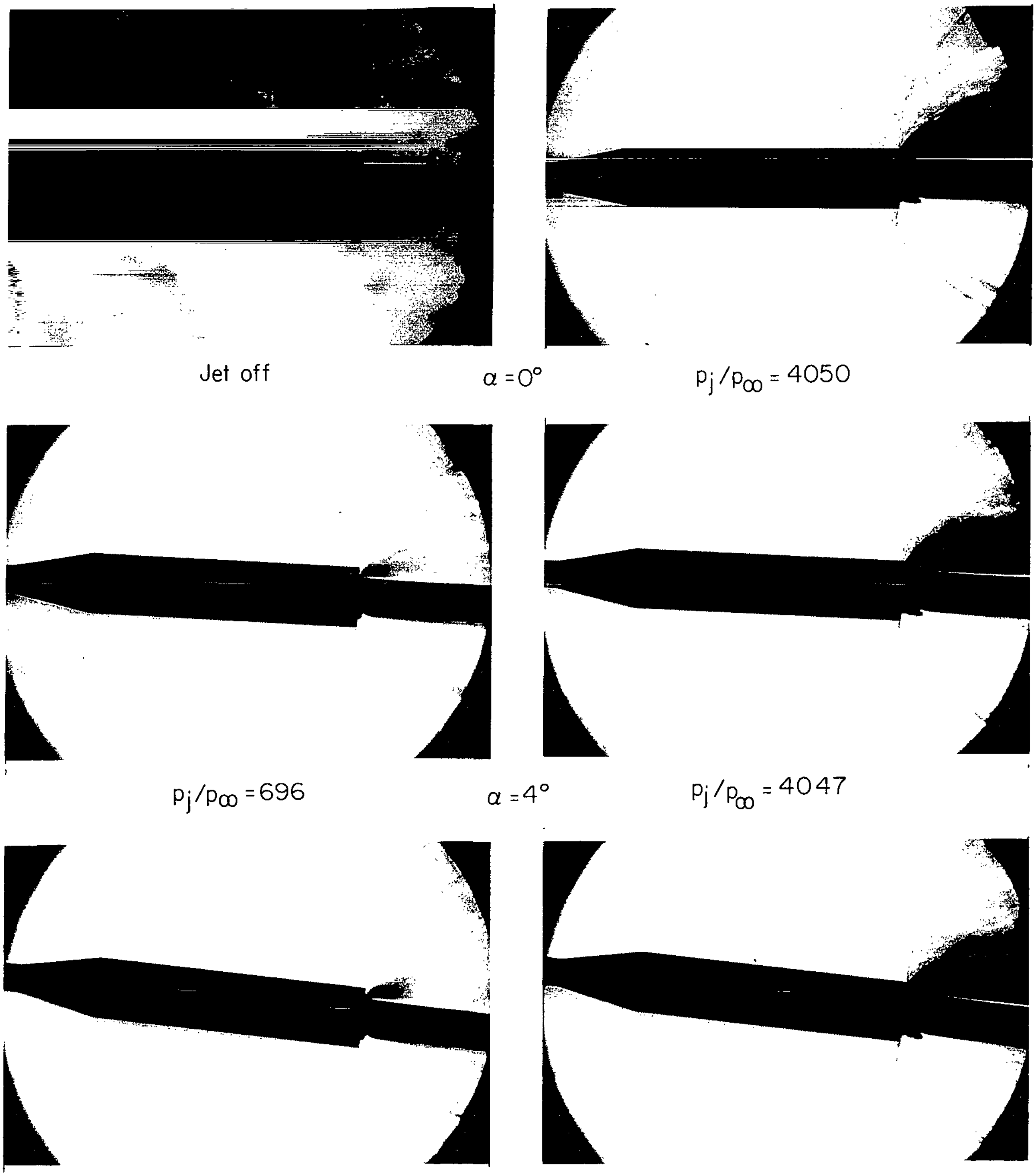

Jet off $\alpha = 0^\circ$ $p_j/p_\infty = 4050$

$p_j/p_\infty = 696$ $\alpha = 4^\circ$ $p_j/p_\infty = 4047$

$p_j/p_\infty = 720$ $\alpha = 6^\circ$ $p_j/p_\infty = 4040$

(d) Schlieren photographs. $M_\infty = 4$; $M_j = 2.24$.

L-67-978

Figure 6.- Continued.

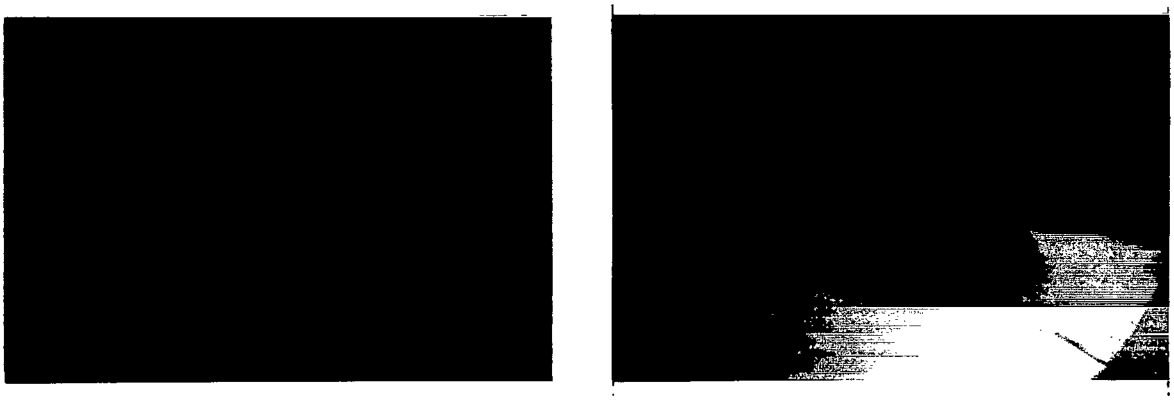

Jet off $\alpha = 0^\circ$ $p_j/p_\infty = 5912$

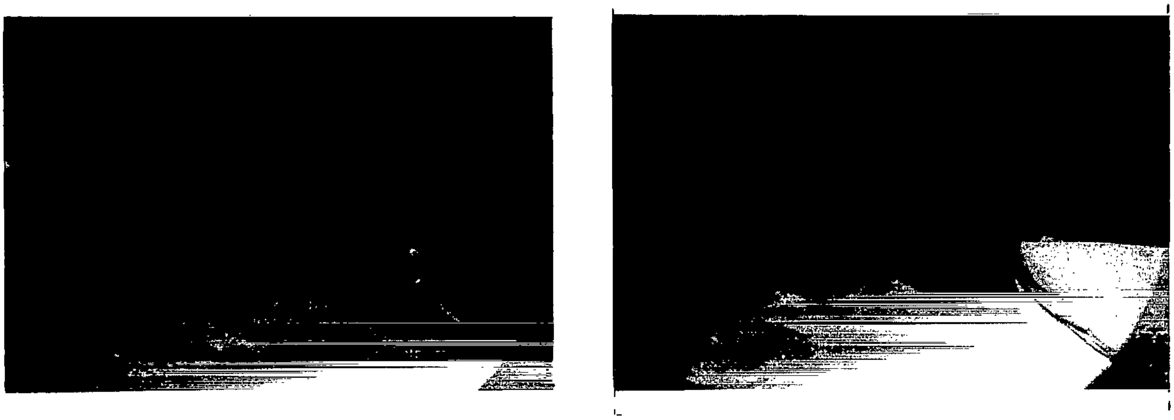

$p_j/p_\infty = 470$ $\alpha = 4^\circ$ $p_j/p_\infty = 5642$

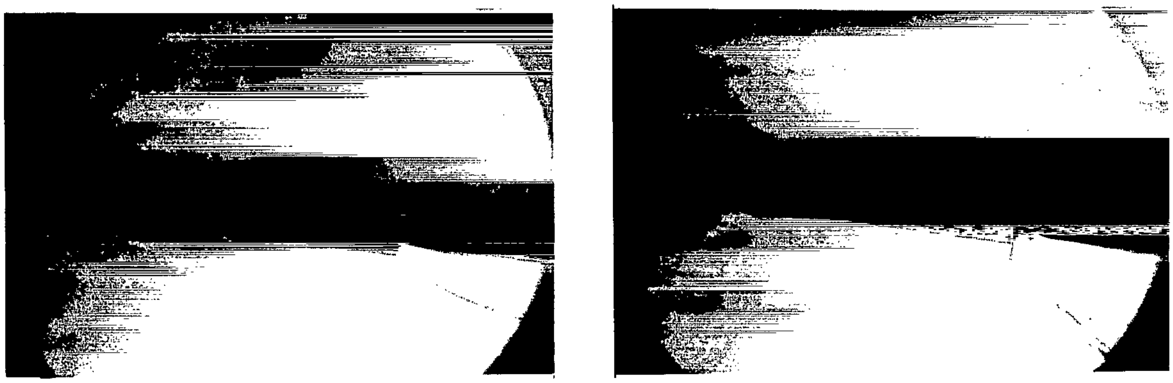

$p_j/p_\infty = 425$ $\alpha = 8^\circ$ $p_j/p_\infty = 5160$

(e) Schlieren photographs. $M_\infty = 5$; $M_j = 2.24$. L-67-979

Figure 6.- Continued.

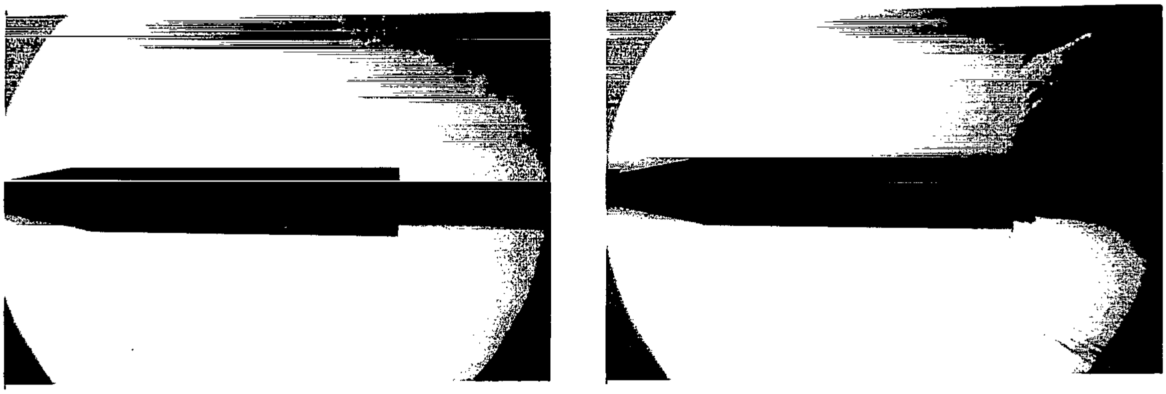

Jet off $\alpha = 0°$ $p_j/p_\infty = 7830$

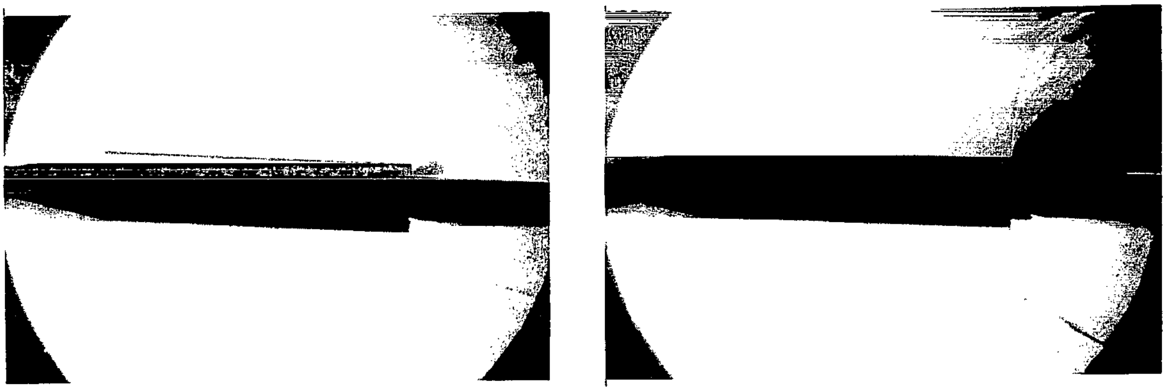

$p_j/p_\infty = 550$ $\alpha = 2°$ $p_j/p_\infty = 6898$

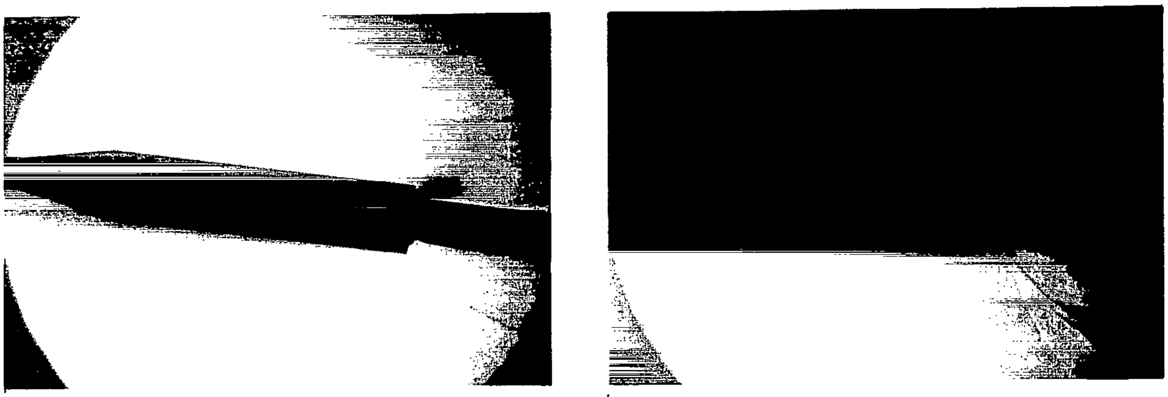

$p_j/p_\infty = 1550$ $\alpha = 6°$ $p_j/p_\infty = 7450$

(f) Schlieren photographs. $M_\infty = 6$; $M_j = 2.24$.

L-67-980

Figure 6.- Concluded.

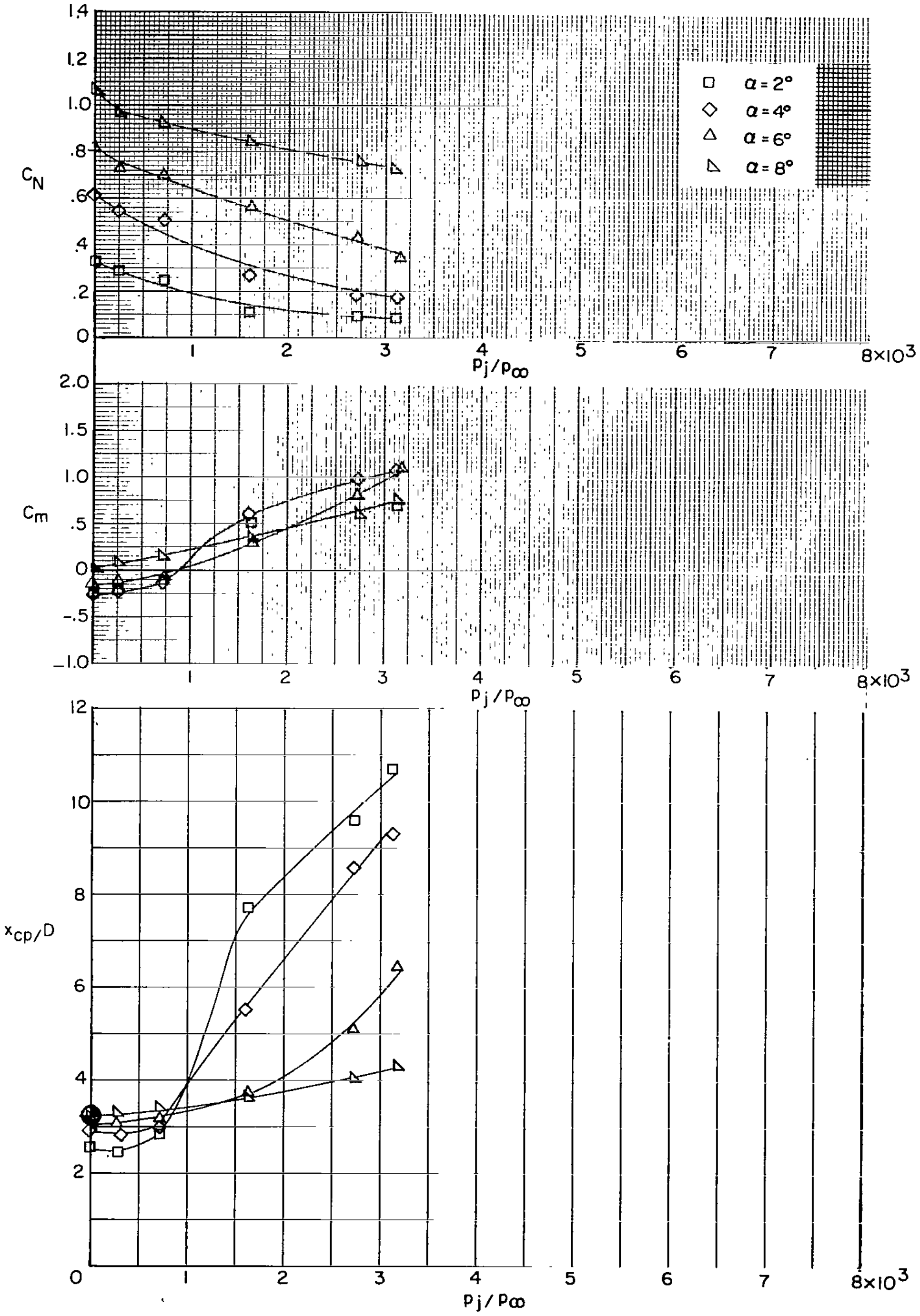

(a) $M_\infty = 4$; $M_j = 2.24$.

Figure 7.- The variation of C_N, C_m, and x_{cp}/D with pressure ratio and angle of attack for model 2, including schlieren photographs.

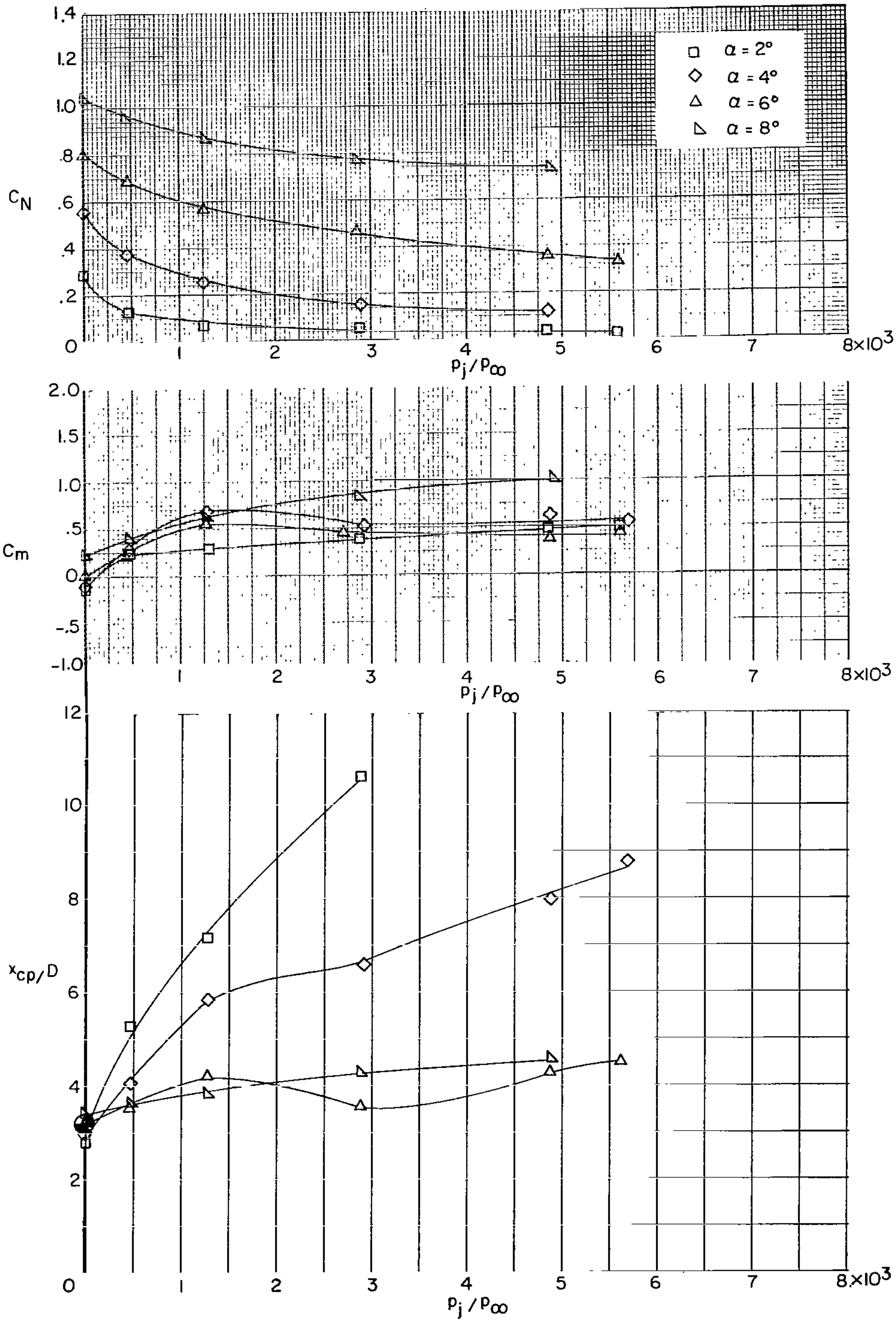

(b) $M_\infty = 5$; $M_j = 2.24$.

Figure 7.- Continued.

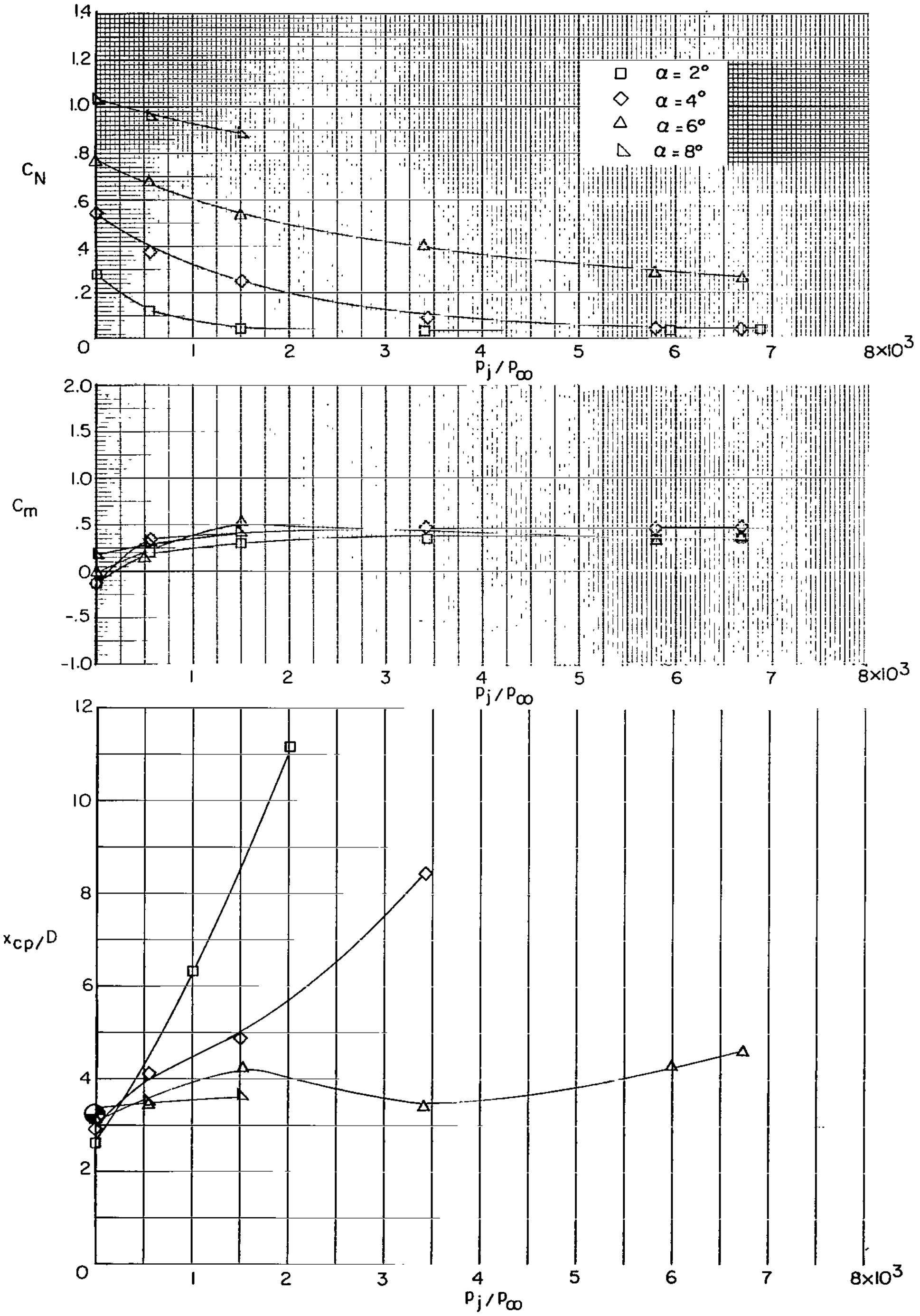

(c) $M_\infty = 6$; $M_j = 2.24$.

Figure 7.- Continued.

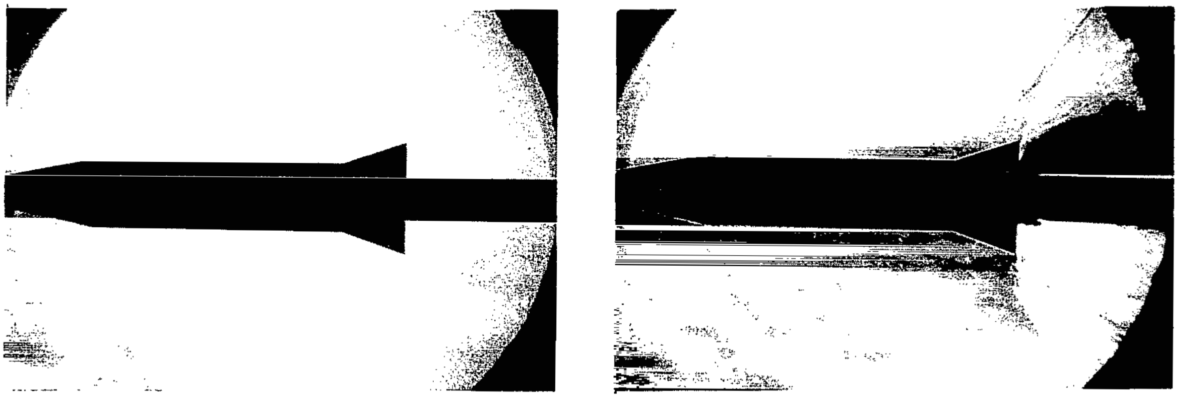

Jet off $\alpha = 0°$ $p_j/p_\infty = 4061$

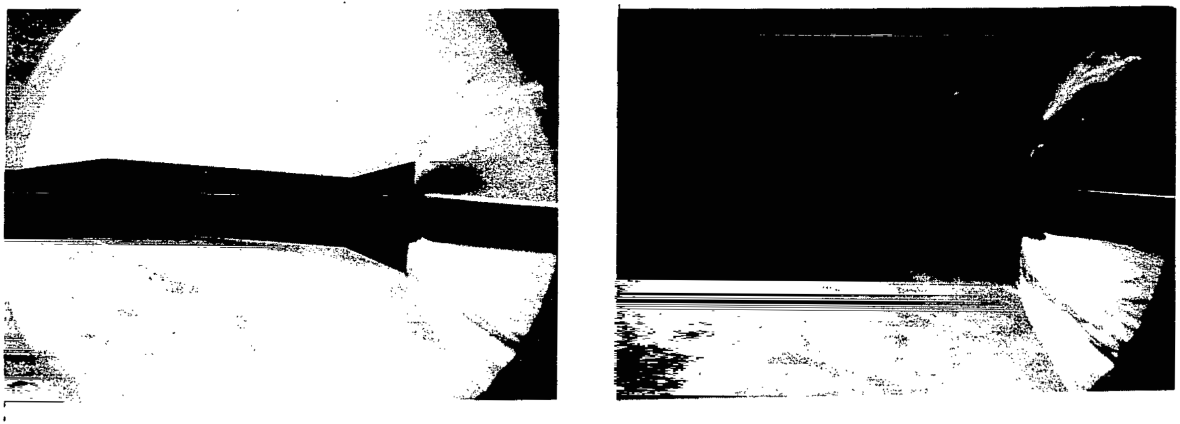

$p_j/p_\infty = 1600$ $\alpha = 4°$ $p_j/p_\infty = 3791$

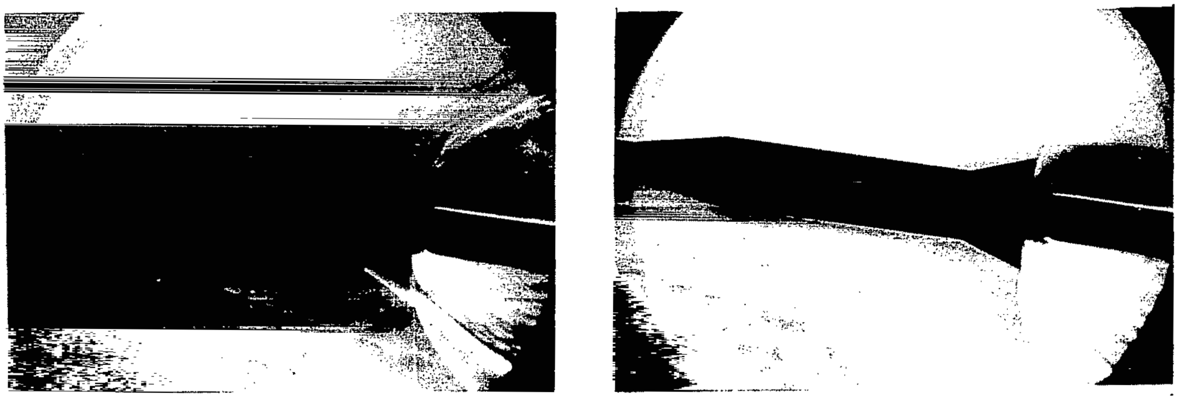

$p_j/p_\infty = 1600$ $\alpha = 8°$ $p_j/p_\infty = 4004$

(d) Schlieren photographs. $M_\infty = 4$; $M_j = 2.24$.

L-67-981

Figure 7.- Continued.

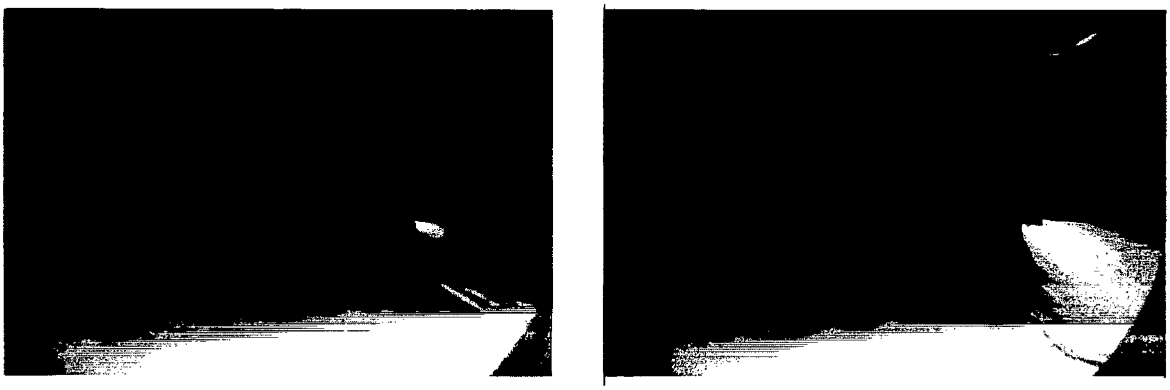

$p_j/p_\infty = 572$ $\alpha = 0°$ $p_j/p_\infty = 7878$

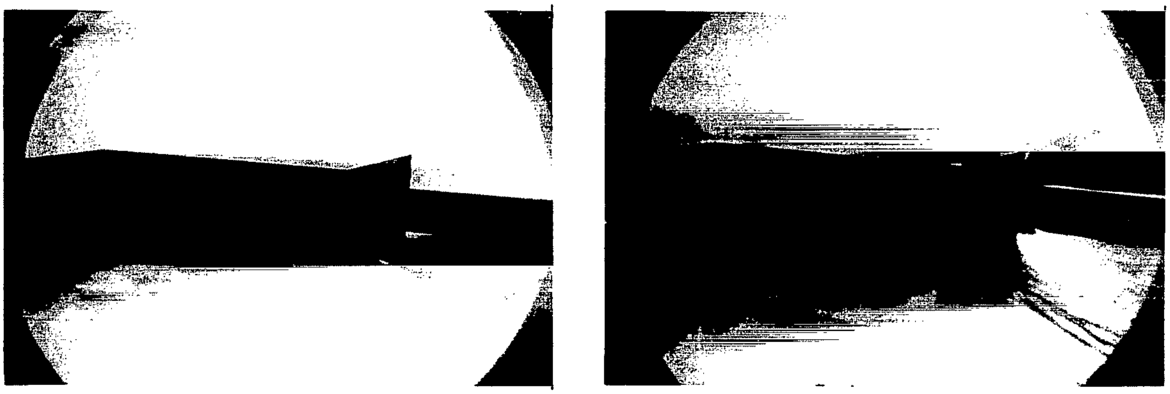

Jet off $\alpha = 4°$ $p_j/p_\infty = 7181$

$p_j/p_\infty = 550$ $\alpha = 6°$ $p_j/p_\infty = 7511$

(e) Schlieren photographs. $M_\infty = 6$; $M_j = 2.24$. L-67-982

Figure 7.- Concluded.

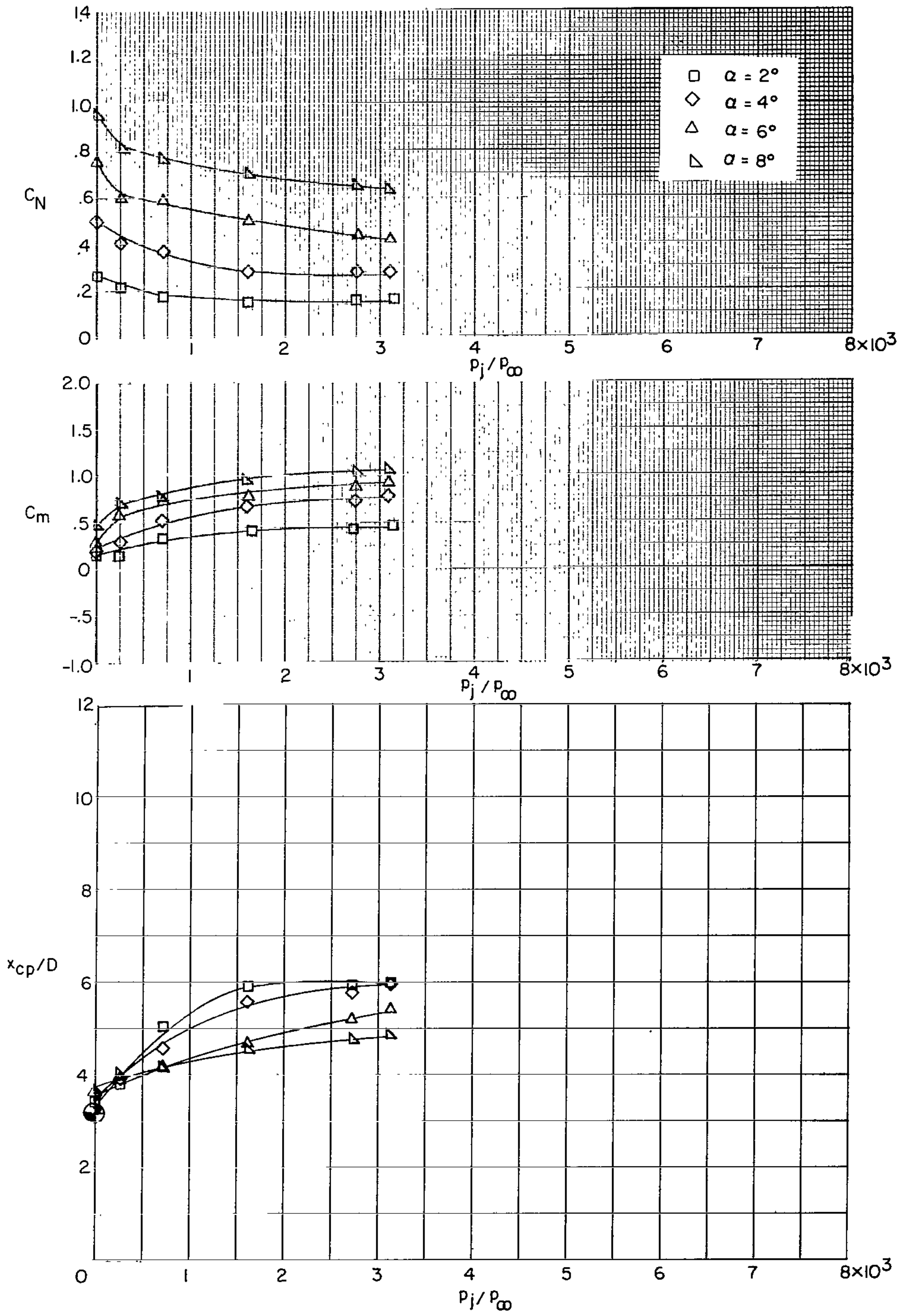

(a) $M_\infty = 4$; $M_j = 2.24$.

Figure 8.- The variation of C_N, C_m, and x_{cp}/D with pressure ratio and angle of attack for model 3, including schlieren photographs.

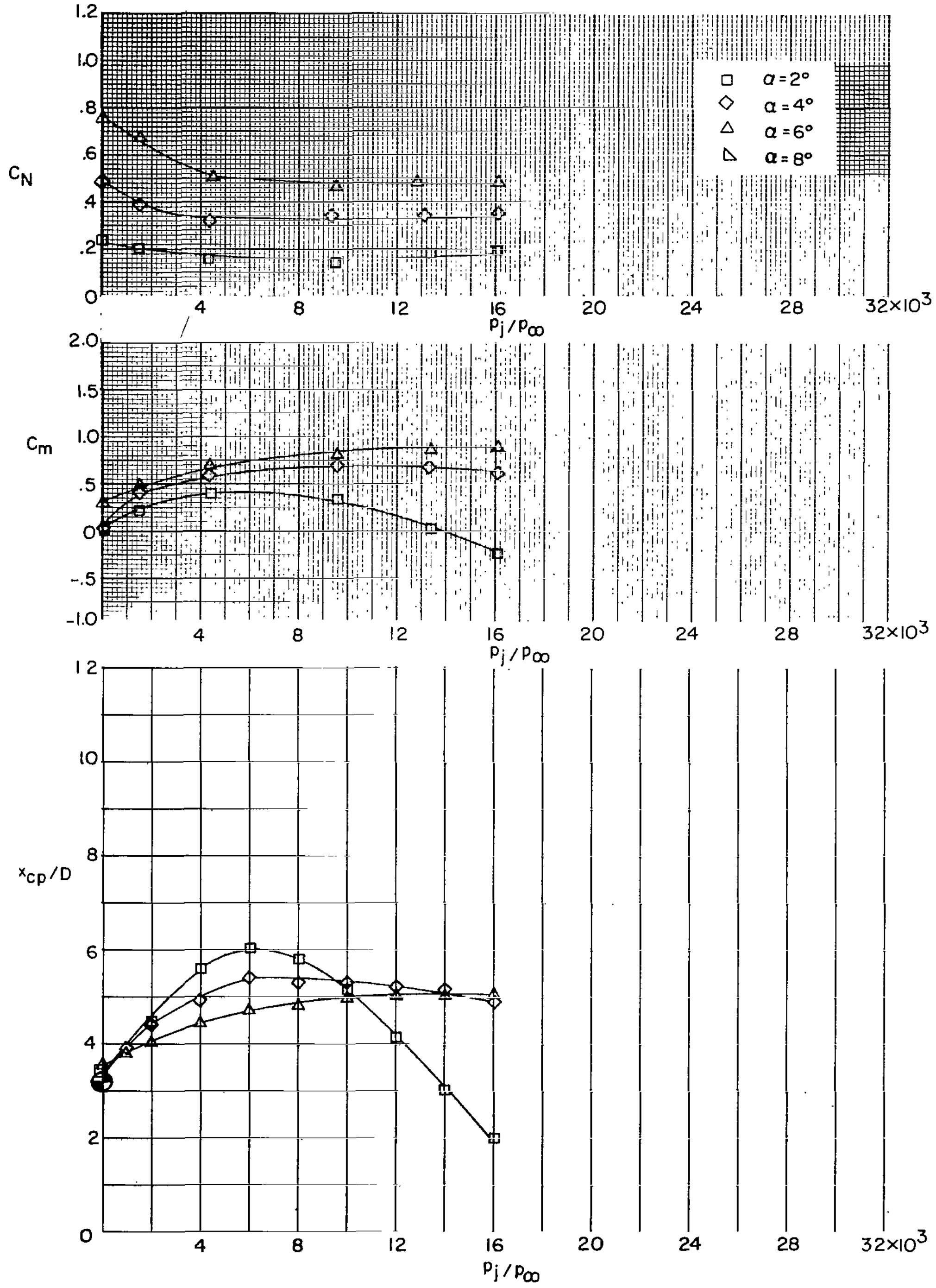

(b) $M_\infty = 4$; $M_j = 1.0$.

Figure 8.- Continued.

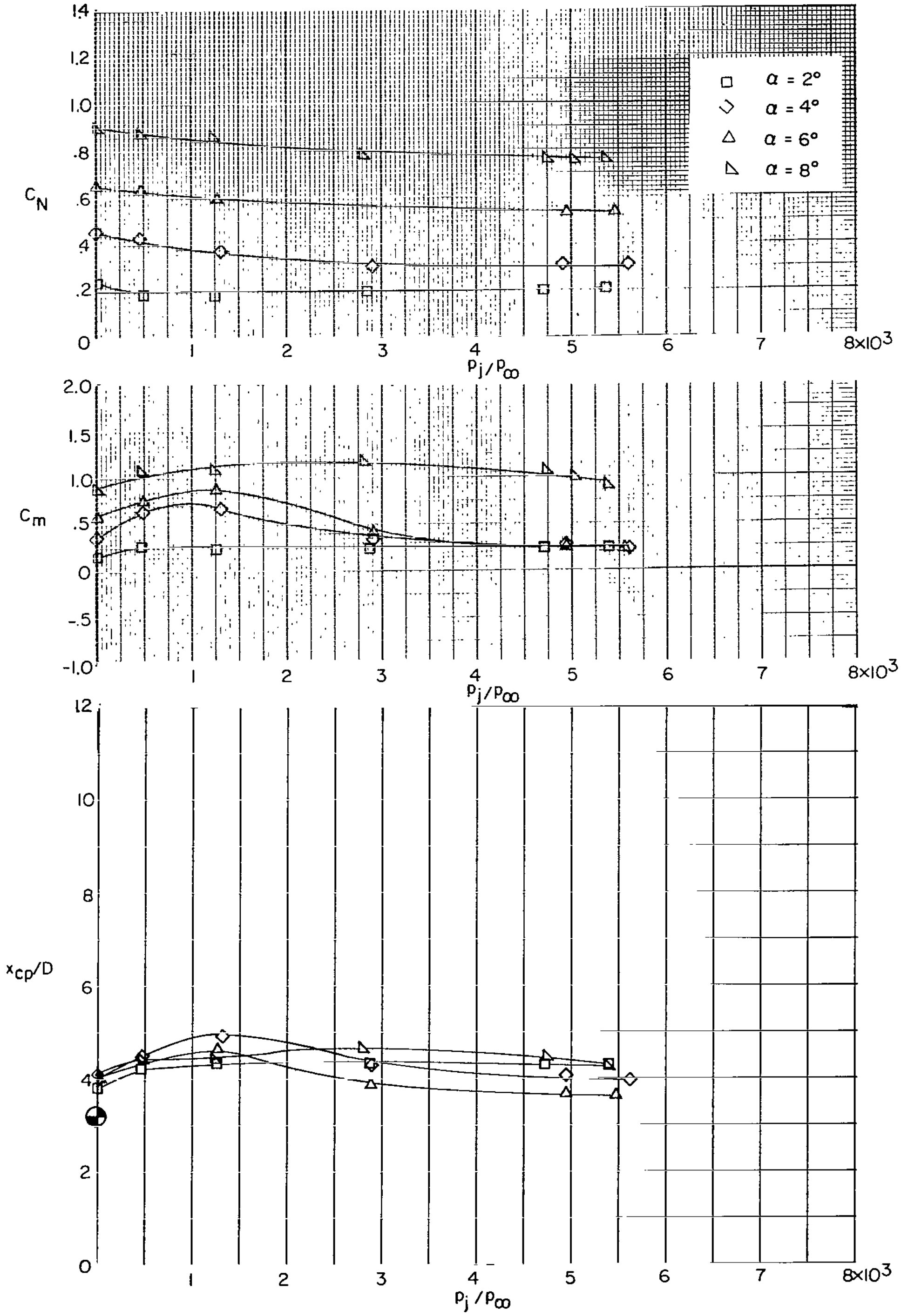

(c) $M_\infty = 5$; $M_j = 2.24$.

Figure 8.- Continued.

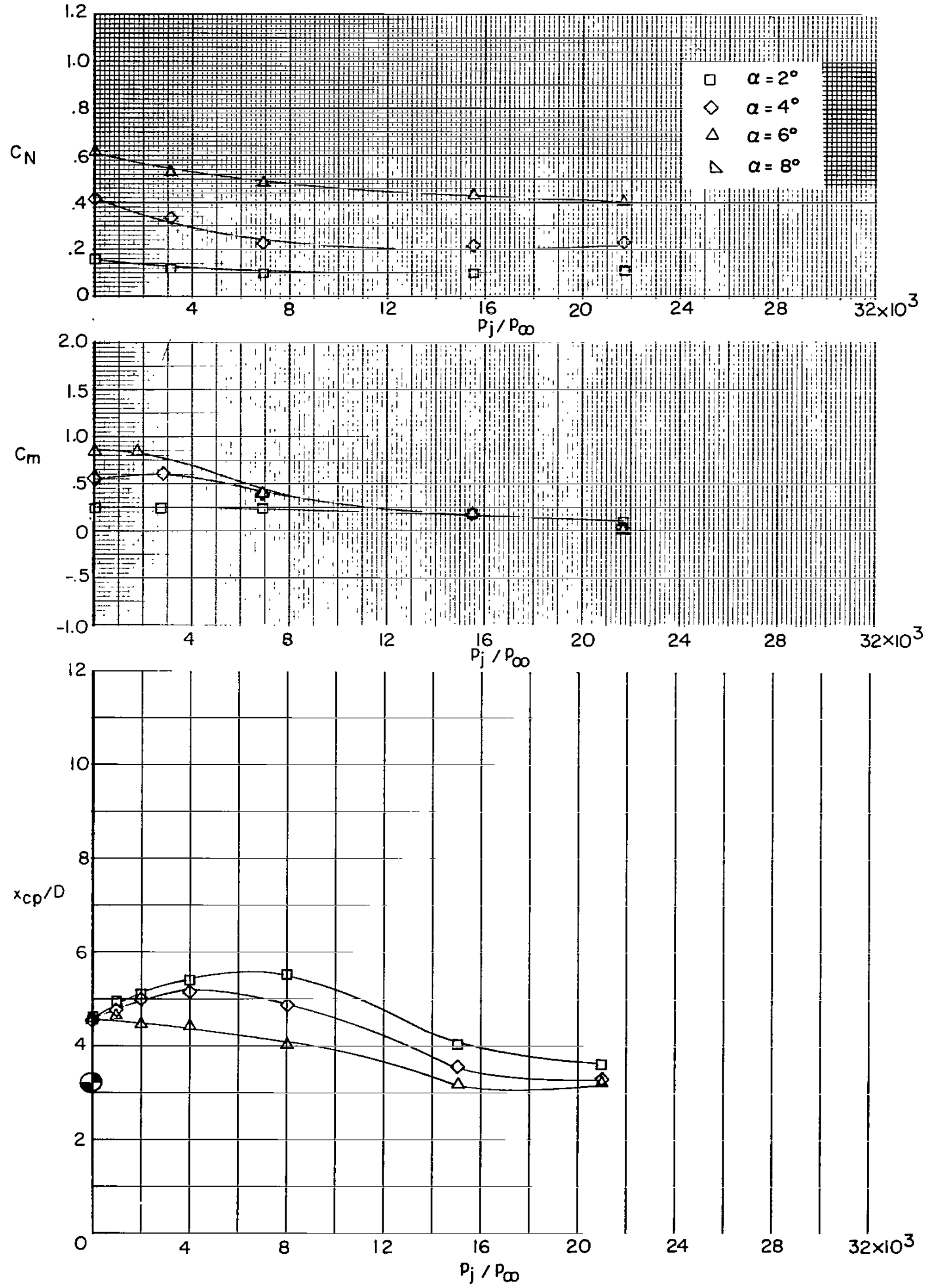

(d) $M_\infty = 5$; $M_j = 1.0$.

Figure 8.- Continued.

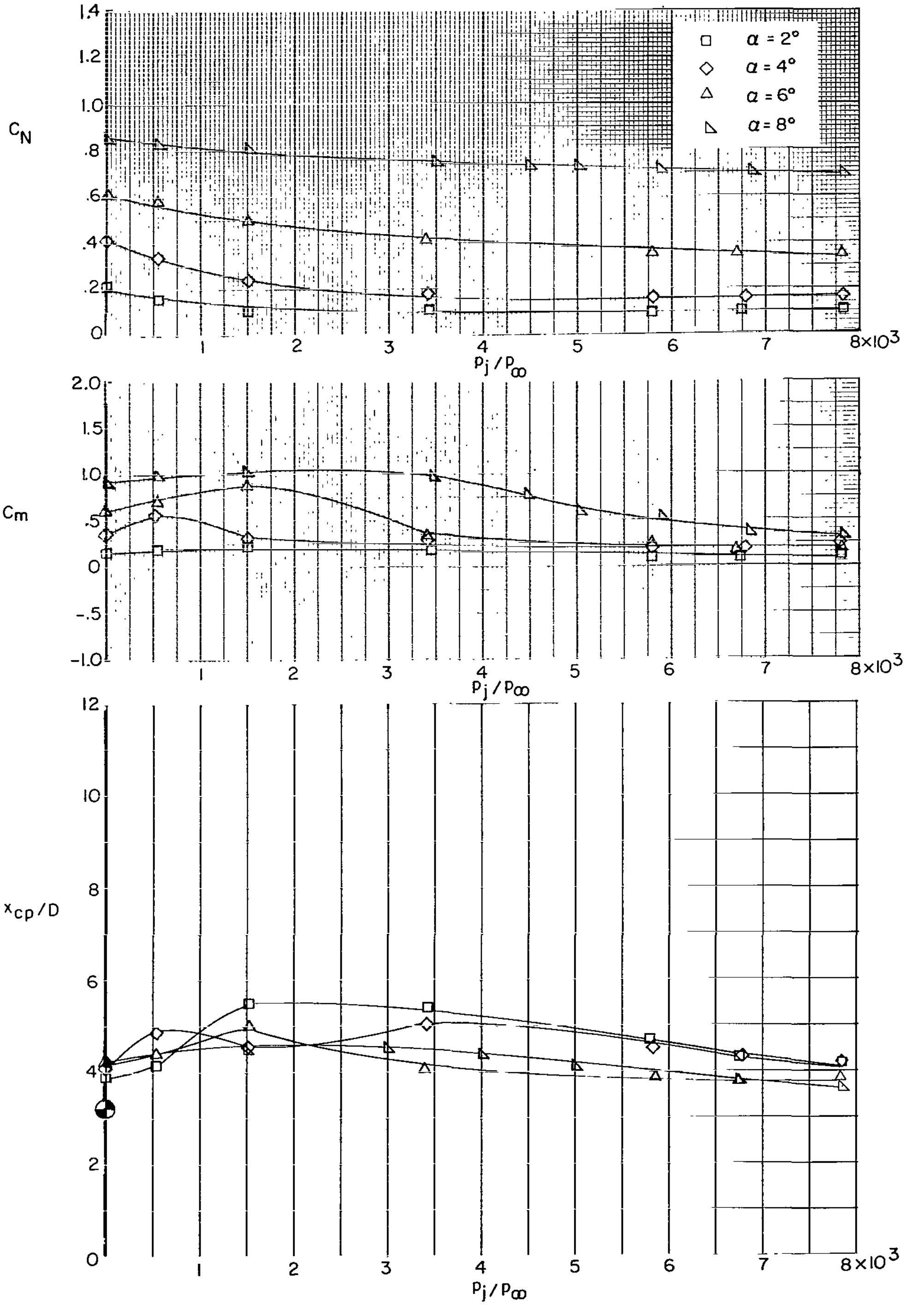

(e) $M_\infty = 6$; $M_j = 2.24$.

Figure 8.- Continued.

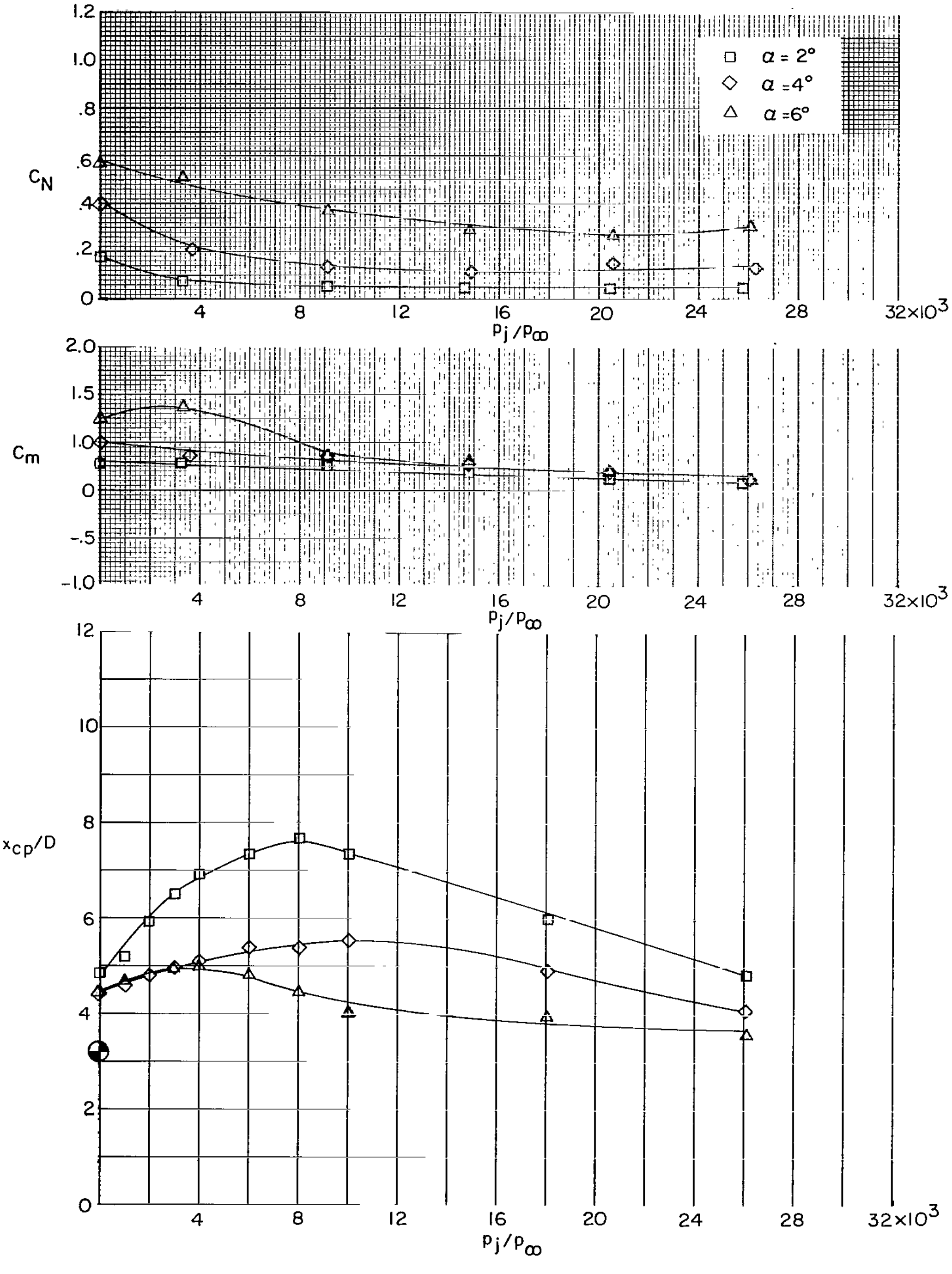

(f) $M_\infty = 6$; $M_j = 1.0$.

Figure 8.- Continued.

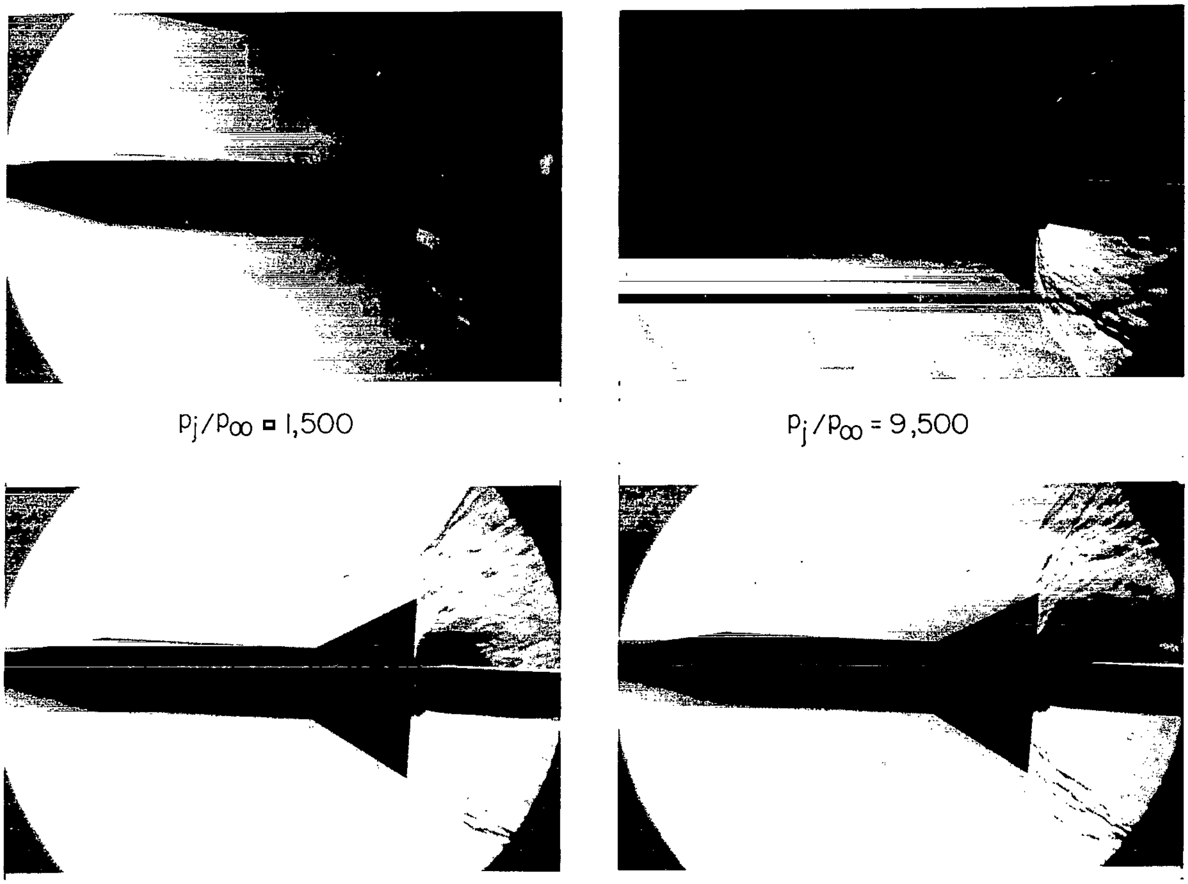

$p_j/p_\infty = 1{,}500$

$p_j/p_\infty = 9{,}500$

$p_j/p_\infty = 13{,}400$

$\alpha = 2°$

$p_j/p_\infty = 16{,}100$

(g) Schlieren photographs. $M_\infty = 4$; $M_j = 1.0$.

L-67-983

Figure 8.- Continued.

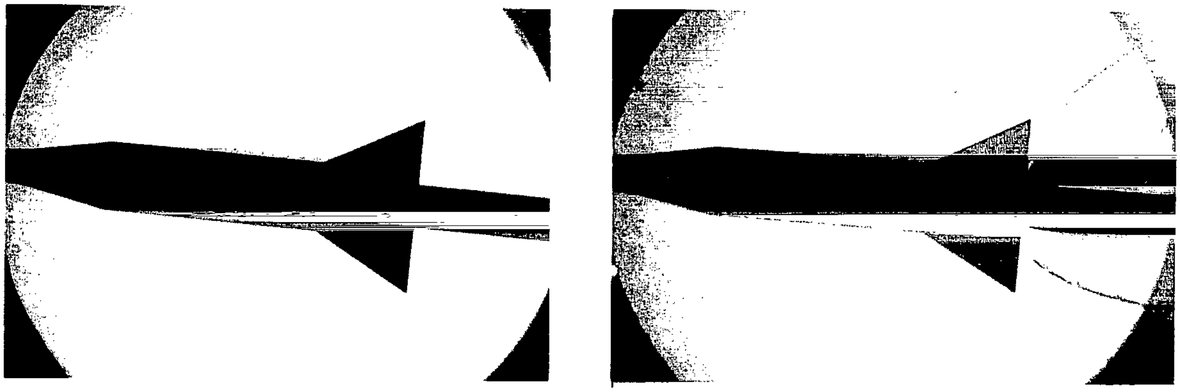

Jet off

$p_j/p_\infty = 1{,}500$

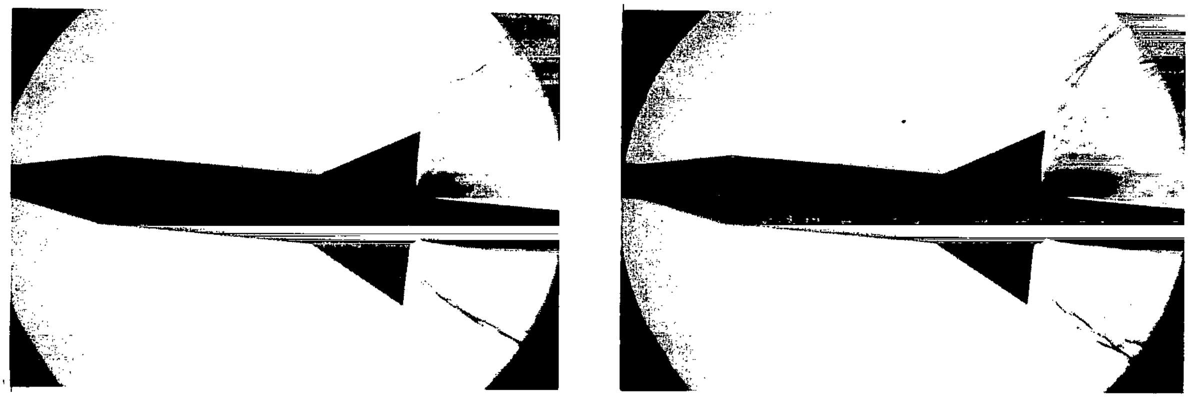

$p_j/p_\infty = 4100$

$p_j/p_\infty = 9400$

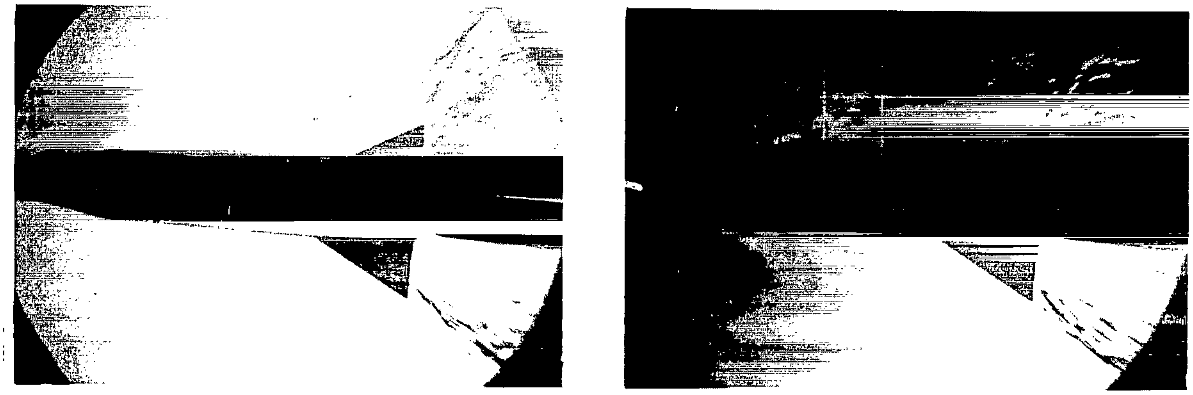

$p_j/p_\infty = 13{,}100$

$\alpha = 4^\circ$

$p_j/p_\infty = 16{,}100$

(h) Schlieren photographs. $M_\infty = 4$; $M_j = 1.0$. L-67-984

Figure 8.- Continued.

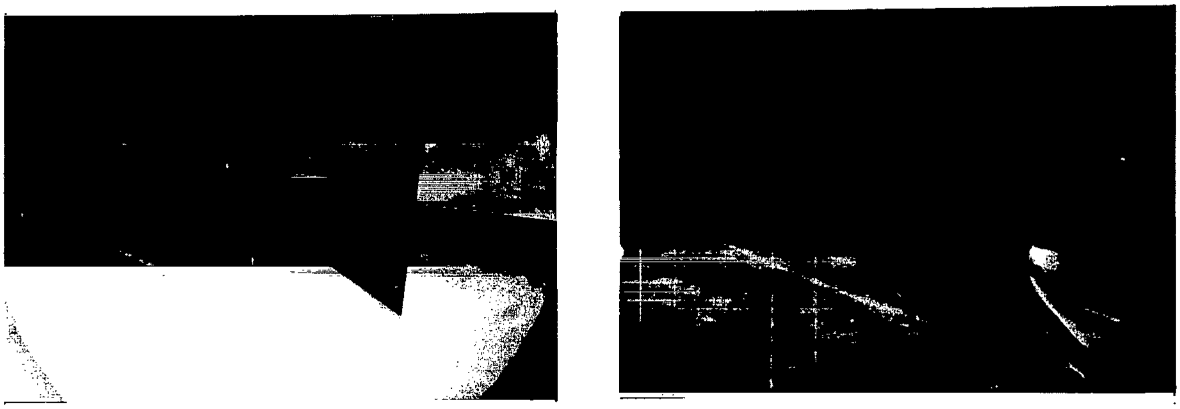

Jet off

$p_j/p_\infty = 1,500$

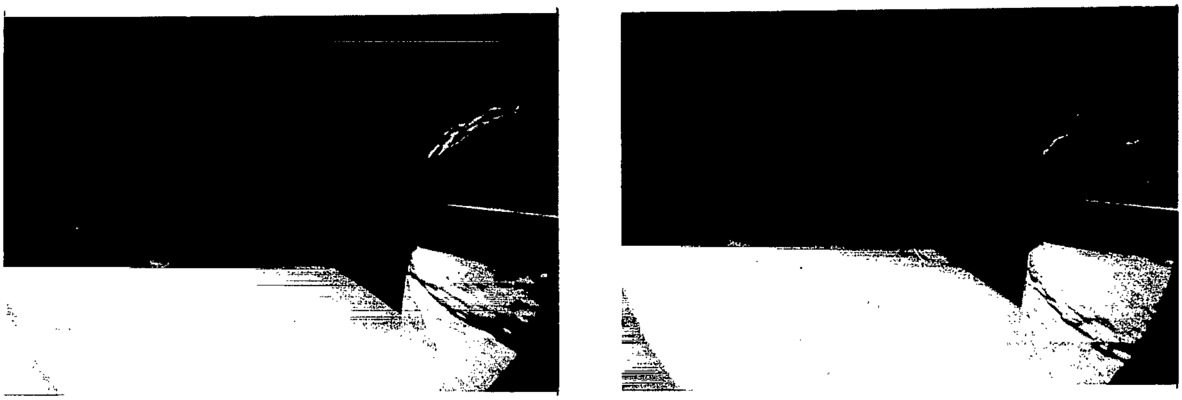

$p_j/p_\infty = 4,312$

$p_j/p_\infty = 9,301$

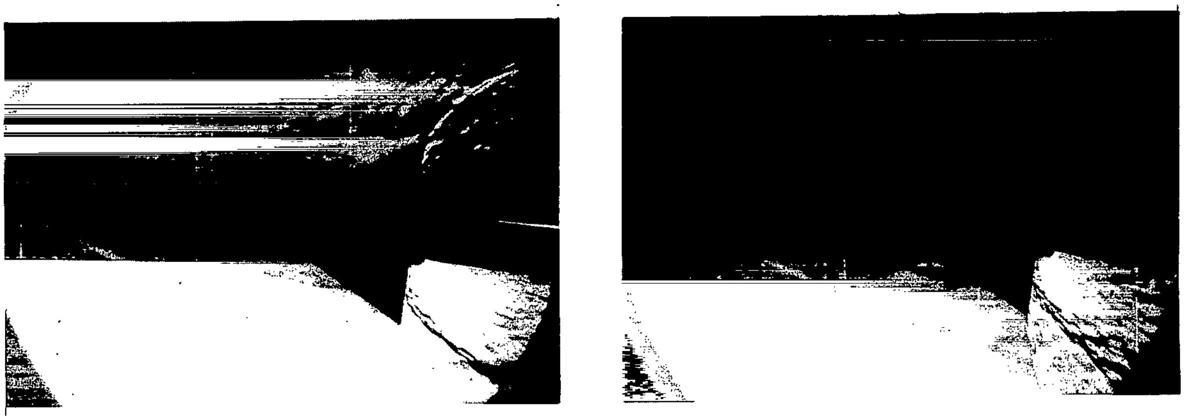

$p_j/p_\infty = 12,800$

$\alpha = 6°$

$p_j/p_\infty = 16,100$

(i) Schlieren photographs. $M_\infty = 4$; $M_j = 1.0$.

L-67-985

Figure 8.- Continued.

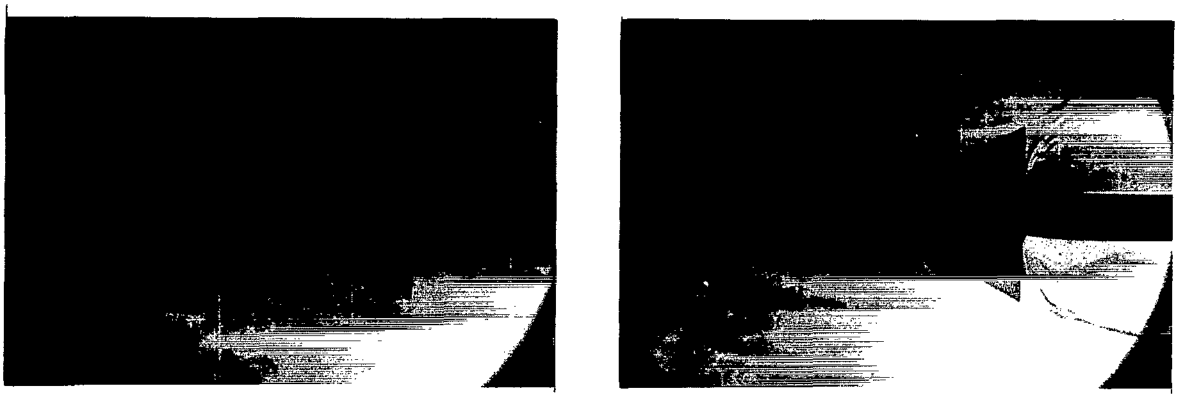

Jet off

$p_j/p_\infty = 2730$

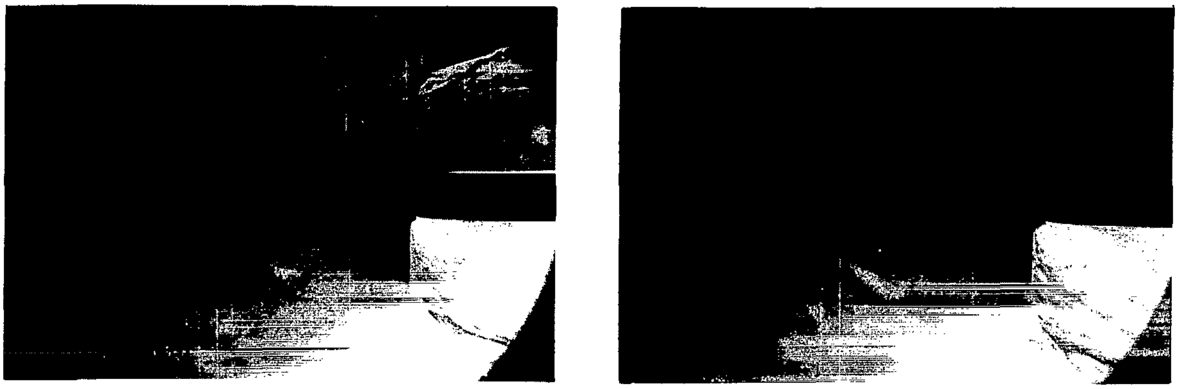

$p_j/p_\infty = 6845$

$p_j/p_\infty = 15{,}646$

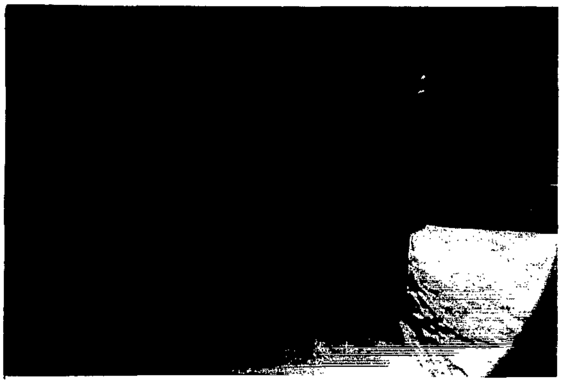

$p_j/p_\infty = 22{,}797$
$\alpha = 0^\circ$

(j) Schlieren photographs. $M_\infty = 5$; $M_j = 1.0$.

L-67-986

Figure 8.- Continued.

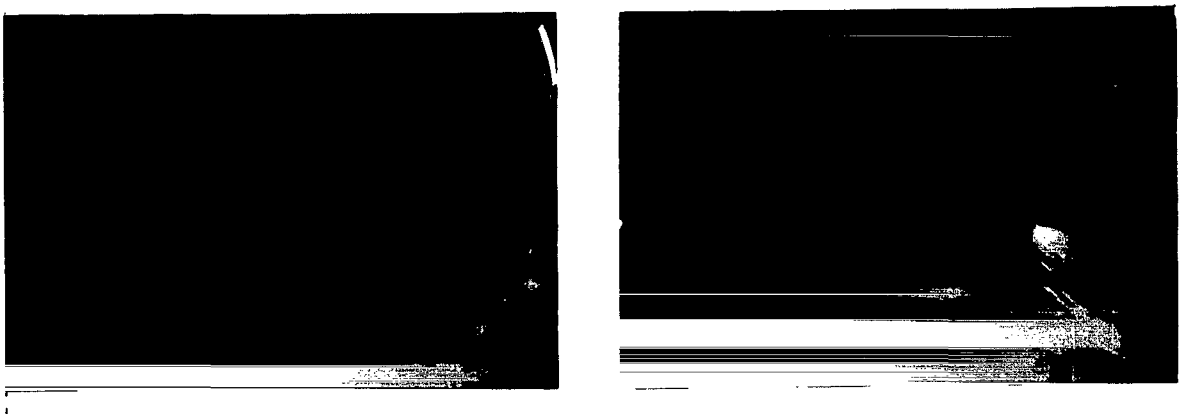

Jet off

$p_j/p_\infty = 2512$

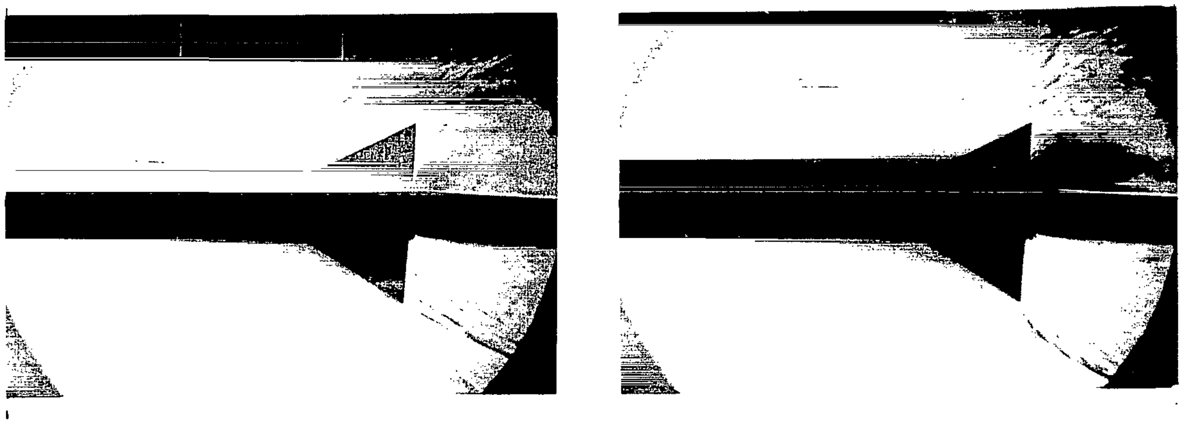

$p_j/p_\infty = 6888$

$p_j/p_\infty = 15{,}551$

$p_j/p_\infty = 21{,}709$
$\alpha = 2°$

(k) Schlieren photographs. $M_\infty = 5$; $M_j = 1.0$.

L-67-987

Figure 8.- Continued.

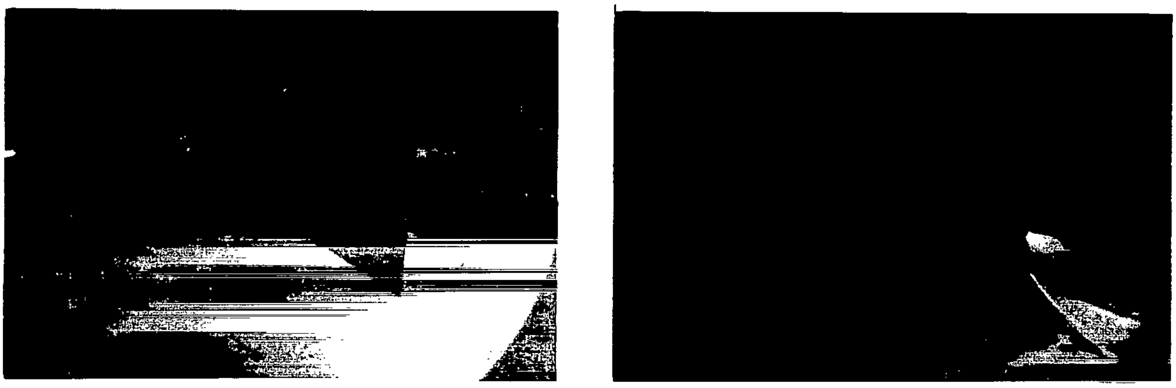

Jet off

$p_j/p_\infty = 2502$

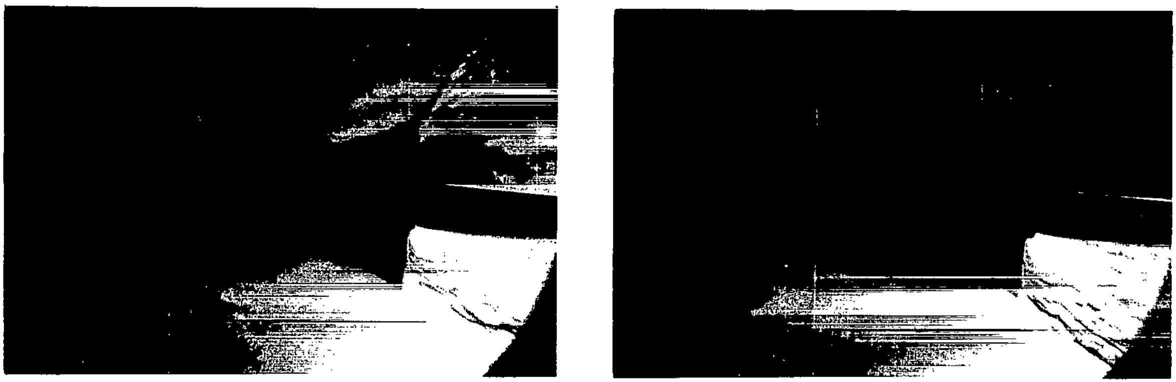

$p_j/p_\infty = 6851$

$p_j/p_\infty = 15{,}474$

$p_j/p_\infty = 21{,}674$
$\alpha = 4^\circ$

(l) Schlieren photographs. $M_\infty = 5$; $M_j = 1.0$.

L-67-988

Figure 8.- Continued.

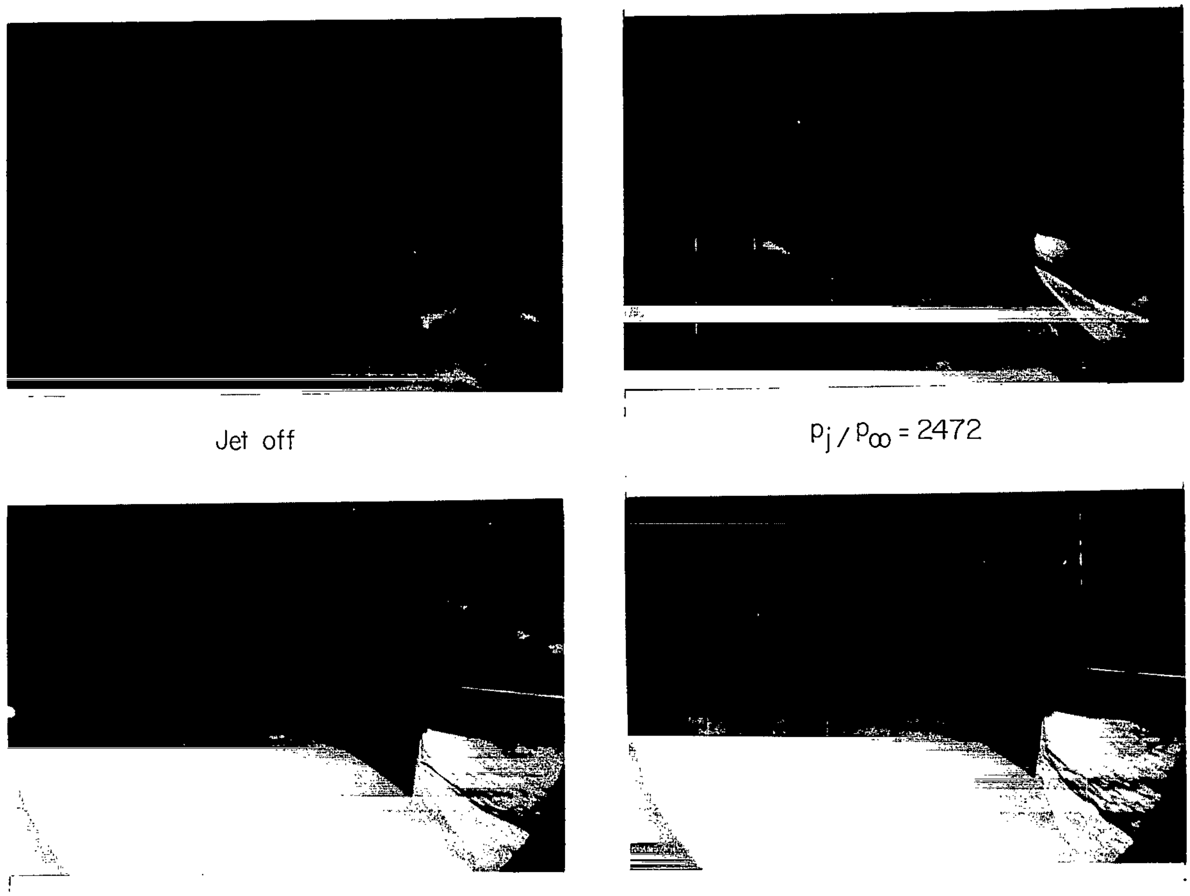

Jet off

$p_j / p_\infty = 2472$

$p_j / p_\infty = 6759$

$\alpha = 6°$

$p_j / p_\infty = 15{,}463$

(m) Schlieren photographs. $M_\infty = 5$; $M_j = 1.0$.

L-67-989

Figure 8.- Continued.

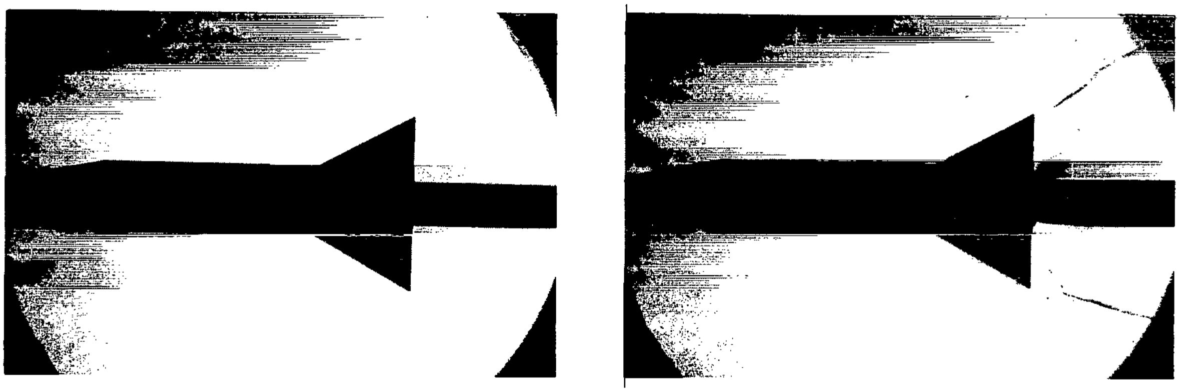

Jet off

$p_j/p_\infty = 3595$

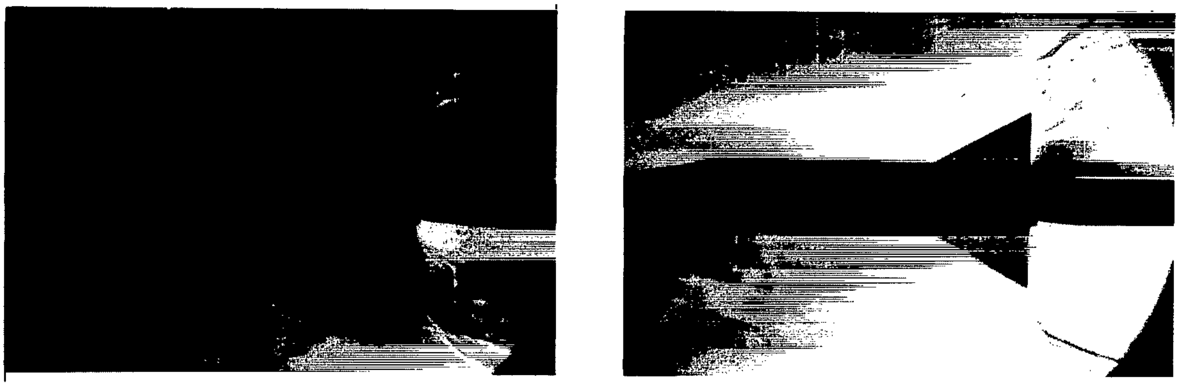

$p_j/p_\infty = 9347$

$p_j/p_\infty = 14{,}746$

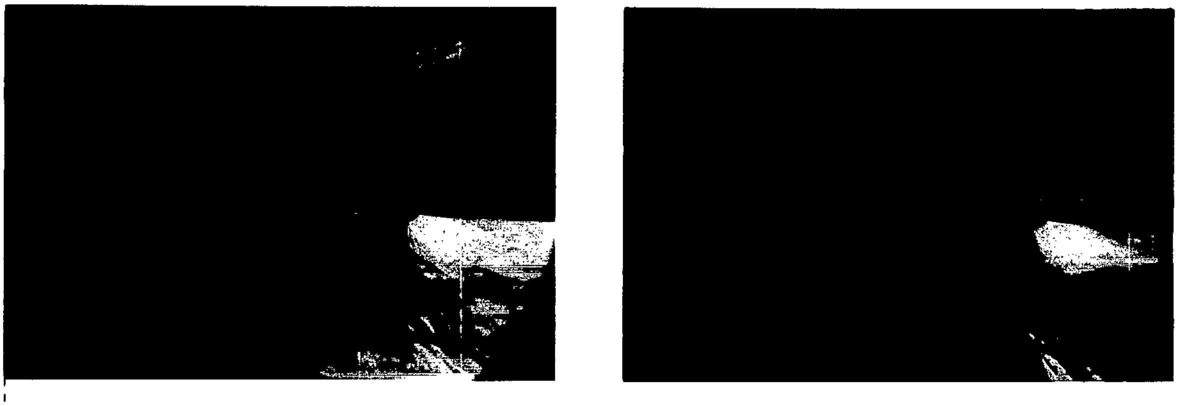

$p_j/p_\infty = 20{,}264$

$\alpha = 0°$

$p_j/p_\infty = 26{,}415$

(n) Schlieren photographs. $M_\infty = 6$; $M_j = 1.0$. L-67-990

Figure 8.- Continued.

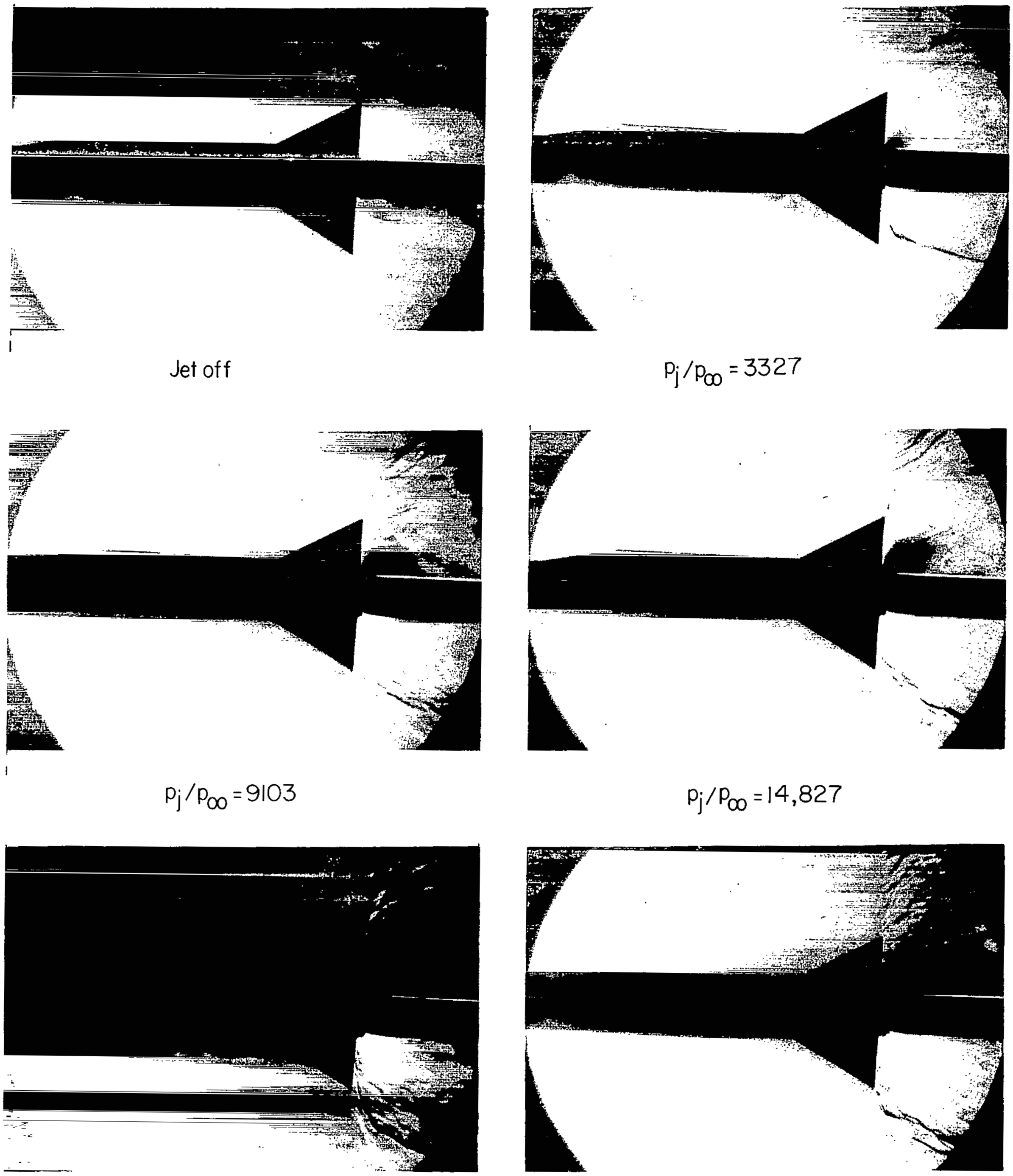

Jet off

$p_j/p_\infty = 3327$

$p_j/p_\infty = 9103$

$p_j/p_\infty = 14{,}827$

$p_j/p_\infty = 20{,}473$

$\alpha = 2°$

$p_j/p_\infty = 25{,}795$

(o) Schlieren photographs. $M_\infty = 6$; $M_j = 1.0$.

L-67-991

Figure 8.- Continued.

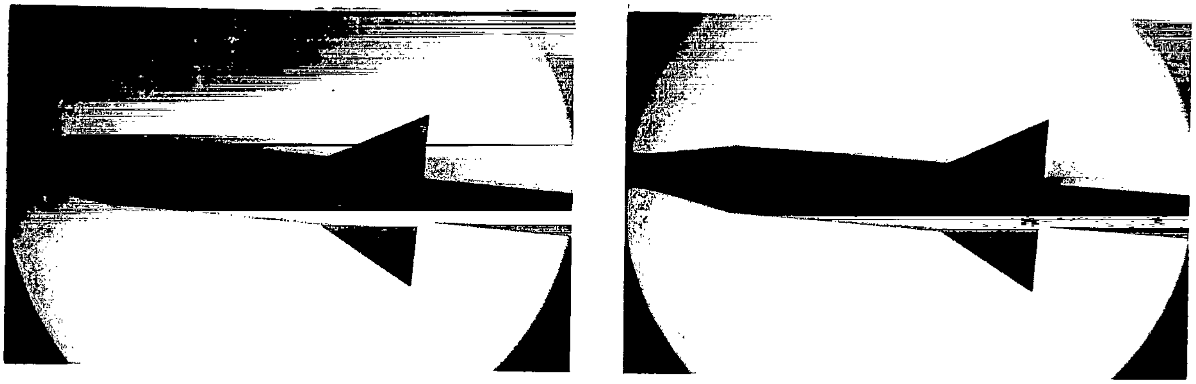

Jet off

$p_j/p_\infty = 558$

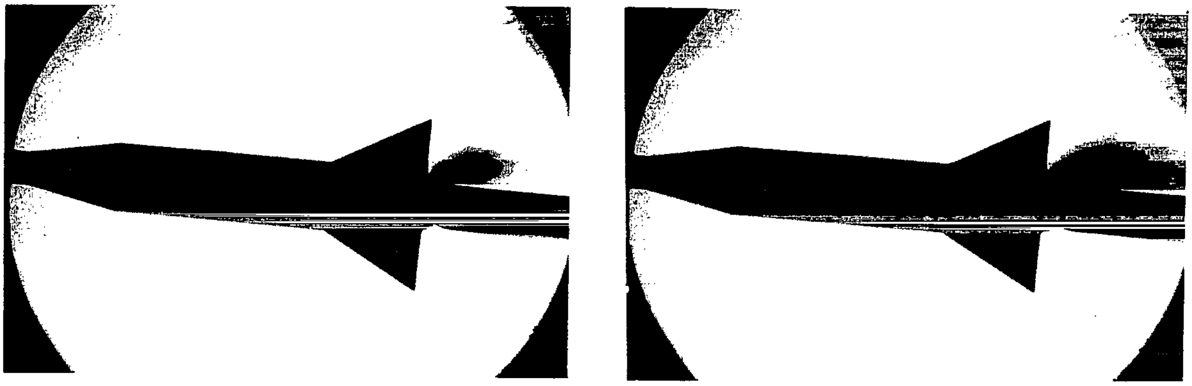

$p_j/p_\infty = 3426$

$p_j/p_\infty = 5823$

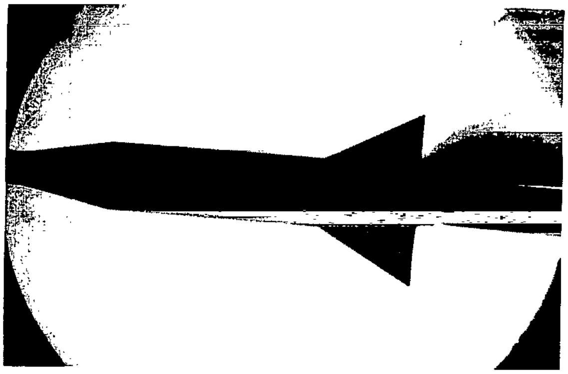

$p_j/p_\infty = 7804$
$\alpha = 4°$

(p) Schlieren photographs. $M_\infty = 6$; $M_j = 2.24$. L-67-992

Figure 8.- Continued.

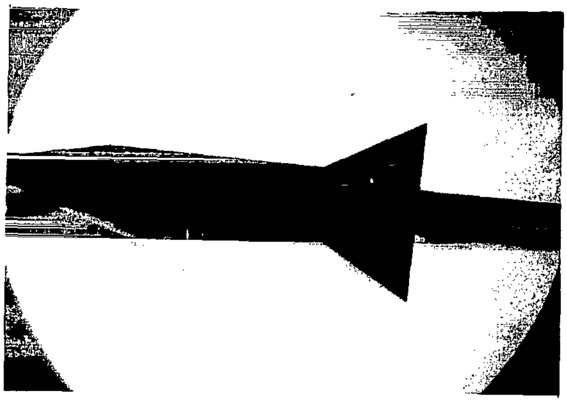

Jet off

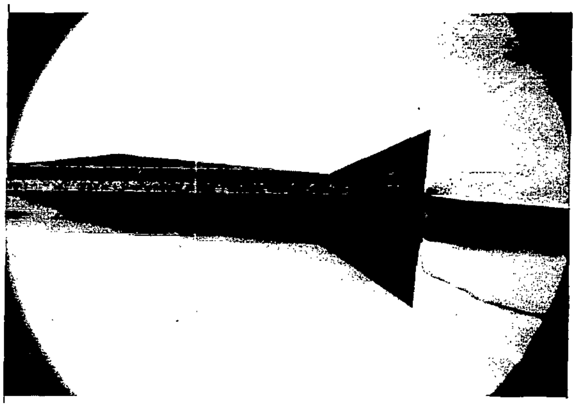

$p_j/p_\infty = 3613$

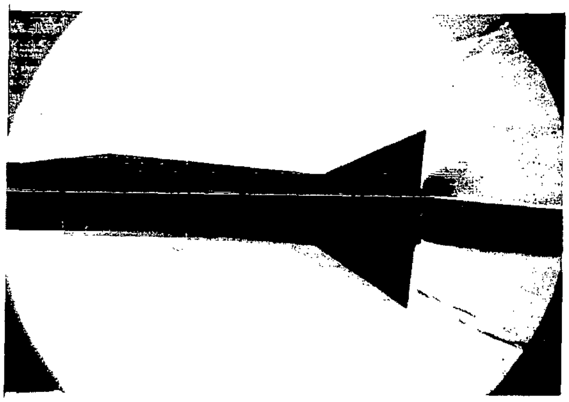

$p_j/p_\infty = 9103$

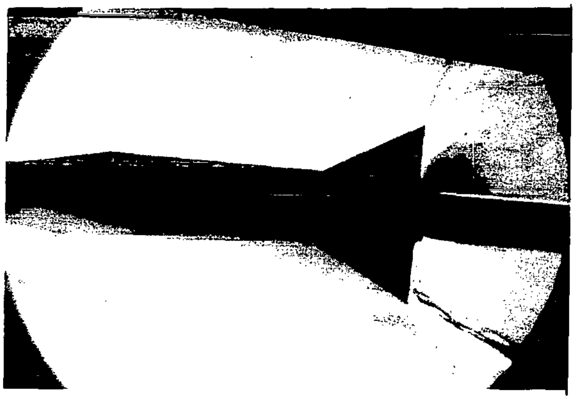

$p_j/p_\infty = 14,867$

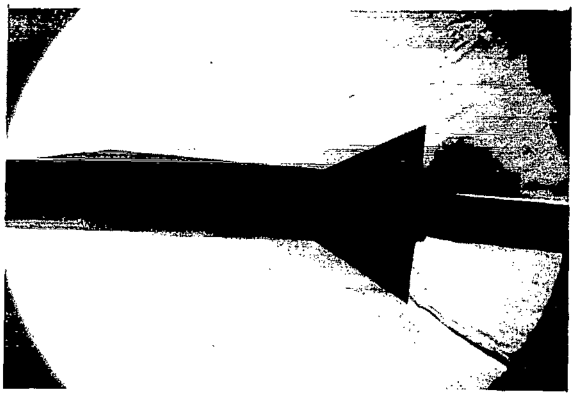

$p_j/p_\infty = 20,585$
$\alpha = 4°$

(q) Schlieren photographs. $M_\infty = 6$; $M_j = 1.0$. L-67-993

Figure 8.- Continued.

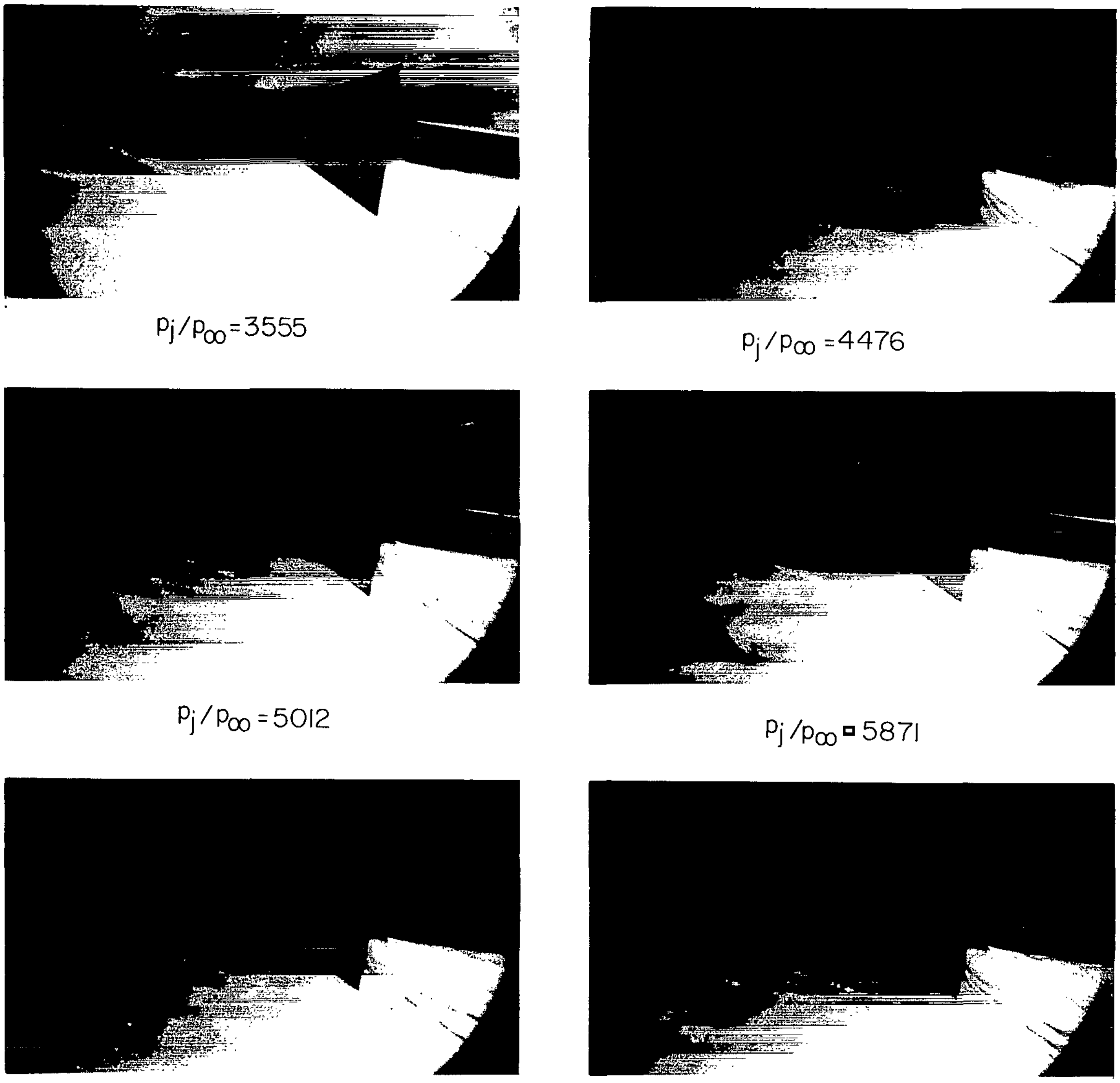

$p_j/p_\infty = 3555$

$p_j/p_\infty = 4476$

$p_j/p_\infty = 5012$

$p_j/p_\infty = 5871$

$p_j/p_\infty = 6856$

$\alpha = 8°$

$p_j/p_\infty = 7821$

(r) Schlieren photographs. $M_\infty = 6$; $M_j = 2.24$. L-67-994

Figure 8.- Continued.

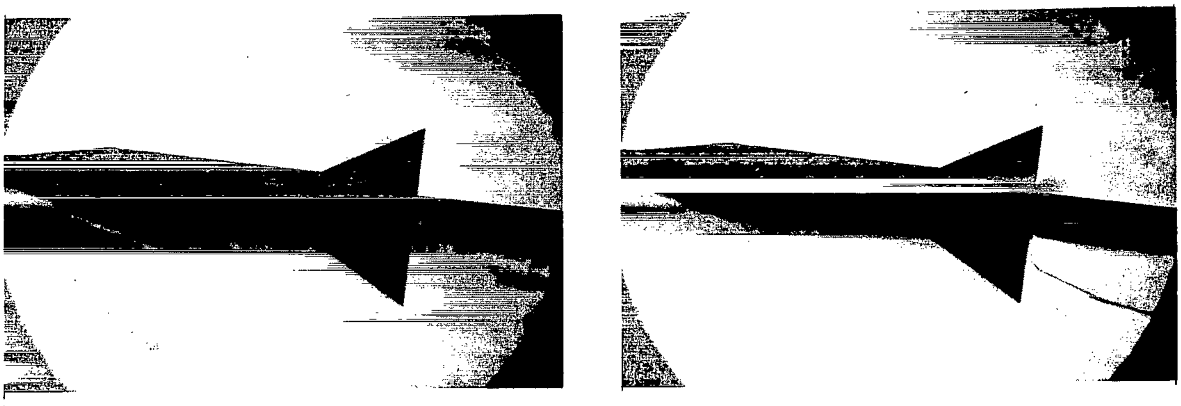

Jet off $p_j/p_\infty = 3323$

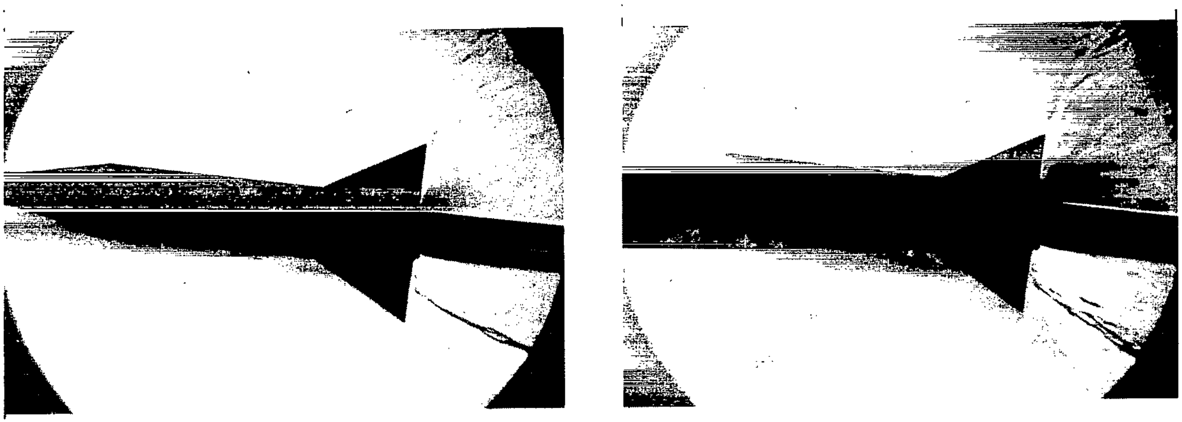

$p_j/p_\infty = 9093$ $p_j/p_\infty = 14{,}843$

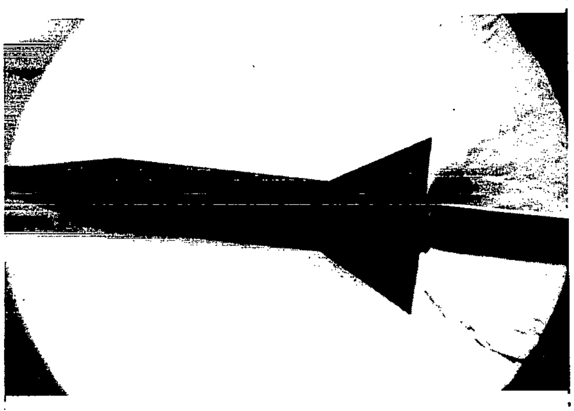

$p_j/p_\infty = 20{,}585$
$\alpha = 6°$

(s) Schlieren photographs. $M_\infty = 6$; $M_j = 1.0$.

L-67-995

Figure 8.- Concluded.

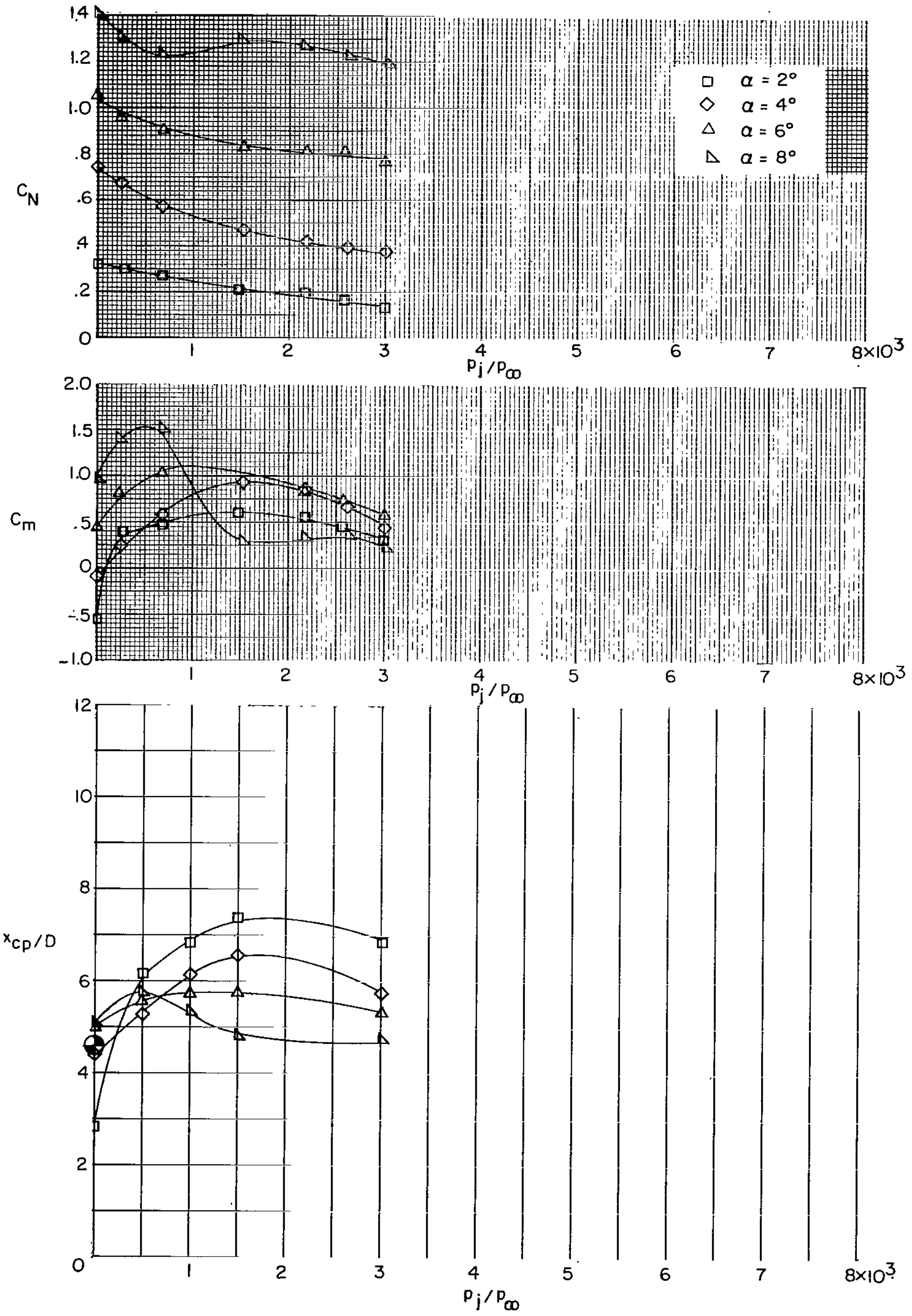

(a) $M_\infty = 4$; $M_j = 2.24$.

Figure 9.- The variation of C_N, C_m, and x_{cp}/D with pressure ratio and angle of attack for model 4, including schlieren photographs.

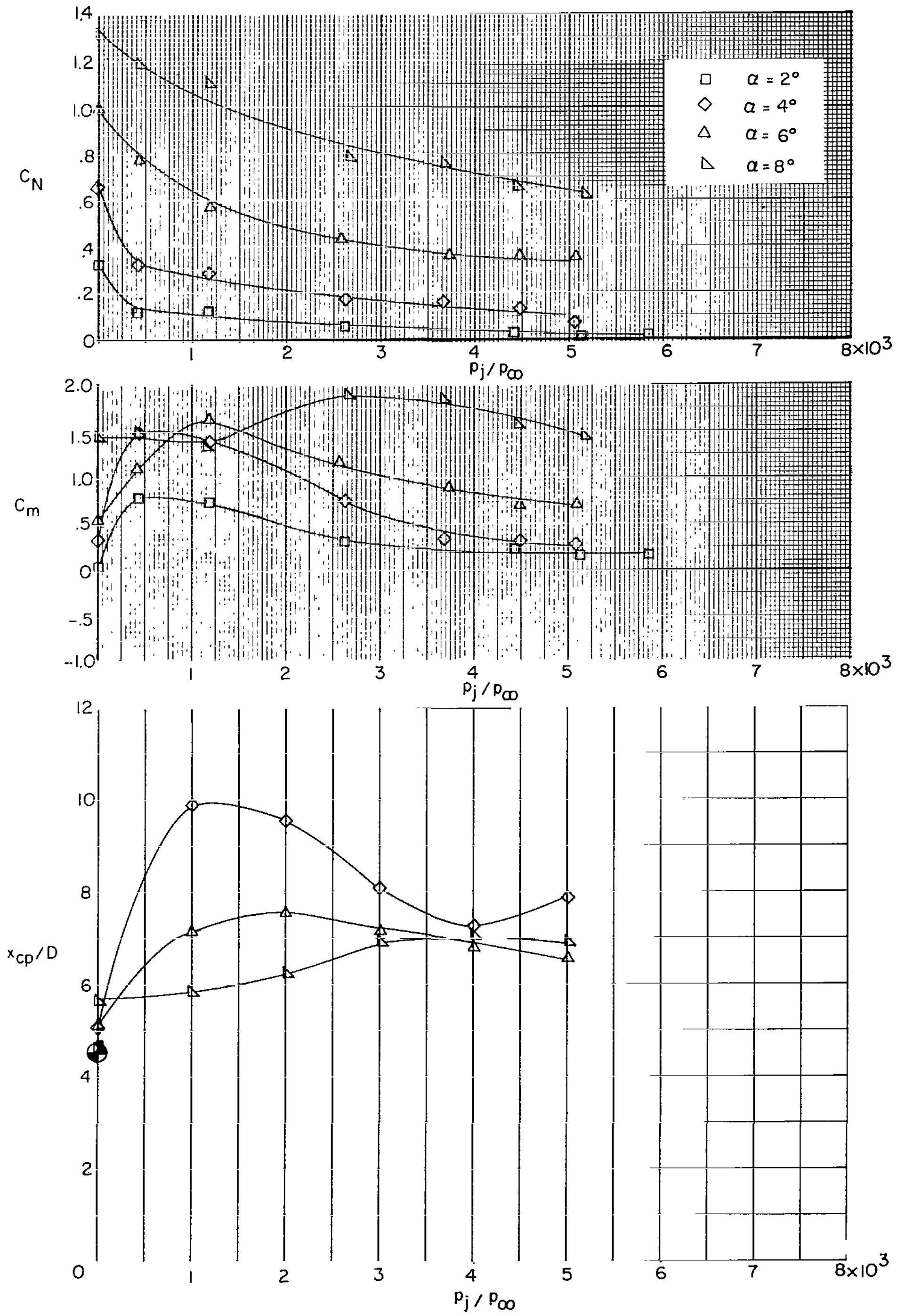

(b) $M_\infty = 5$; $M_j = 2.24$.

Figure 9.- Continued.

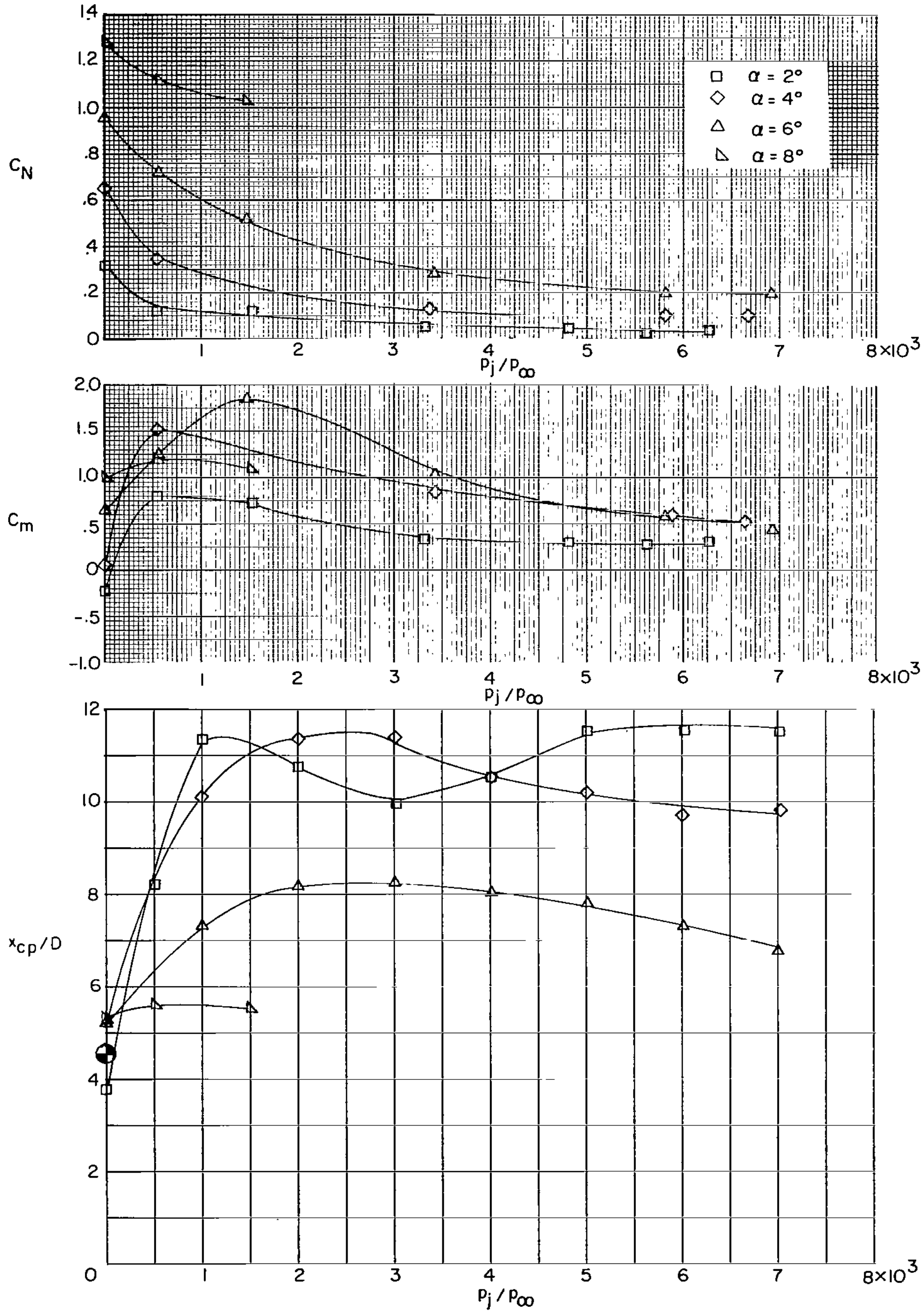

(c) $M_\infty = 6$; $M_j = 2.24$.

Figure 9.- Continued.

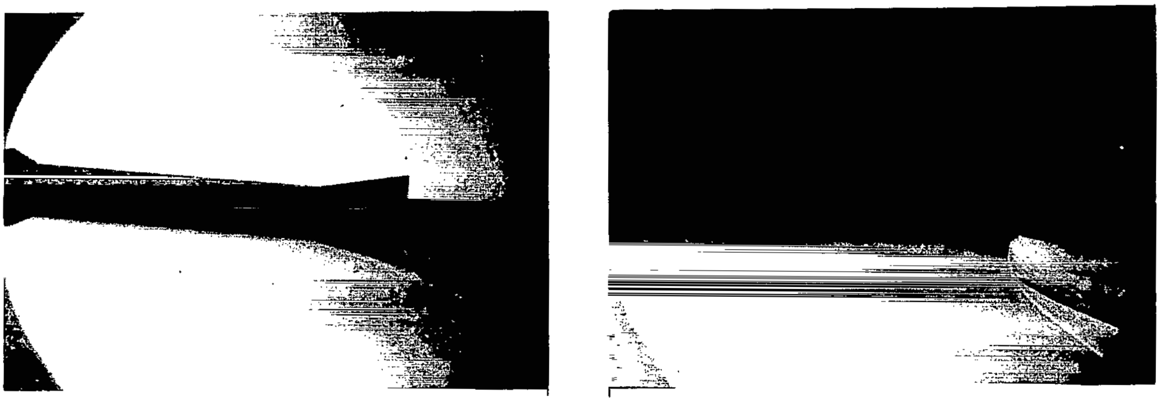

Jet off

$p_j/p_\infty = 550$

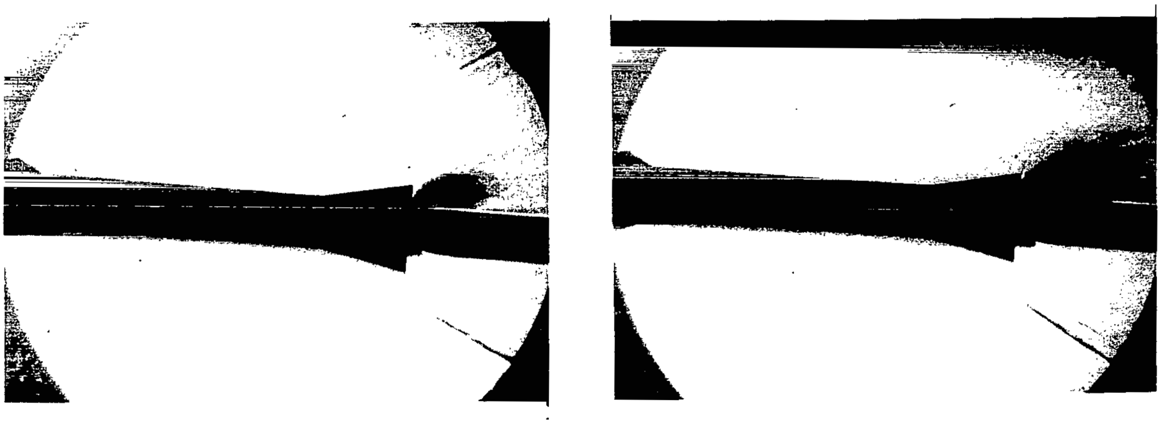

$p_j/p_\infty = 3384$

$p_j/p_\infty = 5845$

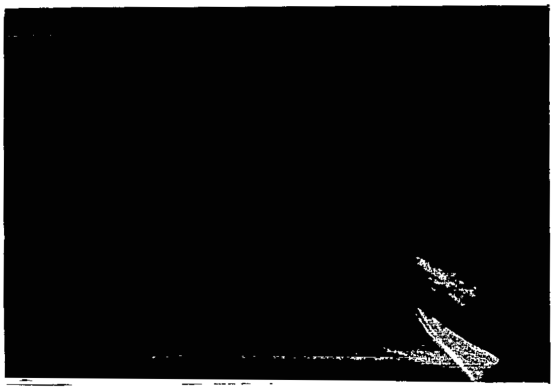

$p_j/p_\infty = 6687$
$\alpha = 4°$

(d) Schlieren photographs. $M_\infty = 6$; $M_j = 2.24$.

L-67-996

Figure 9.- Continued.

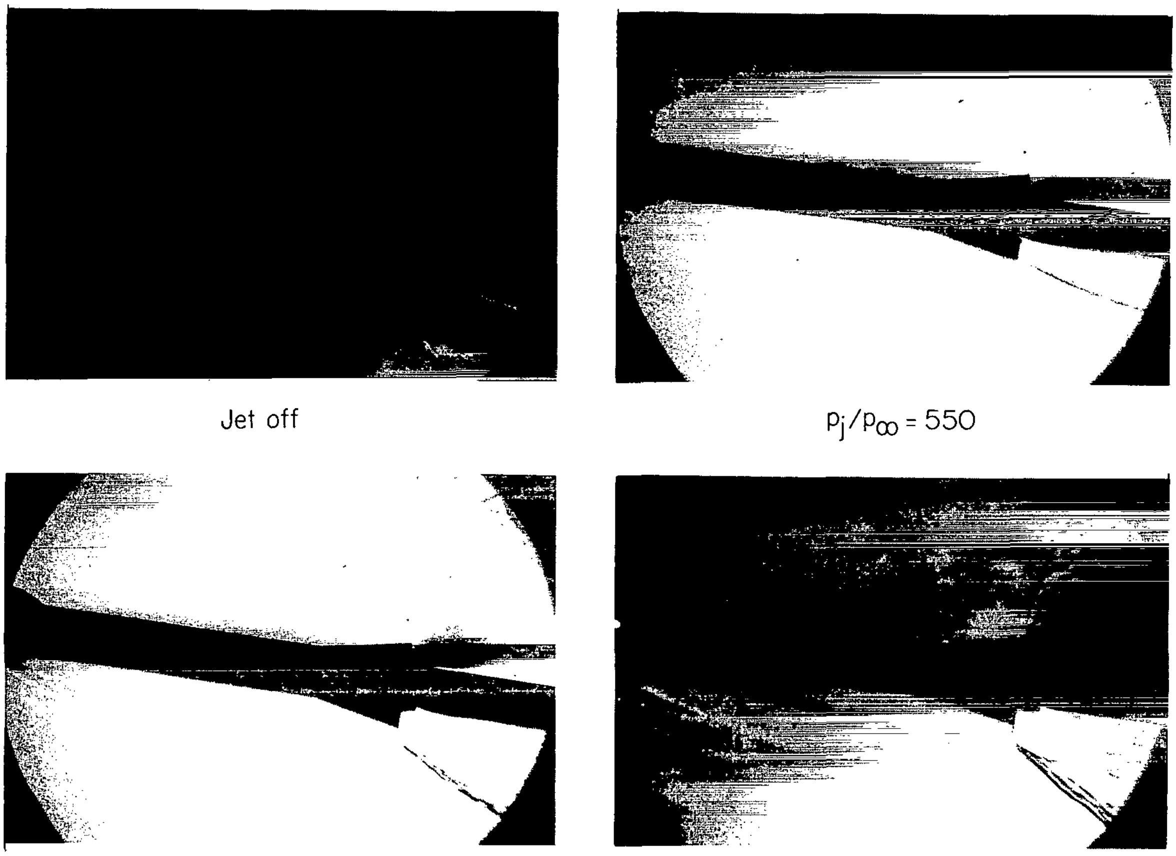

Jet off

$p_j/p_\infty = 550$

$p_j/p_\infty = 3431$

$\alpha = 6°$

$p_j/p_\infty = 6918$

(e) Schlieren photographs. $M_\infty = 6$; $M_j = 2.24$. L-67-997

Figure 9.- Concluded.

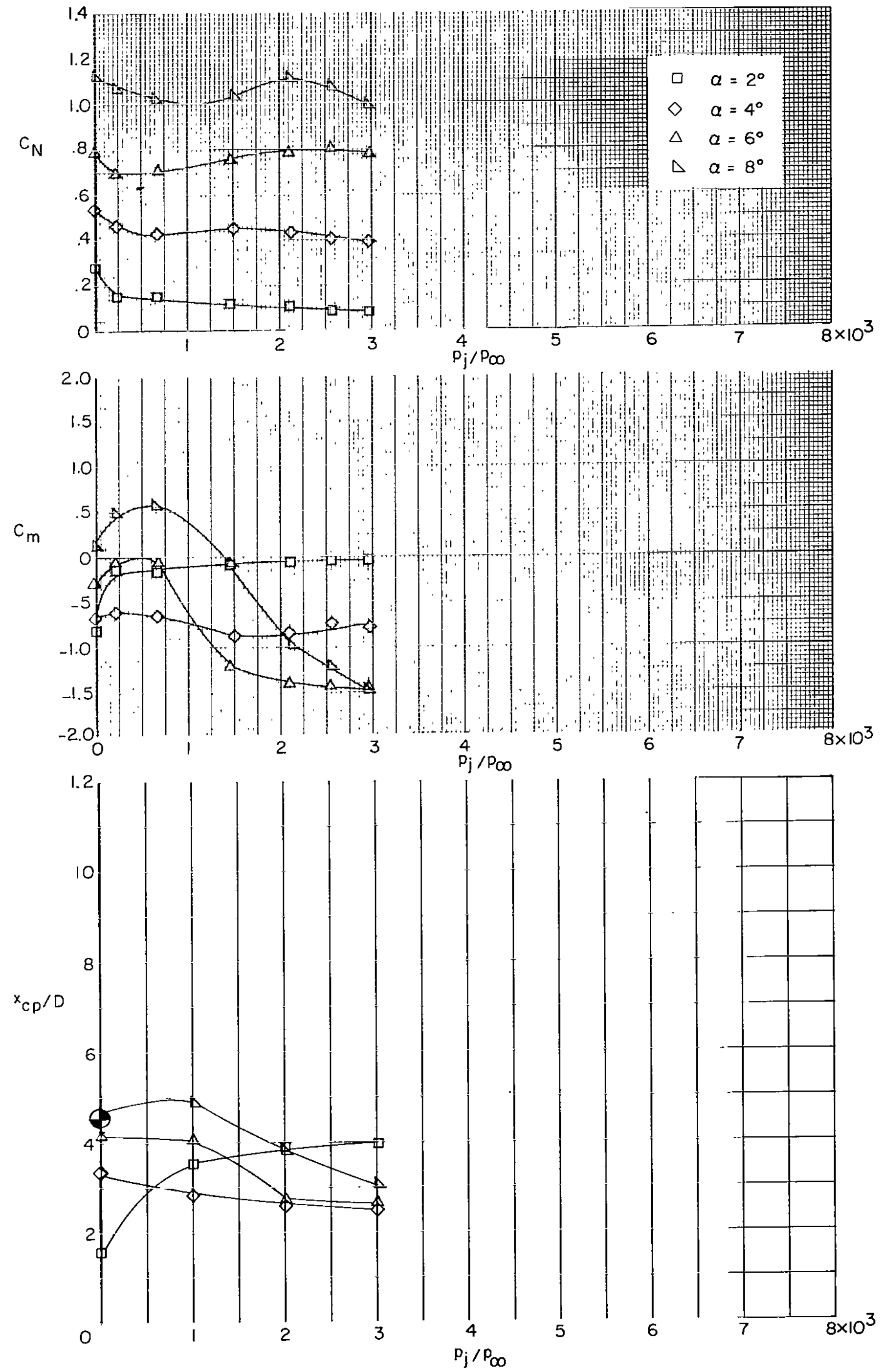

(a) $M_\infty = 4$; $M_j = 2.24$.

Figure 10.- The variation of C_N, C_m, and x_{cp}/D with pressure ratio and angle of attack for model 5, including schlieren photographs.

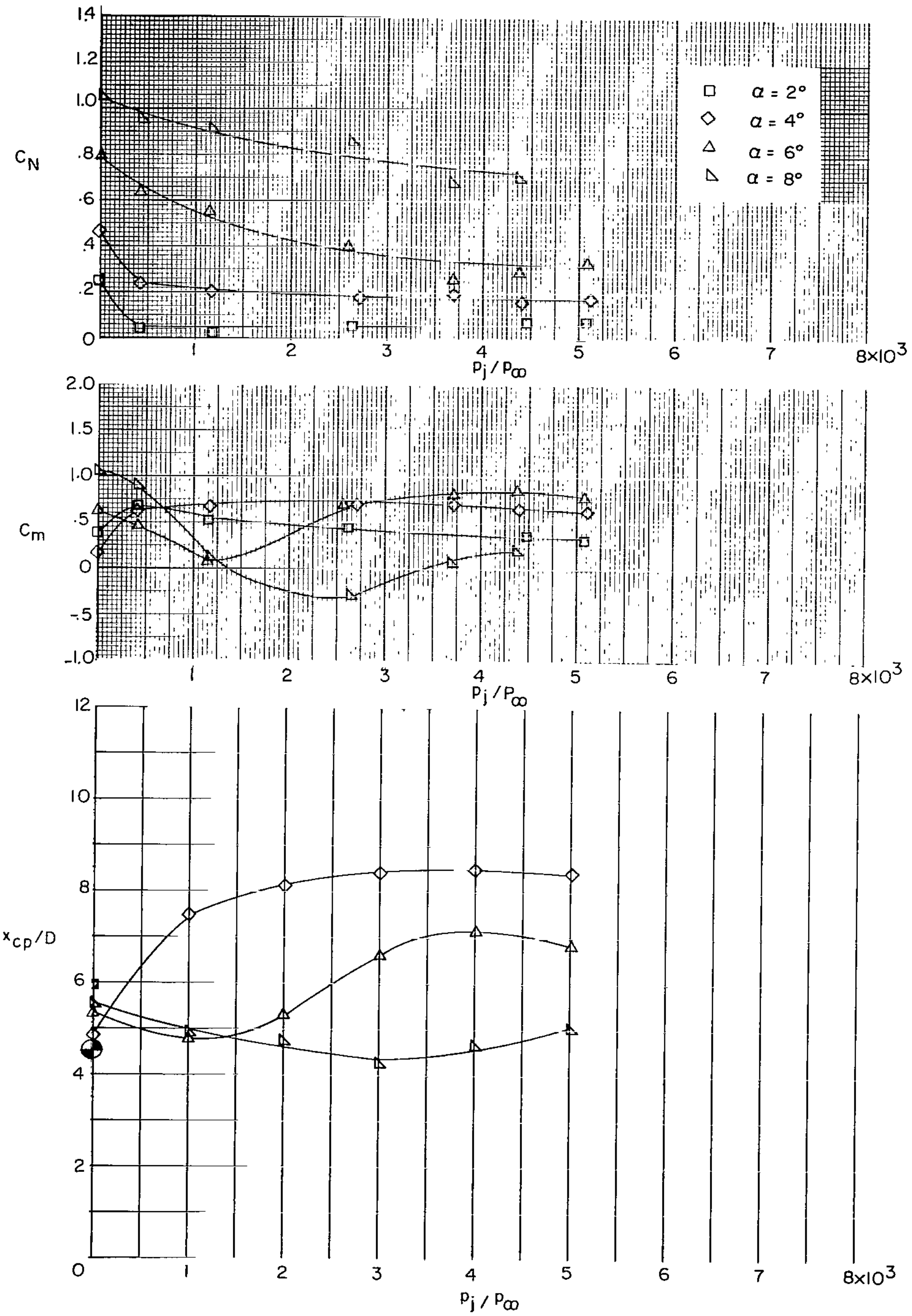

(b) $M_\infty = 5$; $M_j = 2.24$.

Figure 10.- Continued.

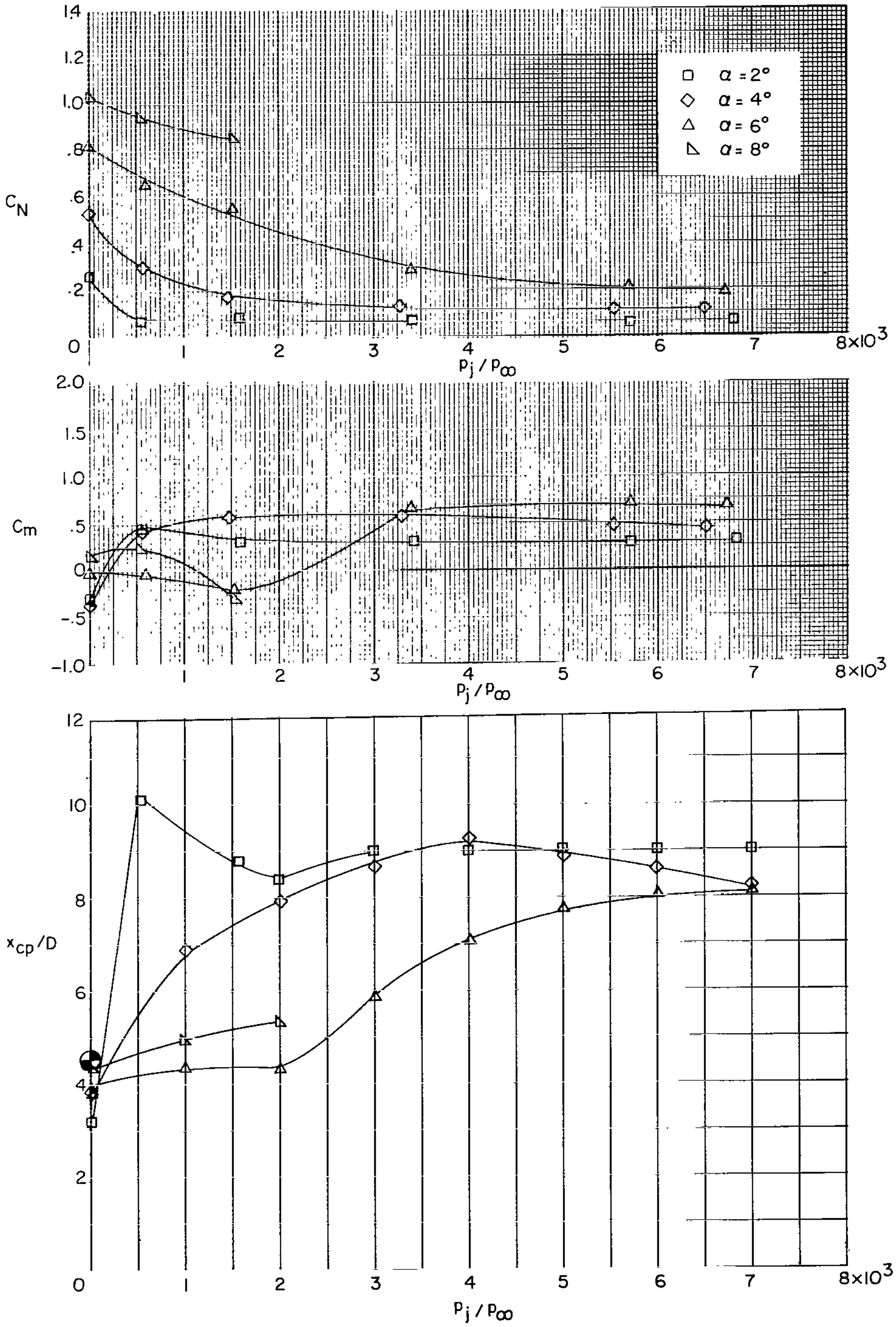

(c) $M_\infty = 6$; $M_j = 2.24$.

Figure 10.- Continued.

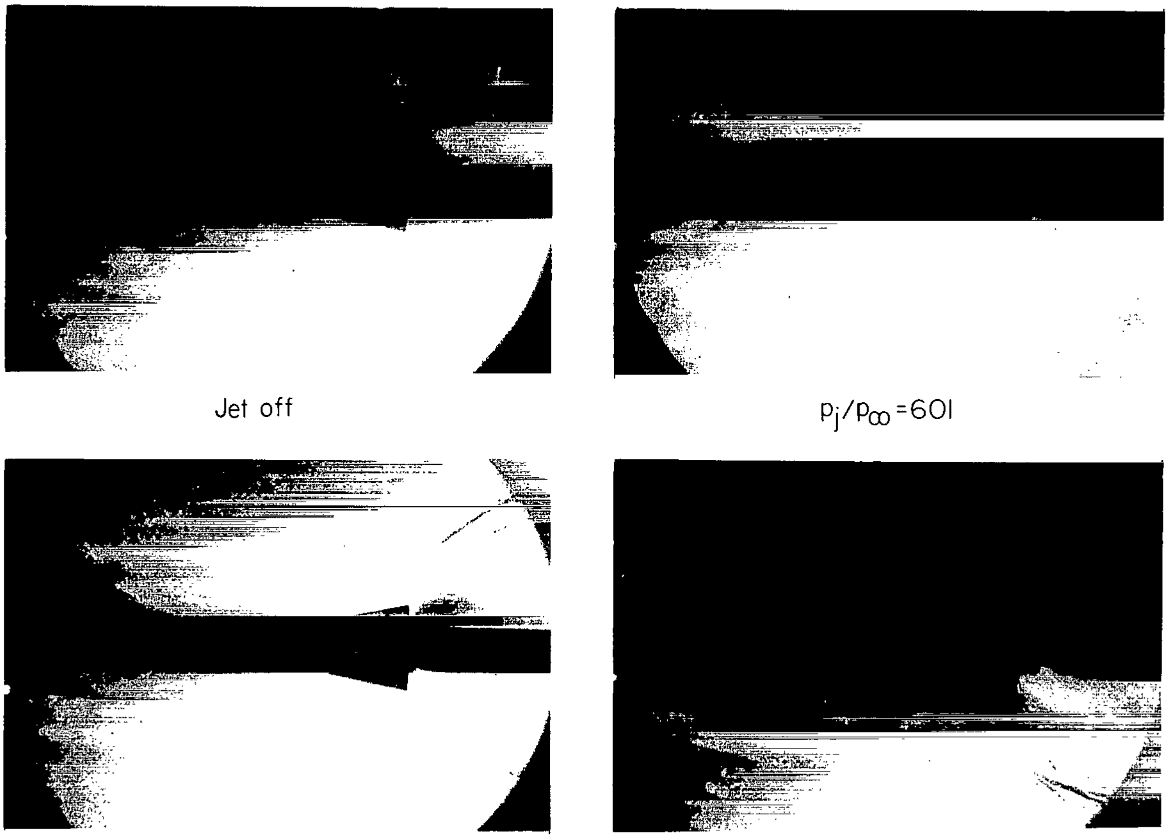

Jet off

$p_j/p_\infty = 601$

$p_j/p_\infty = 1508$

$\alpha = 0°$

$p_j/p_\infty = 6767$

(d) Schlieren photographs. $M_\infty = 6$; $M_j = 2.24$. L-67-998

Figure 10.- Continued.

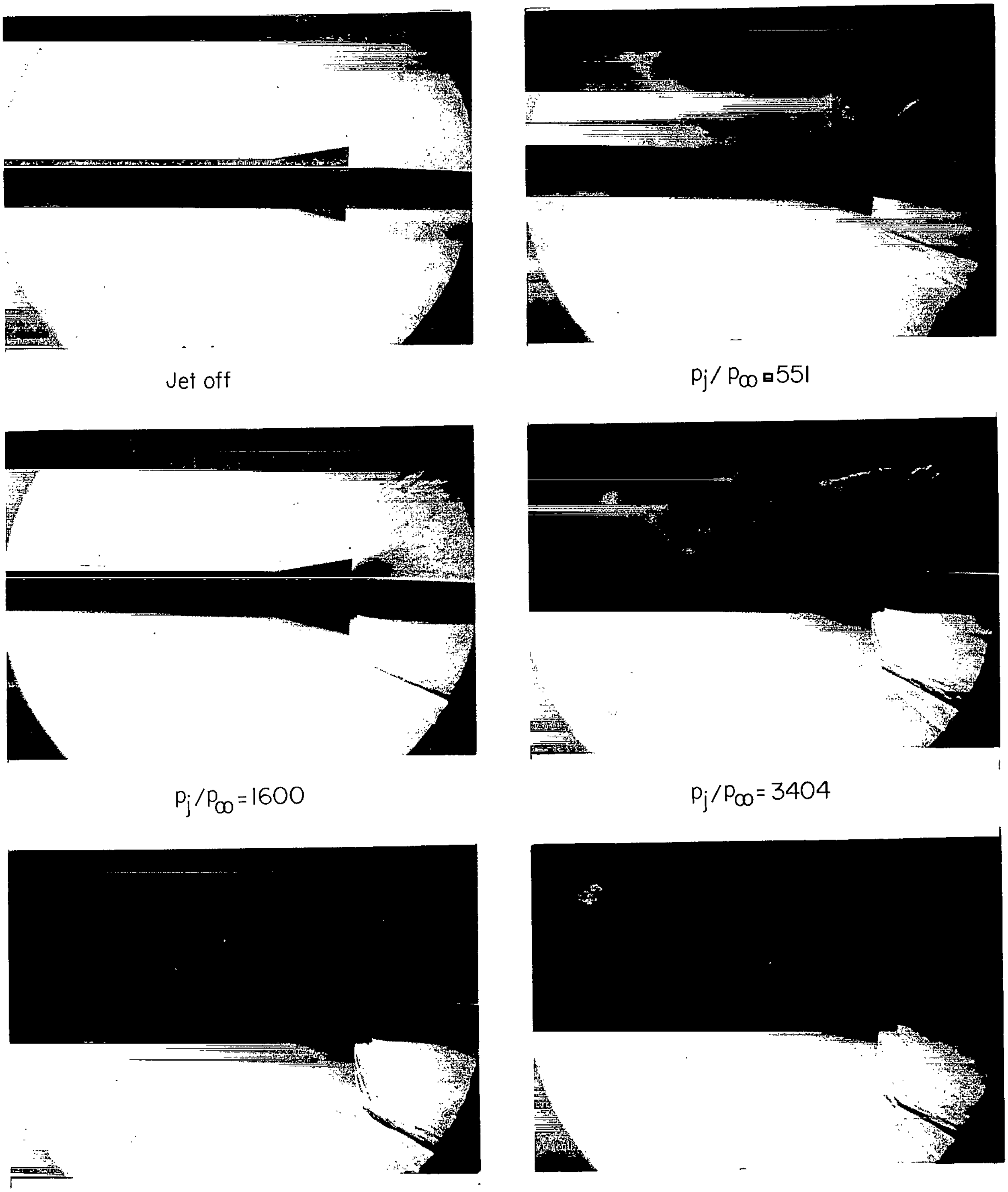

Jet off

$p_j/p_\infty = 551$

$p_j/p_\infty = 1600$

$p_j/p_\infty = 3404$

$p_j/p_\infty = 5829$

$\alpha = 2°$

$p_j/p_\infty = 6808$

(e) Schlieren photographs. $M_\infty = 6$; $M_j = 2.24$.

L-67-999

Figure 10.- Continued.

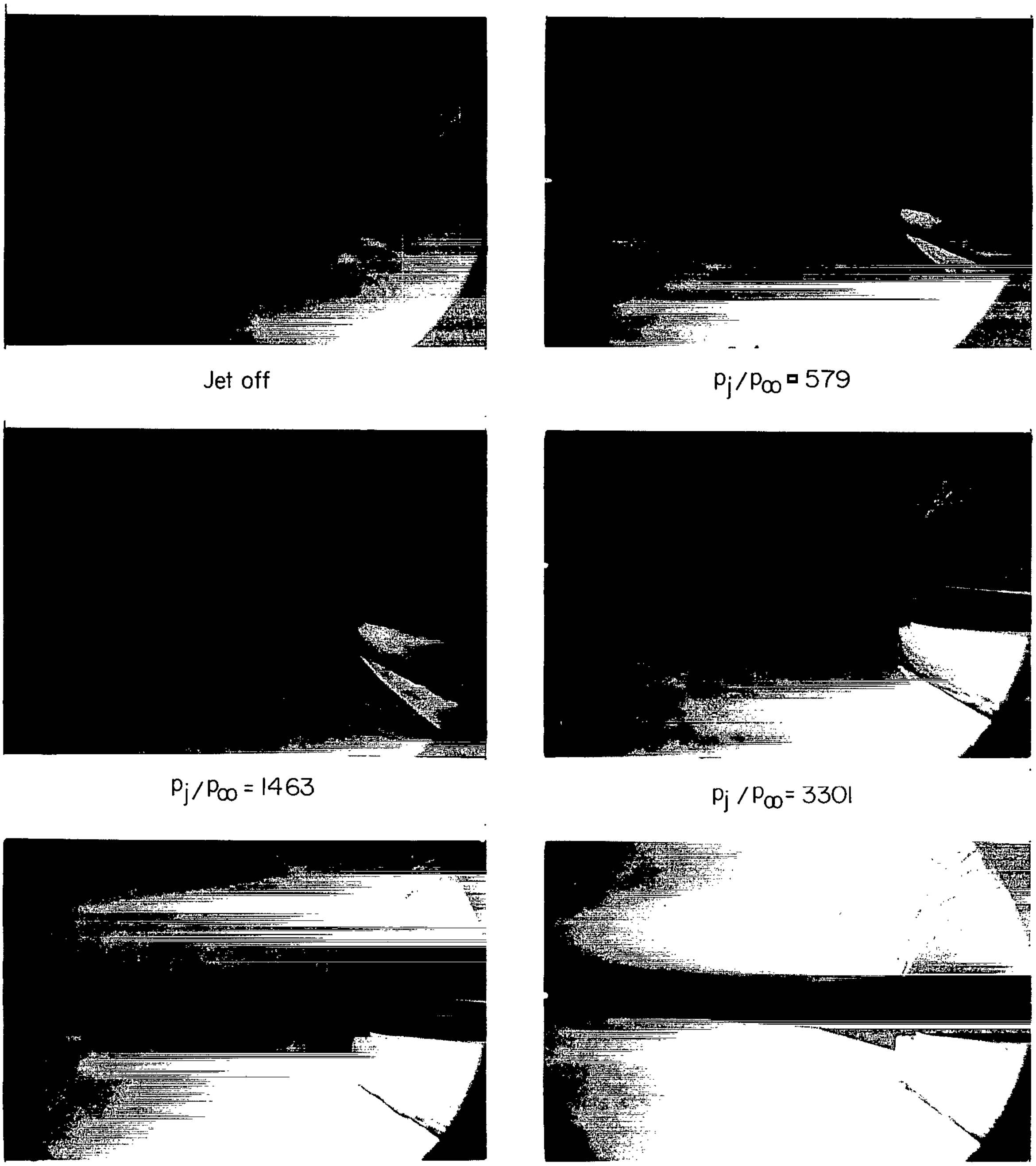

Jet off

$p_j/p_\infty = 579$

$p_j/p_\infty = 1463$

$p_j/p_\infty = 3301$

$p_j/p_\infty = 5553$

$\alpha = 4°$

$p_j/p_\infty = 6512$

(f) Schlieren photographs. $M_\infty = 6$; $M_j = 2.24$.

L-67-1000

Figure 10.- Continued.

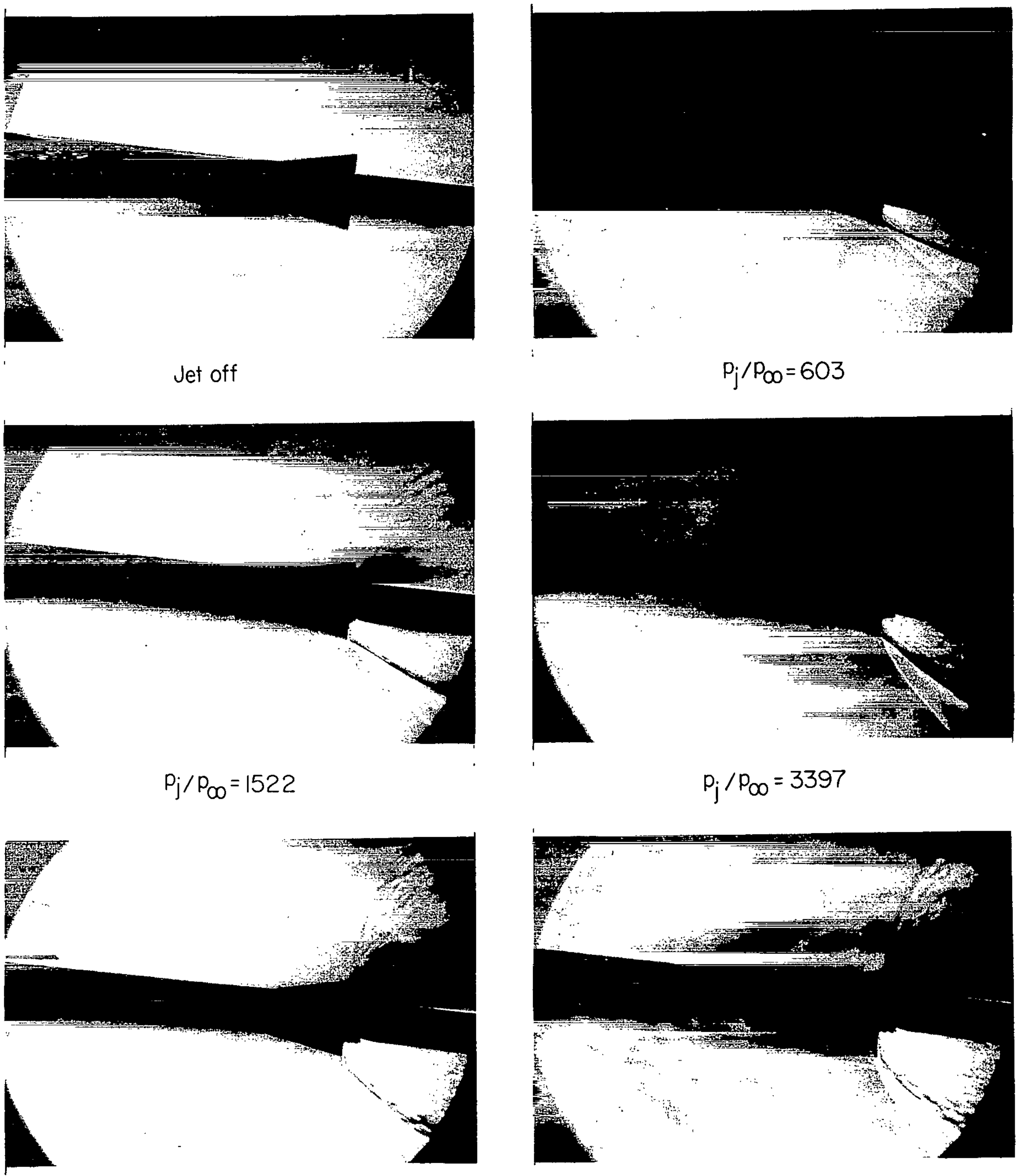

Jet off

$p_j/p_\infty = 603$

$p_j/p_\infty = 1522$

$p_j/p_\infty = 3397$

$p_j/p_\infty = 5708$

$\alpha = 6°$

$p_j/p_\infty = 6738$

(g) Schlieren photographs. $M_\infty = 6$; $M_j = 2.24$.

L-67-1001

Figure 10.- Continued.

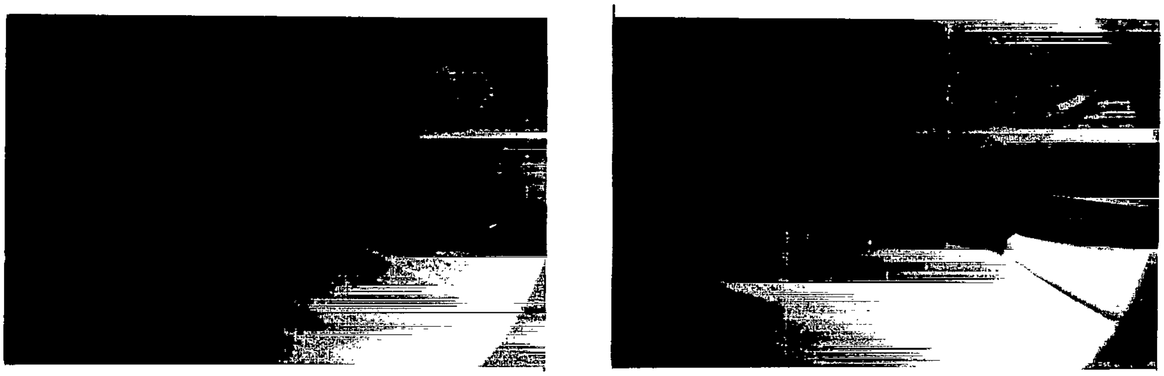

Jet off

$p_j/p_\infty = 664$

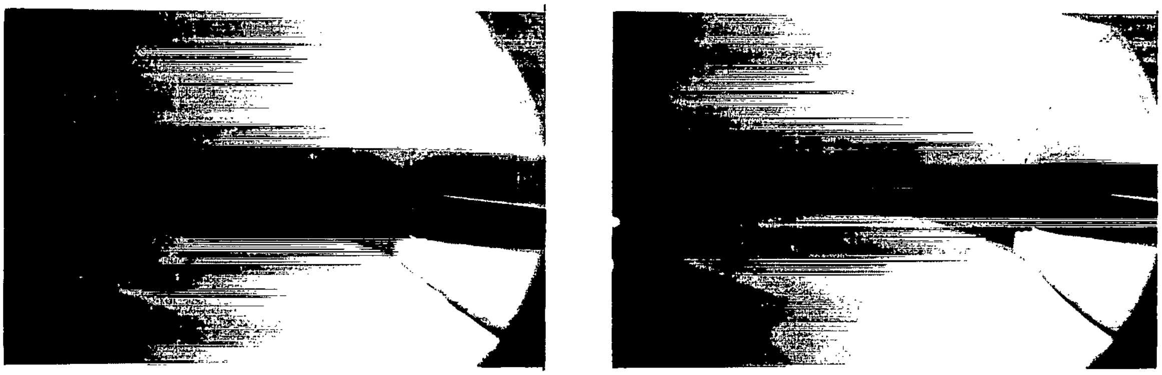

$p_j/p_\infty = 1493$

$p_j/p_\infty = 2114$

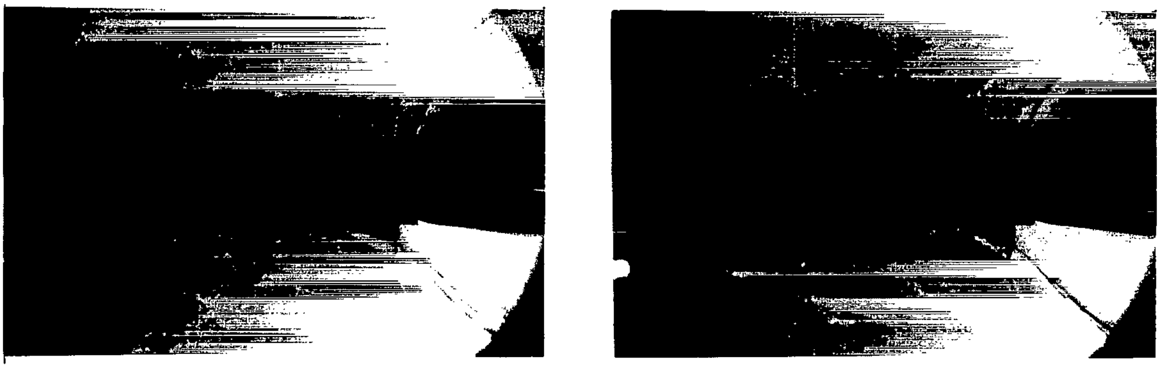

$p_j/p_\infty = 2538$

$\alpha = 6°$

$p_j/p_\infty = 2972$

(h) Schlieren photographs. $M_\infty = 4$; $M_j = 2.24$.

L-67-1002

Figure 10.- Concluded.

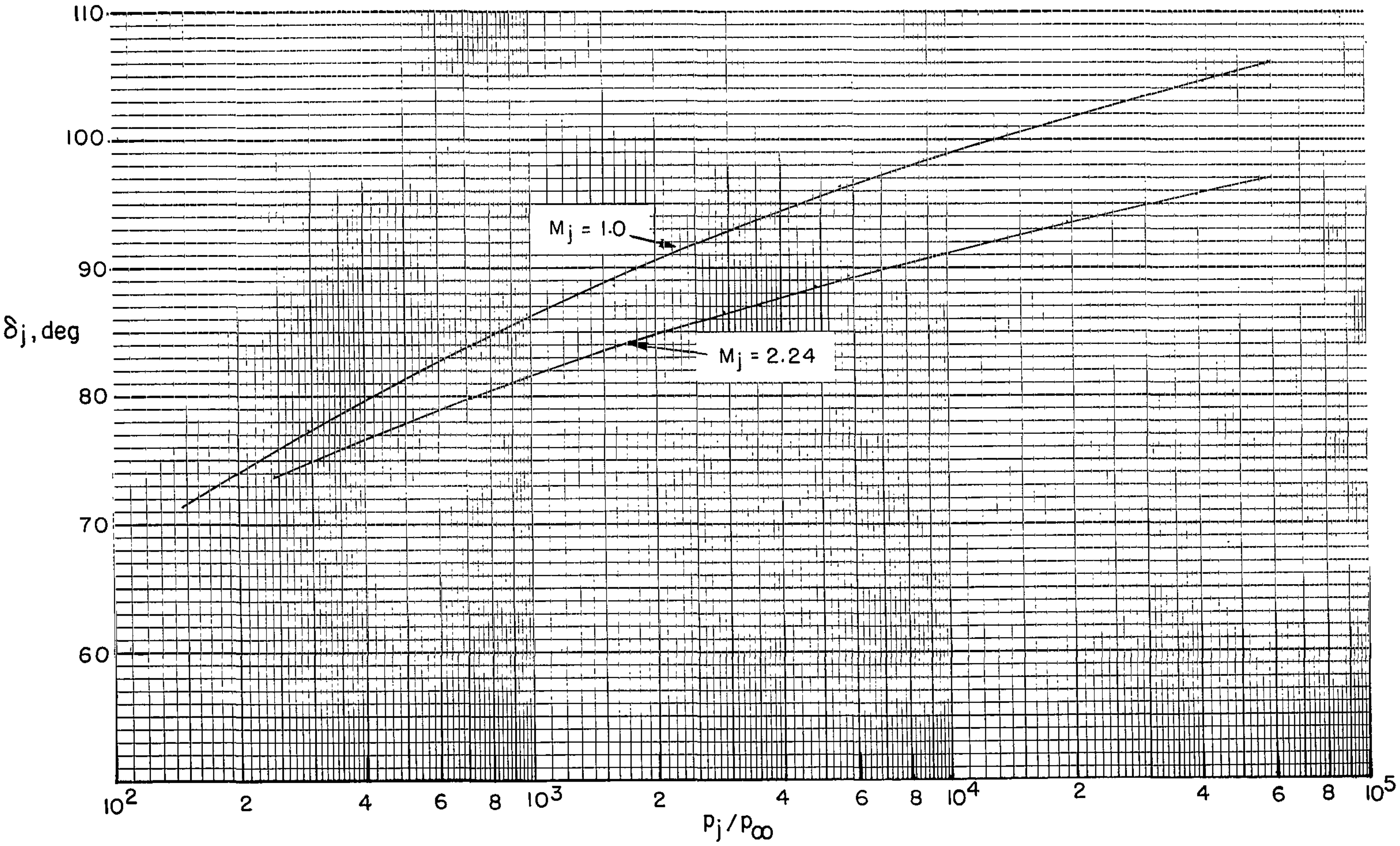

Figure 11.- Variation of the initial inclination of the jet boundary for jets exhausting into still air. $\alpha = 0^0$; $p_\infty = 0.018$ psi; $\gamma = 1.4$ (Prandtl-Meyer two-dimensional expansion).

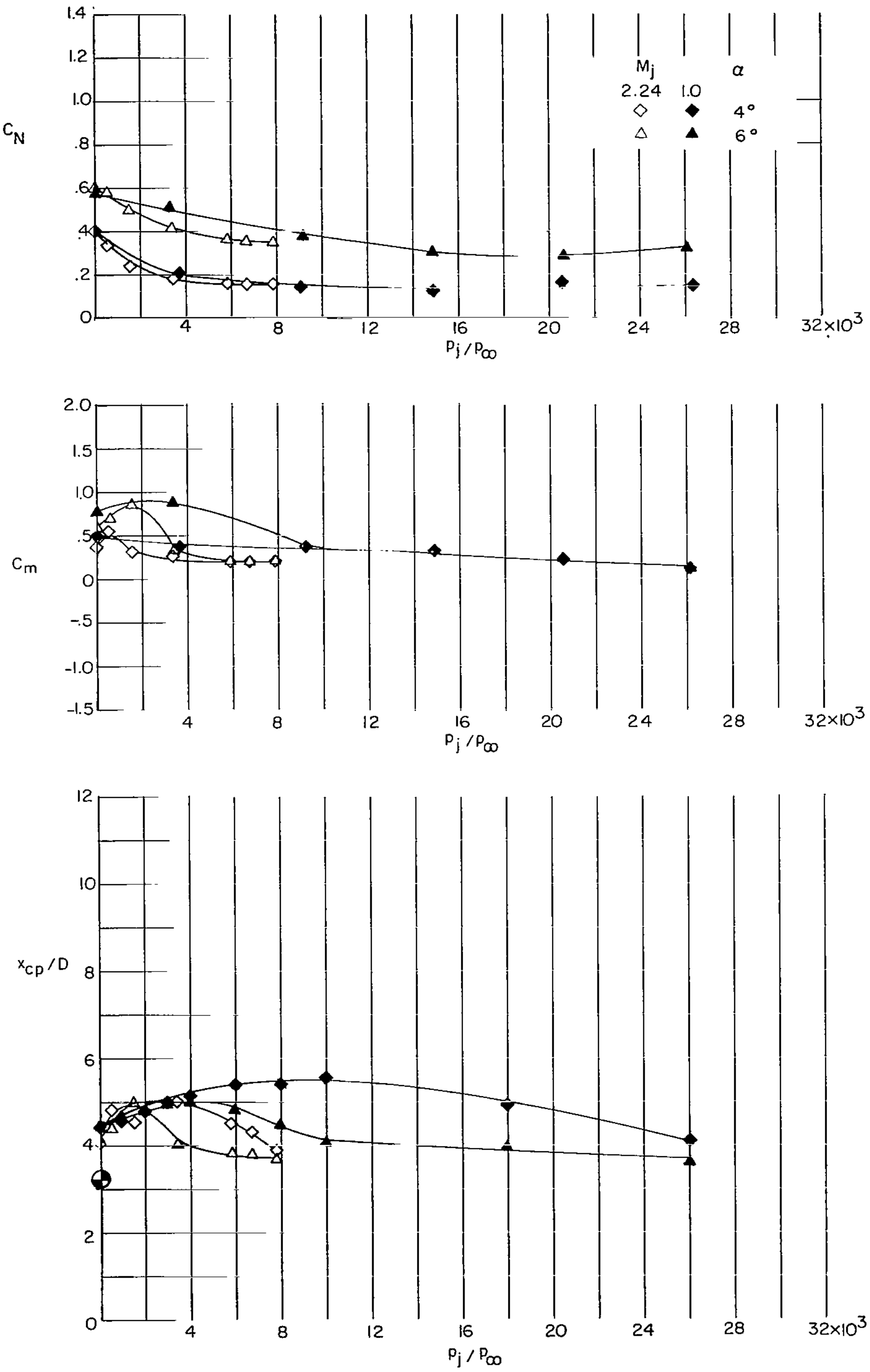

Figure 12.- Effect of nozzle geometry on the variation of C_N, C_m, and x_{cp}/D with jet pressure ratio for model 3 at $M_\infty = 6$.

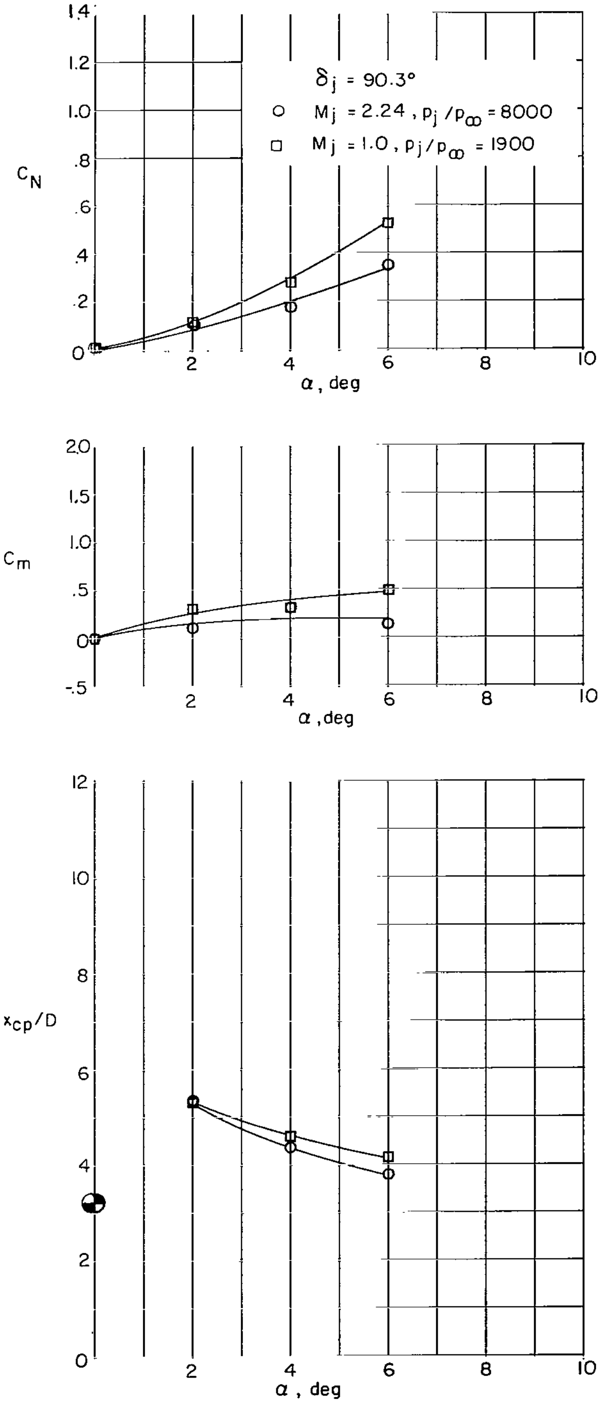

Figure 13.- Variation of C_N, C_m, and x_{cp}/D for model 3 simulating the same initial jet starting angle $\delta_j = 90.3^\circ$. $M_\infty = 6$.

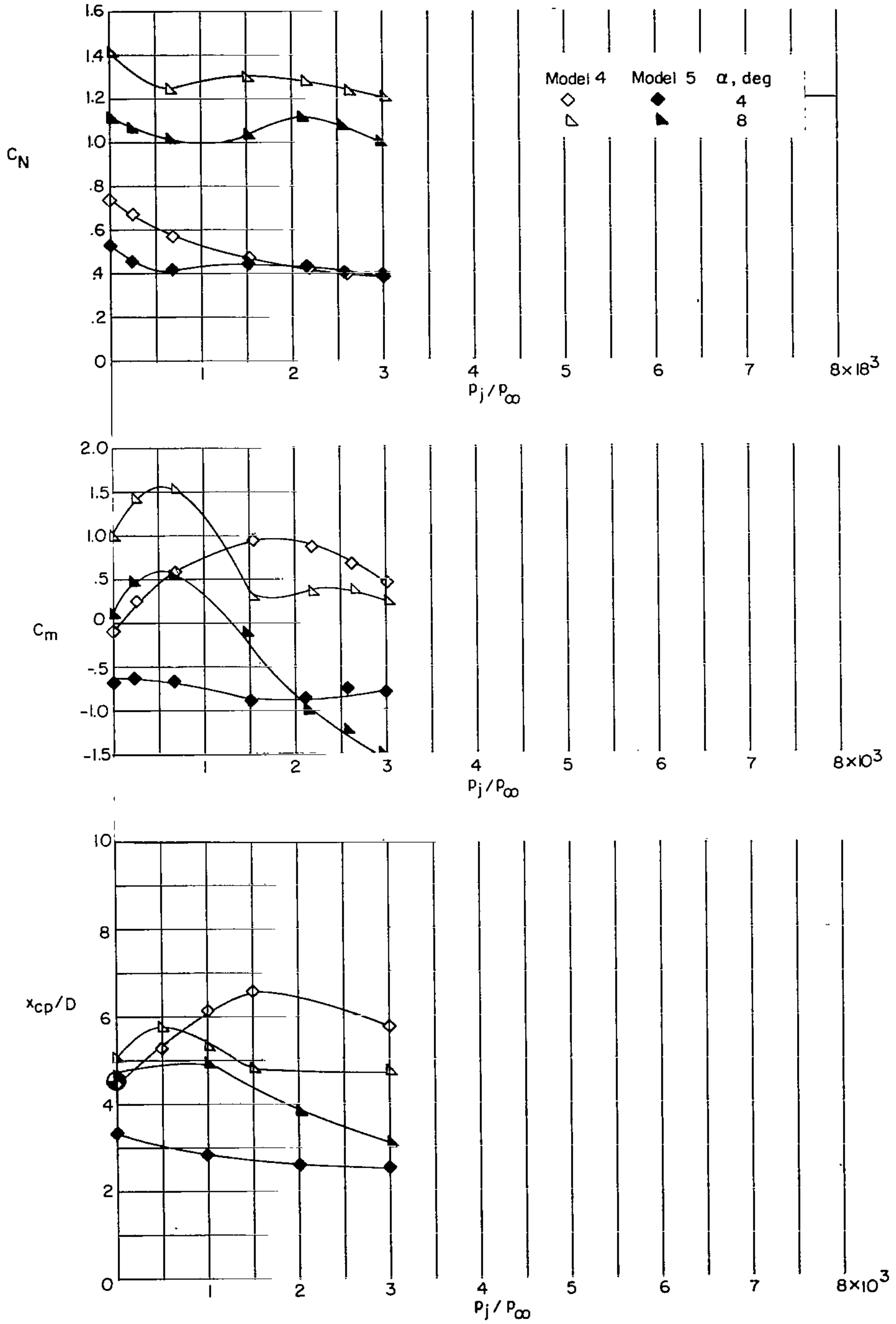

(a) $M_\infty = 4$.

Figure 14.- Effect of flare—reverse-flare on C_N, C_m, and x_{cp}/D between models 4 and 5 with jet pressure ratio. $M_j = 2.24$.

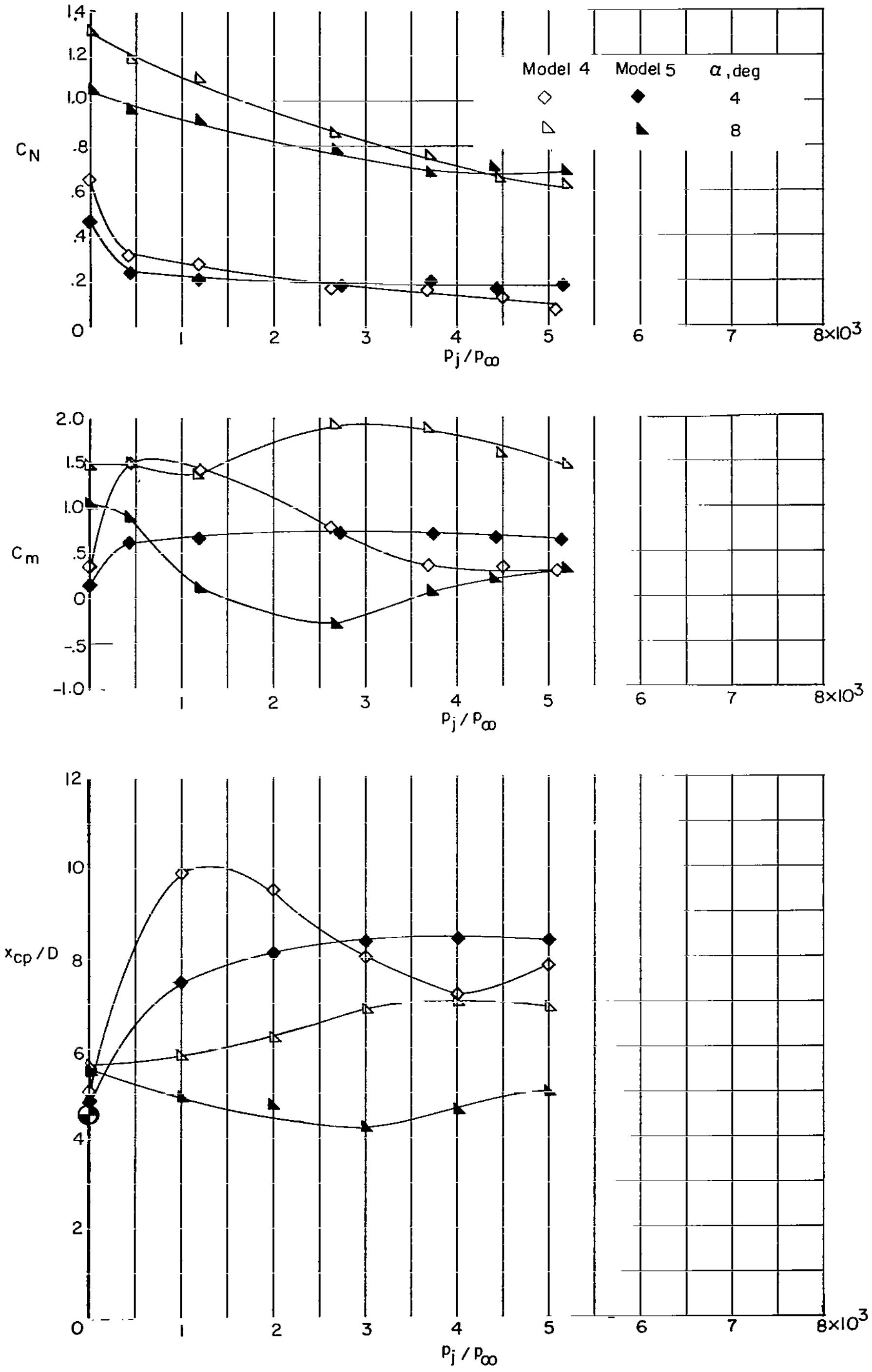

(b) $M_\infty = 5$.

Figure 14.- Continued.

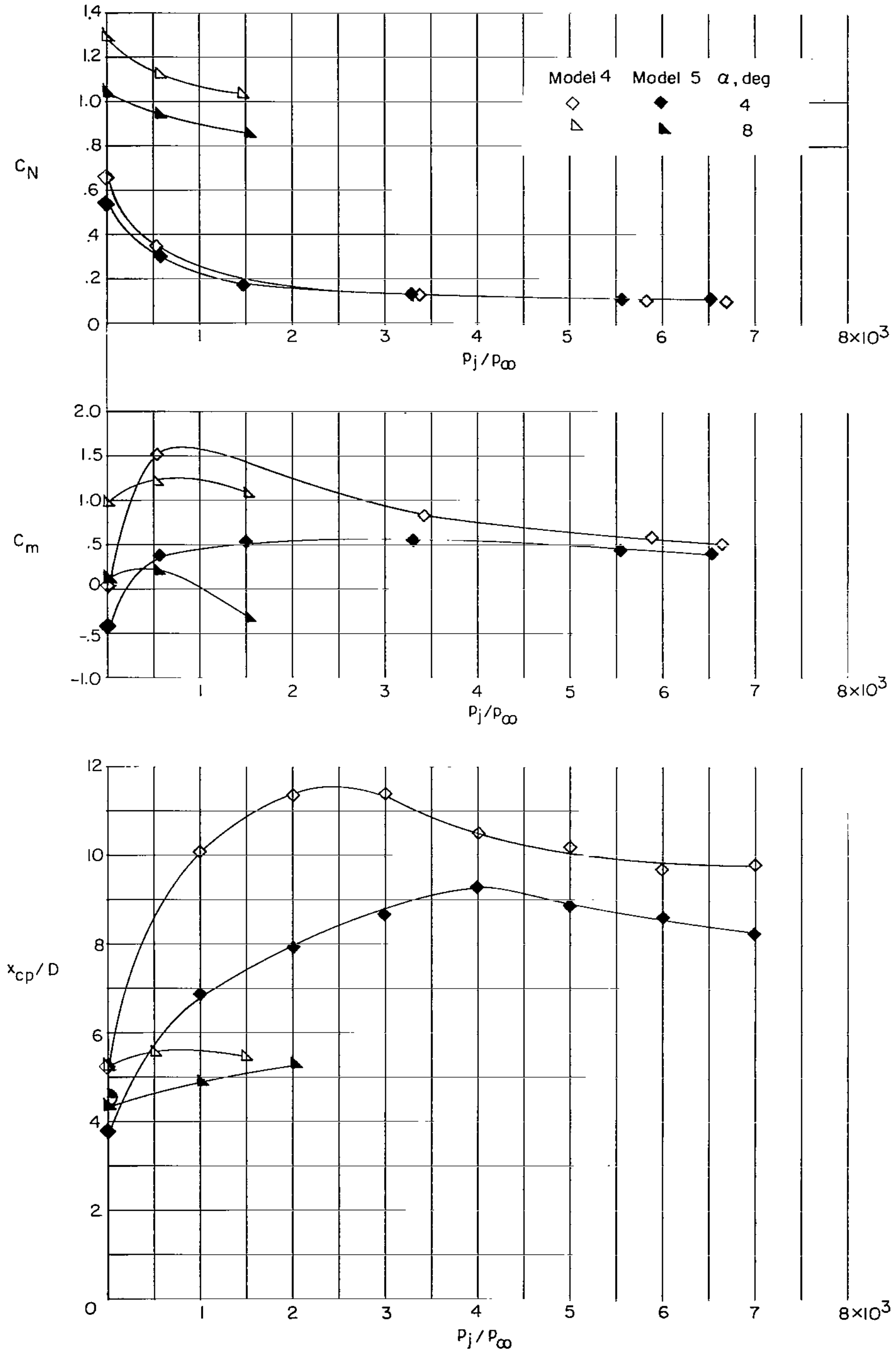

(c) $M_\infty = 6$.

Figure 14.- Concluded.

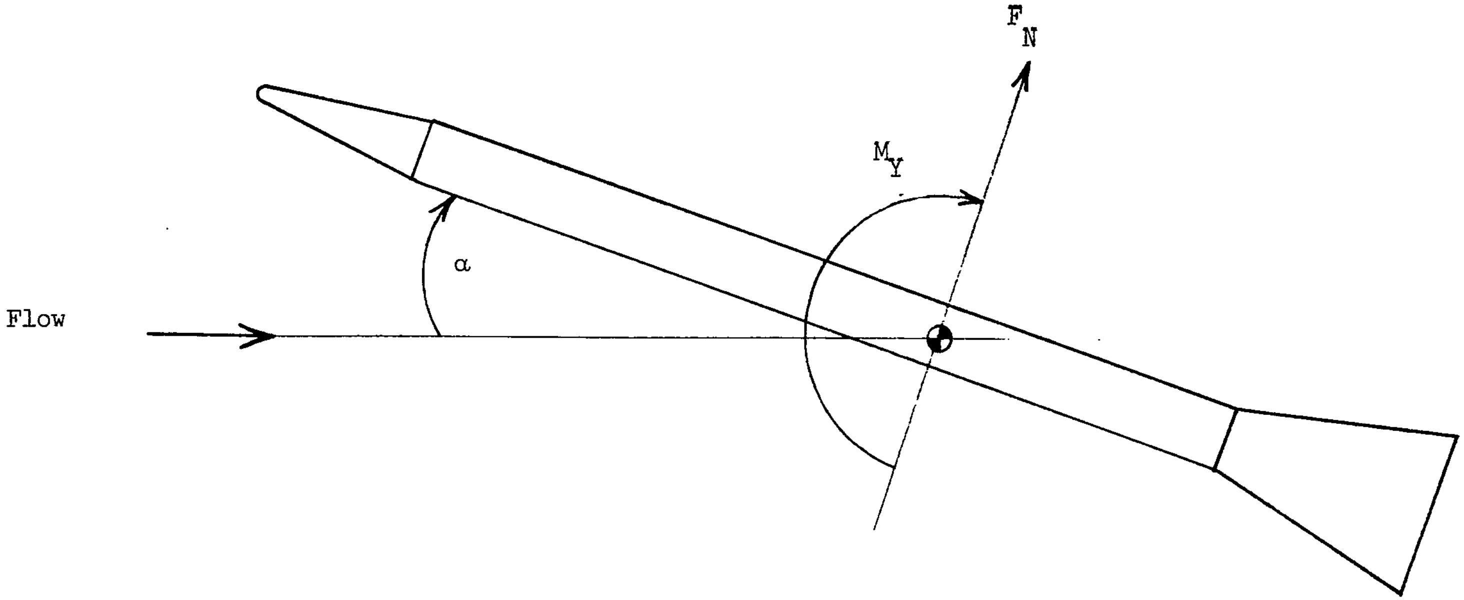

Figure 4.- Body-axis system. Arrows indicate positive direction.

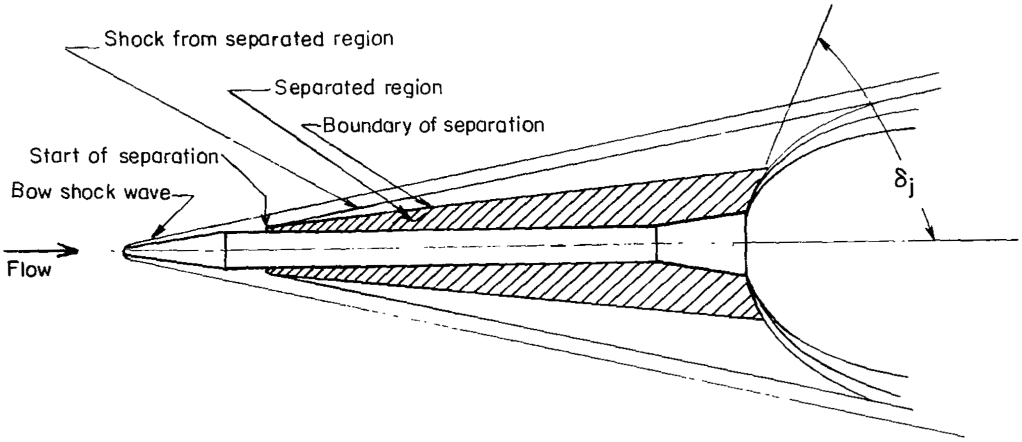

(a) Low angle of attack.

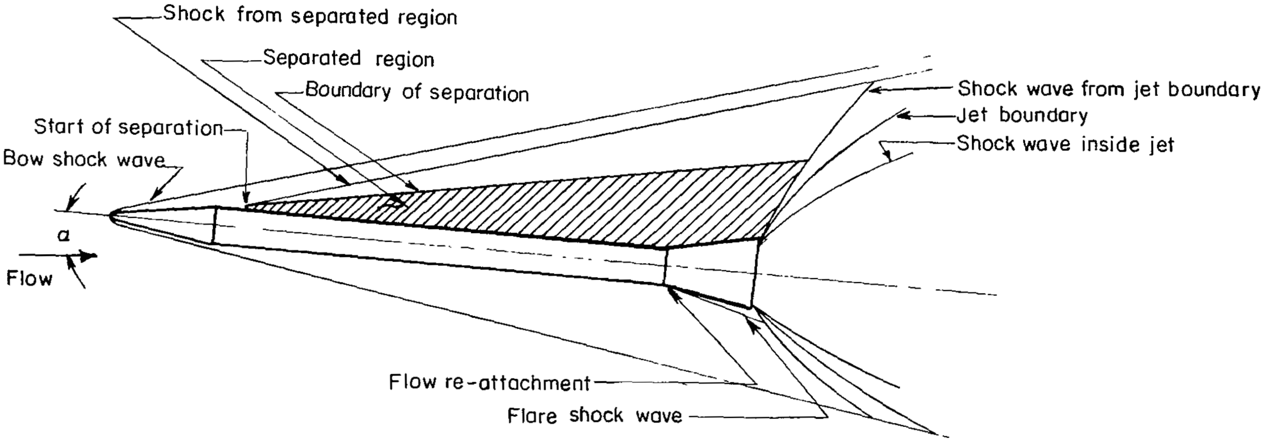

(b) High angle of attack.

Figure 5.- Schematic representation of the flow-field nomenclature.

"The aeronautical and space activities of the United States shall be conducted so as to contribute . . . to the expansion of human knowledge of phenomena in the atmosphere and space. The Administration shall provide for the widest practicable and appropriate dissemination of information concerning its activities and the results thereof."

—NATIONAL AERONAUTICS AND SPACE ACT OF 1958

NASA SCIENTIFIC AND TECHNICAL PUBLICATIONS

TECHNICAL REPORTS: Scientific and technical information considered important, complete, and a lasting contribution to existing knowledge.

TECHNICAL NOTES: Information less broad in scope but nevertheless of importance as a contribution to existing knowledge.

TECHNICAL MEMORANDUMS: Information receiving limited distribution because of preliminary data, security classification, or other reasons.

CONTRACTOR REPORTS: Scientific and technical information generated under a NASA contract or grant and considered an important contribution to existing knowledge.

TECHNICAL TRANSLATIONS: Information published in a foreign language considered to merit NASA distribution in English.

SPECIAL PUBLICATIONS: Information derived from or of value to NASA activities. Publications include conference proceedings, monographs, data compilations, handbooks, sourcebooks, and special bibliographies.

TECHNOLOGY UTILIZATION PUBLICATIONS: Information on technology used by NASA that may be of particular interest in commercial and other non-aerospace applications. Publications include Tech Briefs, Technology Utilization Reports and Notes, and Technology Surveys.

Details on the availability of these publications may be obtained from:

SCIENTIFIC AND TECHNICAL INFORMATION DIVISION
NATIONAL AERONAUTICS AND SPACE ADMINISTRATION
Washington, D.C. 20546